ISSN: 2150-4091 (Print), 2150-4105 (Online) Volume 1, Number 3, December 2009

Scientific Research

Natural Science

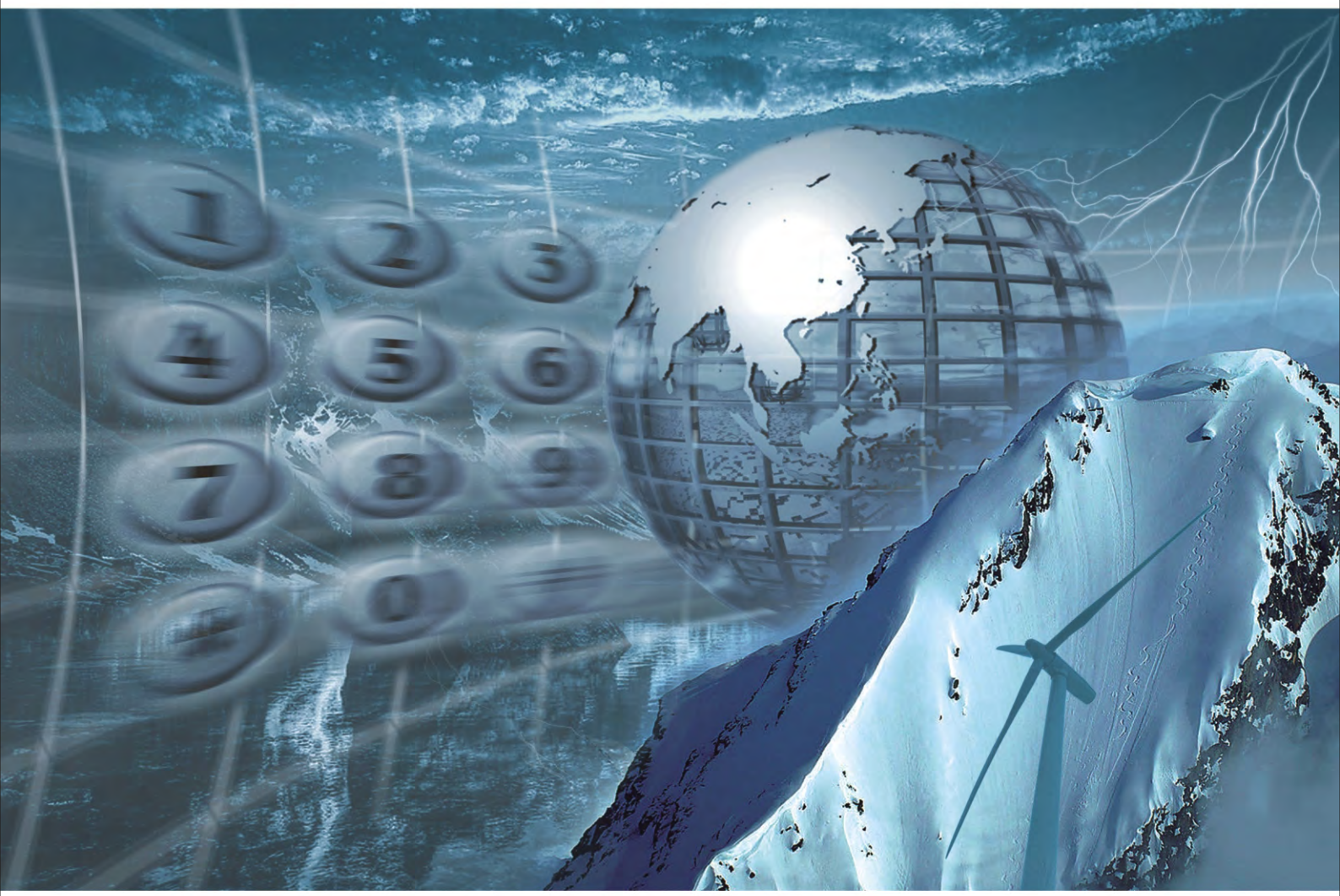

www. scirp. org/journal/ns/

Journal Editorial Board

ISSN: 2150-4091 (Print) ISSN: 2150-4105 (Online)
http://www.scirp.org/journal/ns/

TABLE OF CONTENTS

Volume 1, Number 3, December 2009

Natural Science

Journal Information

SUBSCRIPTIONS

The *Natual Science* (Online at Scientific Research Publishing, www.SciRP.org) is published quarterly by Scientific Research Publishing, Inc.,USA.

E-mail:service@scirp.org

Subscription rates: Volume 1 2009

Print: $50 per copy.

Electronic: free, available on www.SciRP.org.

To subscribe, please contact Journals Subscriptions Department, E-mail: service@scirp.org

Sample copies: If you are interested in subscribing, you may obtain a free sample copy by contacting Scientific Research Publishing, Inc at the above address.

SERVICES

Advertisements

Advertisement Sales Department, E-mail: service@scirp.org

Reprints (minimum quantity 100 copies)

Reprints Co-ordinator, Scientific Research Publishing, Inc., USA.

E-mail: service@scirp.org

COPYRIGHT

PRODUCTION INFORMATION

For manuscripts that have been accepted for publication, please contact:

E-mail: ns@scirp.org

Vol.1, No.3, 157-165 (2009)
doi:10.4236/ns.2009.13020

Natural Science

Steps to the clinic with ELF EMF

Ash Madkan[1*], Martin Blank[2], Edward Elson[3], Kuo-Chen Chou[4], Matthew S. Geddis[5], Reba Goodman[1]

[1]Department of Pathology, Anatomy and Cell Biology, College of Physicians and Surgeons, Columbia University, New York, USA
[2]Department of Physiology and Cellular Biophysics, College of Physicians and Surgeons, Columbia University, New York, USA
[3]Department of Electrical and Computer Engineering, College Park, University of Maryland, MD, USA
[4]Gordon Life Science Institute, San Diego, California, USA
[5]Department of Science, Borough of Manhattan Community College-CUNY, New York, NY

Received 10 October 2009; revised 25 October 2009; accepted 27 October 2009.

ABSTRACT

There have been many models to identify and analyze low-frequency motions in protein and DNA molecules. It has been successfully used to simulate various low-frequency collective motions in protein and DNA molecules. Low-frequency motions in biomacromolecules originate from two common and intrinsic characteristics; i.e., they contain 1) a series of weak bonds, such as hydrogen bonds, and 2) a substantial mass distributed over the region of these weak bonds. Many biological functions and dynamic mechanisms, including cooperative effects have been reported. In this regard, some phenomenological theories were established. However, differences in experimental outcomes are expected since many factors could influence the outcome of experiments in EMF research. Any effect of EMF has to depend on the energy absorbed by a biological organism and on how the energy is delivered in space and time. Frequency, intensity, exposure duration, and the number of exposure episodes can affect the response, and these factors can interact with each other to produce different effects. In addition, in order to understand the biological consequence of EMF exposure, one must know whether the effect is cumulative, whether compensatory responses result, and when homeostasis will break down. Such findings will have great potential for use in translation medicine at the clinical level without being invasive.

Keywords: Electromagnetic Fields; Hsp70; Interaction Mechanisms; Low-Frequency Collective Motion

1. INTRODUCTION

Current investigations primarily focus on electromagnetic fields as electropollutants, e.g. cell phones, with slight regard to therapy. Electro-pollutants are manifestly different in field strength and frequency in comparison to therapeutic applications, yet the FDA fails to address differences in design, implementation and field strength, thereby considering them the same and lists therapeutic devices as ‘‘potentially dangerous’’ by association. The World Health Organization convened scientists from around the world and determined that field strengths less than 20,000 Gauss, which is lower in intensity than magnetic resonance imaging, MRI, are free of adverse side effects [1].

Regardless of device design, EMF technology has been shown to be clinically effective in bone healing [2-4], wound repair [2,5] and neural regeneration [5-10]. In terms of clinical application, EMF-induction of elevated levels of hsp70, a stress response protein, also confers protection against hypoxia [11], aids myocardial function and survival [12] as well as survival following ischemia reperfusion [12-14]. Given these results, we are particularly interested in the translational significance of effect vs. efficacy. This relationship is generally not investigated nor reported. More precise description of EM pulse, field strength intensity and sine wave parameters will provide consistency and scientific basis in reporting findings. It is contended that pulsed therapeutic fields are usually more effective if less than 20 Gauss and frequencies are less than 300 Hz, below which they are referred to as extremely low frequency (ELF) [15-18]. Cell phones are several magnitudes of order larger in both considerations. Most therapeutic ELF-EMF used for wound healing and bone repair use field strengths as small as 50 milliGauss. MRI, a diagnostic EM technology, employs static fields from 15,000 to 50,000 Gauss coupled to radiowaves for tissue penetration. In terms of molecular effects, concern might be expressed for repetitive transcranial magnetic stimulation (rTMS), an EM treatment for mental illness employing extremely low frequencies (ELF) combined with field strengths of sev-

eral thousand Gauss.

This review does not extend to the remainder of the electromagnetic spectrum (radiofrequency, microwave or infrared spectrum) though much work on the employment of these forms of energy in the treatment of neoplastic disease is currently under investigation. This research has now been employed as adjunctive therapy in clinical oncology, e.g. microwave hyperthermia. The radiofrequency and microwave parts of the spectrum are used by inserting bulk energy, whereas the ELF-EMF region is useful by producing electro-mechanical effects on target tissues, producing specific biochemical reactions.

2. THE PROMISE OF ELF-EMF IN TREATING CANCER

Since the 1980s a considerable number of reports have appeared [17,19-22] describing a great variety of cell culture systems, animal models (mice for the most part), field sources producing a variety of waveforms and field strengths, and great variation in exposure protocols. Many of the invitro (cell culture) studies of tumor-cell lines report significant cell-killing compared to control cultures. The studies involving transplantation of tumor lines into mice, frequently subcutaneously into the abdomen, report that magnetic field exposures significantly reduce the size of transplanted tumors (i.e. cyto-reduction) compared to controls. Although it is difficult to compare studies quantitatively, it is interesting that cyto-reduction occurs across a whole variety of field strengths, wave-forms, pulsed fields versus sinusoidal fields, and exposure durations. The great challenge for investigators will be to find an optimal exposure regime which delivers the most efficient cancer-cell-killing with the most minimal side-effects, to establish the role of ELF-EMF, whether as adjunctive or primary therapy, to relate its efficacy to different kinds of cancer and to the stage and grade of human cancer. This process has not actually begun but some information from animal studies is already providing some direction [23-24].

A few studies have been chosen to illuminate the value of the information they are reporting with regard to guidelines for human investigations not yet begun. It should be pointed out that although China and Russia have reported success in ELF-EMF treatments in human subjects with cancer, documentation is often weak and validation by Western science has not occurred. We can crudely separate the studies into those employing "weak" magnetic fields, not exceeding tens of micro-Tesla and those employing "strong" fields, above one milliTesla and ranging through 100 milliTesla and even up to several Tesla. This is indeed crude because other parameters of the fields, such as waveforms, time and spatial rate of variation of the fields are also critically important. For reference, the geomagnetic field is about 50 microTesla. Some house-hold appliances produce up to 1 milliTesla at a distance of 30 cm from the body, but usually for short periods. A more prolonged exposure is one to an electric blanket (60 Hertz) in which fields at the surface run from 2 to 5 microTesla [25]. These ambient exposures are considered safe.

One study of extremely low frequency (ELF) pulsed-gradient magnetic fields inhibited malignant tumor growth through different biological mechanisms [83] using a pulsed-gradient magnetic field (0.6-2.0 Tesla, gradient of 10-100 T/meter, pulse width of 20-200 milliseconds, frequency of 0.16-1.34 Hz) to exposed sarcomas inoculated into the legs of mice. These normally rapidly growing tumors showed significant shrinkage with exposure as compared with a control group. Endothelial cells of tumor blood vessels were swollen and appeared occluded and morphologic observation and biochemical tests revealed marked programmed cell death (apoptosis). Necropsy revealed no abnormalities in normal tissues.

Another study [26] exposed mice with implanted murine 16/C mammary adenocarcinoma cells to a rectified, 60 Hertz magnetic field for 10 minutes per day at 10,15 and 20 milliTesla for 12 consecutive days after a seven day period in which the cells produce visible tumors. Exposure to the fields significantly reduced tumor growth. On microscopic examination the tumor exhibited marked necrosis and evidence of inhibition of tumor vascularization. Necropsy revealed no abnormalities in the remainder of normal tissues.

De Seze *et.al.*, [27] used a 0.8 Hertz square wave 100 mT, 8 hours/day or until death on mice subjected to chemically induced tumor using benzo(a)pyrene. A significant decrease in tumor growth and increase in survival were observed.

Cameron, *et. al.* [28] transplanted a human breast cancer cell line into athymic nude mice and compared the effects of a rectified 60 Hz magnetic field signal at 15 milliTesla to that of radiation, 200 cGy of radiation every other day and found significant cyto-reduction in radiation and ELF-EMF exposed mice to a roughly comparable extent. Mice that received either therapy also had significantly fewer lung metastatic sites than did untreated mice. Normal tissues were unaffected. This study raised the question of whether ELF-EMF exposures could achieve the same efficacy as radiation but without the side effects of radiation.

Although electromagnetic technology was originally described by Maxwell in 1865, electromagnetic technology as therapy received little interest from basic scientists or clinicians until the 1980s. It now includes applications such as mitigation of inflammation (electrochemistry) and stimulation of several specific of genes [15,16]. Studies on DNA have provided an understanding of cell response to low energy EMF inputs via elec-

tromagnetically responsive elements (EMRE; EMF-sensitive base pairs nCTCTn) [19,20,29,30,84].

3. SELECTING MODEL SYSTEM FOR TRANSLATIONAL RESEARCH AND ITS CLINICAL POTENTIAL

Of under rated importance in investigating ELF EMF reactions, is the model system on which experiments are based. When extrapolating preclinical testing results to the intended clinical setting, it is important to recognize and appreciate both the relevant attributes and the limitations of a selected animal. It is essential to select a model system that will help provide an understanding of the interaction mechanism and provide specific markers for studying the effect of EMF on many diseases/ conditions including regeneration; ischemia-reperfusion, and tumor suppression. Such model systems include tissue cultured cells, Platyhelminths (worms), yeast, Diptera (flies), bacteria, fish and mice.

4. CURRENT THEORIES ON ELF-EMF INTERACTION MECHANISM

We confine the current discussion to studies of frequencies below 0.3 kHz (commonly defined as the upper limit of ELF) to magnetic fields with sinusoidal waveshapes, studies with simultaneous static magnetic fields, and studies using pulsed magnetic fields. In the many studies reported since the 1980s a variety of different exposure protocols, with variation in such parameters as magnetic field strength, frequency, duration of exposure and combined modality applications with chemotherapy and/or radiation, have been reported. Many studies have not been replicated, a general weakness of the field. But the studies taken as a whole still confer great potential promise on the role of magnetic field therapy, either as adjunctive therapy (i.e. in addition to chemotherapy or ionizing radiation) or even potentially as a primary (stand-alone) therapy for certain neoplastic diseases.

4.1. Basic Mechanisms Underlying the Efficacy of Elf-Emf Treatments.

Enough is known about the cellular and molecular mechanisms of interactions of ELF-EMF to furnish a rational basis for employing such a therapeutic modality. We describe several mechanisms for which there is some documentation and a few proposed models, not verified, which we believe are worth further investigation.

One strongly documented mechanism is the activation of apoptosis, a process characterized as programmed cell death. In response to many different stimuli, a series of biochemical cascades are activated within a cell which results in its death. From a teleological aspect such a process constitutes a defense of the organism as a whole, as a damaged cell can undergo the unregulated proliferation (lack of apoptosis) we regard as a cancerous transformation. Under the microscope such cells can show fragmentation of nuclei, bizarre appearances of nuclear chromatin, membrane blebs and cell shrinkage. Biochemically one observes the activation of a family of cysteine proteases called caspases which destroy structural elements of the cell [21]. Caspases are activated by the BCl-2 family of proteins which cause the release of cytochrome c from mitochondria into the cytoplasm by altering the mitochondrial membrane potential. Cytochrome c is considered one of the major factors in activating the caspase cascade. It has been proposed [4] that ELF-EMF can intervene in this process by affecting voltage-dependent anion channels which are used in the BCl-2 activation process. Other processes have also been described as causing increased intra-cytoplasmic calcium through voltage-activated channels as well [31]. One must bear in mind that the broad picture is far more complex, as there is a related literature showing that ELF-EMF fields also play a role in cell proliferation. Such an effect is generally associated with the weak fields, 10 microTesla to a few hundred microTesla, as opposed to higher strength fields, greater than one milliTesla, which can produce cell injury and apoptosis. It has also been reported that a static field combined with an ELF field increases apoptosis [31].

A second mechanism which has been reported from several studies is an effect of ELF-EMF which produces inhibition of new blood vessel formation. This is most dramatically observed in histological sections of tumors exposed to ELF-EMF. Malignant tumors normally elaborate angiogenic factors which cause neo-vascularization of the growing tumor, a proliferation of thin-walled capillaries branching through the tumor mass to provide nutrients to the tumor cells. The endothelial cells which form buds to new vessels from existing vessels appear to be inhibited during and following ELF-EMF exposure, a process which most likely plays a role in tumor cell death.

A few theoretical models have received much discussion over the years. One is the ion cyclotron resonance (ICR) model of McLeod and Liboff [32]. In this model free ions move in a cell membrane in a combined static and ELF magnetic field of the correct “cyclotron” frequency. This motion is thought to trigger cell signals and disrupt normal cell behavior. Another theory is that of Lednev [33] and describes the interaction of magnetic fields with ions bound to channel proteins which influence the opening and closing of the channels.

A variety of stimulative [4] effects from ELF-EMF have been found, as opposed to strong field effects described as destructive. Utilizing primarily cell culture,

time-varying magnetic fields, sinusoidal or pulsed, with frequencies in the extremely low frequency (ELF range), or repetition rates on the order of 1 to 10 Hz, have been shown to produce up-regulation of early response genes and stress response genes [4], transcription in several different cell lines [16] induction of stress response genes [34], induction of DNA synthesis in fibroblasts [32] induction of DNA synthesis in frog erythrocytes [35] and alterations in the mitotic cycle of sea urchin embryos [36]. The literature has been reviewed [25].

The model of gene regulation was believed to be that the negatively charged DNA was tightly wrapped up in the nucleus with positively charged histones, and that most genes were 'turned off' most of the time. Of course, different regions of the DNA code re being read more or less all the time to replenish essential proteins.

The ability of relatively weak EMF (in the ELF frequency range) to affect movement of electrons has been demonstrated in several specific biological reactions that are fundamental to cellular mechanisms; Na, K-ATPase reaction, the oxidation of cytochrome oxidase, and the oxidation of malonic acid (the Belousov-Zhabotinsky reaction) reviewed in [3,4]. Thus, the same fields can cause electrons to move in DNA, leading to areas of local charging and local deaggregation of DNA strands. This would set in motion the biosynthesis associated with the stresses.

This protective mechanism induces the expression of stress response genes and refolds damaged proteins to transport them across cell membranes. Specific DNA sequences on the promoter of the HSP70 stress gene are responsive to EMF, and studies with model biochemical systems suggest that EMF could interact directly with electrons in DNA. The sensitive base pairs are upstream on the HSP70 promoter and consist of the nCTCTn consensus sequence. When the EMRE are tranfected into a reporter gene, which was previously unresponsive to electromagnetic fields, they become sensitive. Studies have shown that the ERK 1-2 protein is phosphorylted when exposed to electromagnetic radiation (8 mT). A related model is that of Elson [27] which, like the model of Blank and Goodman, describes a direct electro-mechanical interaction of ELF-EMF with DNA. These theories have benefited from the results of a number of studies on the ability of DNA to conduct electric currents along the DNA backbone [38]. The phenomenon of DNA conductivity has been demonstrated in vitro using photochemical techniques and direct measurements of current flow through DNA strands using nano-techniques [39]. The phenomenon has not been demonstrated in vivo, but it has been speculated that the motion of charges in DNA could serve to protect DNA from oxidative damage. The model advocated by Elson suggests that charge motion through helical pathways could also serve to open DNA strands, producing origin sites for DNA replication. This model also indicates how very strong magnetic fields could damage DNA, which would send the signal for the induction of apoptosis. This might constitute yet another mechanism for the treatment of tumors. The model may offer an explanation for the finding of DNA strand breaks produced by electromagnetic fields as reported in a few studies [40-42].

A final mechanism first described by Dr. K. C. Chou and subsequently elaborated by both Dr. Chou and Dr. Glen Gordon [43,44] is the concept of low-frequency phonons (or internal motion) in proteins. Dr. Chou reported this mechanism in order to solve a perplexing "free-energy deficit" problem [45], which was encountered in studying the binding interaction between insulin and the insulin receptor [46]. According to the inference elaborated in [45], the wave numbers of the low-frequency phonons were in the range of $10 \sim 100\ \mathrm{cm}^{-1}$, corresponding to the range of terahertz frequency (3×10^{11} to 3×10^{12} Hz). In the mean time, the possible biological functions of low-frequency phonons in proteins were also discussed [45].

Subsequently, low-frequency modes have been indeed observed by Raman spectroscopy for a number of protein molecules [47,48] and different types of DNA [49-52]. These observed results have also been further confirmed by the neutron scattering experiments [53].

To identify and analyze this kind of low-frequency motion in protein and DNA molecules, the quasi-continuum model was developed [54-60]. It has been successfully used to simulate various low-frequency collective motions in protein and DNA molecules, such as accordion-like motion, pulsation or breathing motion, as reflected by the fact that the low-frequency wave numbers thus derived were quite close to the experimental observations [54-56,59,61]. It was also revealed through the quasi-continuum model that the low-frequency motions in biomacromolecules originate from their two common and intrinsic characteristics; i.e., they usually contain 1) a series of weak bonds, such as hydrogen bonds, and 2) a substantial mass distributed over the region of these weak bonds [62].

The most interesting fact is that many marvelous biological functions and their profound dynamic mechanisms, such as cooperative effects [60,63], allosteric transition [64,65], and intercalation of drugs into DNA [66,67], can be revealed through the low-frequency collective motion or resonance in protein and DNA molecules. In this regard, some phenomenological theories [57,65,67,68] were established. Meanwhile, the solitary wave motion was also used to address the internal motion during microtubule growth [69]. A soliton is a self-reinforcing solitary wave (a wave packet or pulse) that maintains its shape while it travels at constant speed. The relationship between the solitons and the low-frequency phonons in proteins have been discussed in a re-

cent paper [70].

As stated on the web-page of Vermont Photonics Technologies Corp. at Vermont (http://www.sover.net/~bell/newFrontierpics.htm), "Study of low-frequency (or Terahertz frequency) motions in biomacromolecules holds a very exciting potential that could lead to revolutionize biophysics, molecular biology, and biomedicine."

For a systematic introduction of the low-frequency collective motion in biomacromolecules and its biological functions, refer to a comprehensive review article [71].

4.2. Concluding Remarks on Mechanism

Direct effects on electron (or hole) flow in DNA by the models cited are not proven. It is, however, easy to visualize how ELF-EMF could damage cellular processes and structures with the documented mechanisms described. A cell is an electrolyte rich, dipolar-protein-filled water-dominated dielectric through which course many lipid membranes filled with voltage-gated and other types of channels designed for transmitting biochemical signals. It is easy to visualize how such a system could be affected by low frequency, strong time-varying magnetic fields and their associated electric fields, and so most attention has been focused on effects on electrolyte flow, protein dipole responses, and signal transduction at membranes. One interesting study used pulsed electric fields (not magnetic fields), a burst of high voltage, 40 kiloVolt/cm, 300 nanosecond wide pulses to produce complete destruction of focal melanomas injected subcutaneously into mice [72]. Because electrodes must be placed on either side of the tumor there are severe practical restrictions on the applicability of such a technology to tumors in general, but such an approach can yield valuable information on the strength of the fields required to produce tumor destruction. The general conception has been that it is the electrical fields, not the magnetic fields per se that couple into biological structures to produce an effect. Consequently the pulsed electric field experiment can provide valuable information on the magnetic field parameters required to produce an effective electric field.

One must be cognizant, however, that the studies and models of Blank, Goodman, and Elson have raised the possibility that coupling of electromagnetic energy can occur as well directly through the magnetic fields. This possibility can be explained by the expressions F = qv X B and curl E = dB/dt of classical electromagnetism, and remembering that a cell is filled with currents through membranes virtually at all times and possibly currents through DNA as well. The technology is available to fashion waveforms with far faster rise-times, shorter pulse-widths, far higher field strengths, varying repetition rates and burst modes than have been studied. In view of the fact that no adverse side-effects have been found and no abnormalities in normal tissue have been identified to date (possibly a very significant advantage over chemotherapy and conventional radiation) exciting opportunities are visible.

In view of these many interesting possibilities, and the promise communicated by the existing literature, a very strong case can and should be made for an investment into the potential of ELF-EMF in cancer therapeutics.

5. EMF-DNA INTERACTION MECHANISMS: SIGNALING PATHWAYS

The initial step in transmitting extracellular information from the plasma membrane to the nucleus of the cell is by NADH oxidase [73]. NADH then rapidly generates reactive oxygen species (ROS). These ROS stimulate matrix metalloproteinases which allows them to cleave and release heparin binding epidermal growth factor. This secreted factor actives the epidermal growth receptor which in turn activates the ERK cascade [73].

The major mechanism that regulates transcriptional activity in response to extracellular stimuli is the activation of the mitogen-activated protein kinase (MAPK) signaling cascades. There are three MAPK cascades that are implicated in exposures to ELF and RF. They are: 1) extracellular signal regulated kinase 1\2 (ERK), 2) c-Jun-terminal kinase (JNK), stress actrivated protein kinase (SAPK) and p38SAPK. Each of the cascades is composed of three to six tiers of protein kinases and their signals are transmitted by sequential phosphorylation and activation of the protein kinases in each of the tiers. Upon activation the protein kinases in various tiers phosphorylated and activated a large number of regulatory proteins which include a set of transcription factors, e.g., c-Jun, c-Fos, hsp27 and hsp70. Activation of the stress response is accompanied by activation of specific signal transduction cascades involved in regulating cell proliferation, differentiation and metabolism [74-77]. The MAPK pathways have been characterized in several cell types [74,78-81]. Exposure to nonthermal EMF as well as RF affects the expression of many cellular proteins [73-75].

The initial step in transmitting extracellular information from the plasma membrane to the nucleus of the cell is by NADH oxidase [73]. NADH then rapidly generates reactive oxygen species (ROS). These ROS stimulate matrix metalloproteinnases which allows them to cleave and release heparin binding epidermal growth factor. This secreted factor activates the epidermal growth receptor which in turn activates the ERK cascade [73].

Both EMF and RF activate the upregulation of the HSP70 gene and the induction of elevated levels of the hsp70 protein. This effect on RNA transcription and

protein stability is controlled by specific protein transcription factors which are elements of the mitogen-activated-phospho-kinase (MAPK) cascade.

EMF also stimulate serum response factor which binds to the serum response element (SRE) through ERKmapk activation and is associated with injury and repair in *in vivo* and *in vitro*. The SRE site is on the promoter of an early response gene, c-fos, which under specific cellular circumstances has oncogenic properties. The c-fos promoter is EMF-sensitive; a 20 min exposure to 60Hz 80mG sinusoidal fields significantly increased c-*fos* gene expression [82]. The SRE accessory protein, Elk-1, contains a growth-regulated transcriptional activation domain. ERK phosphorylation potentiates Elk-1 and transactivation at the c-*fos* SRE [8]. ELF-EMF exposure may also control protein regulation through the PI3-kinase pathway as inhibition results in an upregulation of collagen in response to ELF-EMF, suggesting an inhibitory role for PI3K in ELF-EMF induction. Furthermore, the role of nitric oxide/ cGMP signaling pathway has been implicated in pulsed EMF induced chondrocyte proliferation.

In studying human disorders, such as cancer, a stronger emphasis should be placed on model systems and noninvasive techniques for patient safety and ease of application for the treating physician. Information from the laboratory bench on non-human model organisms is under appreciated and very important.

REFERENCES

[1] M. H. Repacholi and B. Greenebaum, (1999) Interaction of static and extremely low frequency electric and magnetic fields with living systems: Health effects and research needs. Bioelectromagnetics. **20(3)**, 133-60.

[2] C. A. L. Bassett, (1995) Bioeletromagnetics in the service of medicine. Adv Chem, **250**, 261-276.

[3] M. Blank and R. Goodman, (2004) Initial Interactions in Electromagnetic Field-Induced Biosynthesis. J. Cellular Physiology, **199**, 359-363.

[4] M. Blank and R. A. Goodman, (2008) Mechanism for stimulation of biosynthesis by electromagnetic fields: Charge transfer in DNA and base pair separation. Journal of Cellular Physiology.

[5] H. Ito and C. A. Bassett, (1983) Effect of weak, pulsing electromagnetic fields on neural regeneration in the rat. Clin Orthop Relat Res, **181**, 283-290.

[6] M. Jin, H. Lin, L. Han, M. Opler, S. Maurer, M. Blank, and R. Goodman, (1997) Biological and technical variables in myc expression in HL60 cells exposed to 60 Hz electromagnetic fields. Bioelectrochemistry and Bioenergetics, **44**, 111-120.

[7] F. Shao, K. Augustyn, and J. K. Barton, (2005) Sequence dependence of charge transport through DNA domains. J Am Chem Soc, **127**, 17445-17452.

[8] B. F. Sisken, M. Kanje, G. Lundborg, E. Herbst, and W. Kurtz, (1989) Stimulation o frat sciatic nerve regeneration with pulsed electromagnetic fields. Brain Res, **485**, 309-316.

[9] B. F. Sisken, J. Walker, and M. Orgel, (1993) Prospects on clinical applications of electrical stimulation for nerve regeneration. J Cell Biochem, **51**, 404-409.

[10] J. L. Walker, J. M. Evans, P. Meade, P. Resig, and B. F. Sisken, (1994) Gait-stance duration nas a measure of injury and recovery in the rat sciatic nerve model. J Neurosci Methods, **52**, 47-52.

[11] J. M. Shallom, A. L. DiCarlo, D. Ko, L. M. Penafiel, and A. Nakai, (2002) Microwave exposure induces hsp70 and confers protection against hypoxia in chick embryos. J Cell Biochem, **86**, 490-496.

[12] I. George, M. Geddis, Z. Lill, H. Lin, T. Gomez, M. Blank, M. Oz, and R. Goodman, (2008) Myocardial function improved by electromagnetic fields induction of stress protein hsp70. J Cellular Physiol, **216**, 816-823. Published Online: DOI: 10.1002/jcp.21461.

[13] A. Albertini, B. Zucchini, G. Noera, R. Cadossi, C. P. Napoleone, and A. Pierangeli, (1999) Protective effect of low frequency low energy policy electromagnetic fields on acute experimental myocardial infarcts in rats. Bioelectromagnetics, **20**, 372-377.

[14] A. Di Carlo, J. M. Farrell, and T. Litovitz, (1998) A simple experiment to study electromagnetic field effects: Protection induced by short-term exposures to 60Hz magnetic fields. Bioelectromagnetics, **19**, 498-500.

[15] R. Goodman and A. Henderson, (1988) Exposure of salivary gland cells to low frequency electromagnetic fields alters polypeptide synthesis. PNAS, **85**, 3928- 3932.

[16] R. Goodman, C. A. L. Bassett, and A. Henderson, (1983) Pulsing electromagnetic fields induce cellular transcription. Science, **220**, 1283-1285.

[17] R. Goodman, M. Blank, H. Lin, O. Khorkova, L. Soo, D.Weisbrot, and A. S. Henderson, (1994) Increased levels of hsp70 transcripts are induced when cells are exposed to low frequency electromagnetic fields. Bio- electrochem Bioenerg, **33**, 115-120.

[18] R. Goodman and M. Blank, (1998) Magnetic field stress induces expression of hsp70. Cell Stress and Chaperones, **3**, 79-88.

[19] H. Lin, M. Blank, K. Rossol-Haseroth, and R. Goodman, (2001) Regulating genes with electromagnetic response elements. J Cell Biochem, **81**, 143-148.

[20] H. Lin, M. Head, M. Blank, L. Han, M. Jin, and R. Goodman, (1998) Myc-mediated transactivation of HSP70 expression following exposure to magnetic fields. J Cell Biochem, **69**, 181-188.

[21] R. Palumbo, D. Capasso, F. Brescia, P. Mita, M. Sari, F. Bersani, and M. R. Scarfi, (2006) Effects on apoptosis and reactive oxygen species formation by Jurkat cells exposed to 50 Hz electromagnetic fields. Bioelec- tromagnetics, **27**, 159-162.

[22] S. Tofani, D. Barone, M. Cintorino, M. M. de Santi, A. Ferrara, R. Orlassino, P. Ossola, F. Perogio, K. Rolfo, and F. Ronchetto, (200l) Static and ELF magnetic fields induce tumor growth inhibition and apoptosis. Bioelectromagnetics, **22**, 419-428.

[23] E. Elson, (2009) The little explored efficacy of magnetic fields in cancer treatment, and postulation of the mechanism of action. Electromagnetic Biology and Medicine, in press.

[24] E. D. Kirson, V. Dbalý, F. Tovaryš, J. Vymazal, J. F. Soustiel, A. Itzhaki, D. Mordechovich, S. S. Shirley, Z. Gurvich, R. chneiderman, Y. Wasserman, M. Salzberg, B. Ryffel, D. Goldsher, E. Dekel, and Y. Palti, (2007) Alternating electric fields arrest cell proliferation in animal tumor models and human brain tumors. PNAS, **104**, 10152-10157.

[25] C. Polk and E. Postow, (1996) Eds. Handbook of Biological Effects of Electromagnetic Fields. 2nd Ed, CRC Press, Chapter 4.

[26] C. D. William, M. S. Markov, W. E. Hardman, and I. L. Cameron, (2001) Therapeutic electromagnetic field effects on angiogenesis and tumor growth. Anticancer Research, **21**, 3887-3892.

[27] R. De Seze, S. Tuffet, J. M. Moreau, and B. Veyret, (2000) Effects of 100 mT time varying margnetic fields on the growth of tumors in mice. Bioelectromagnetics, **21**, 107-111.

[28] I. L. Cameron, L. Z. Sun, N. Short, W. E. Hardman, and C. D. Williams, (2005) Therapeutic electromagnetic field [TEMF] and gamma irradiation on human breast cancer xenograft growth, angiogenesis and metastasis. Cancer Cell International, **5(23)**.

[29] D. Kultz, (2005) Molecular and evolutionary basis of the cellular stress response. Ann Rev Physiol, **67**, 225-257.

[30] J. Topol, D. M. Ruden, and C. S. Parker, (1985) Sequences required for in vitro transcriptional activation of a drosophila hsp70 gene. Cell, **42**, 527-537.

[31] M. T. Santini, A. Ferrante, G. Rainaldi, P. Indovina, P. L. Indovina, (2005) Extremely low frequency magnetic fields and apoptosis: A review. International Journal of Radiation Biology, **81**, 1-11.

[32] A. R. Liboff, (1998) Electric-field ion cyclotron resonance. Bioelectromagnetics, **18**, 85-87.

[33] V. V. Lednev, (1993) Possible mechanism for the effect of weak magnetic fields on biological systems: Correction of the basic expression and it consequences. Electricity and Magnetism in Biology and Medicine, Blank, M. Ed. San Francisco Press, San Francisco, 550- 552.

[34] S. Kwee, P. Raskmark, and S. Velizarov, (2001) Changes in cellular proeins due to environmental non-ionizing radiation. I. Heat-shock proteins. Electro- and Magnetobiology, **20**, 141-152.

[35] M. Grattarola, A. Chiabrera, R. Vlvianl, and G. Parodl, (1985) Interactions between weak electromagnetic fields and biosystems: A summary of nine years of research, **4 (1)**, 211-226.

[36] L. Michael and S.G. Ernst, (2005) Applied AC and DC magnetic fields cause alterations in the mitotic cycle of early sea urchin embryos. **4(6)**, 231 – 240.

[37] E. Elson, (2007) Developmental control in animals and a biological role for DNA charge transfer. Progress in Biophysics & Molecular Biology, **95**, 1-15.

[38] E. J. Merino, A. K. Boal, and J. K. Barton, (2008) Biological contexts for DNA charge transport chemistry. Current Opinion in Chemical Biology, **12**, 229-237.

[39] C. Wan, T. Fiebig, S. O. Kelley, C. R. Treadway, and J. K. Barton, (1999) Femtosecond dynamics of DNA-mediated electron transfer. Proc Nat Acad Sci, USA, **96**, 6014-6019.

[40] H. Lai and N. P. Singh, (2004) Magnetic-field-induced DNA strand breaks in brain cells of the rat. Environmental Health Perspectives, **112**, 687-94.

[41] H. Lai and N. P. Singh, (1997) Acute exposure to a 60Hz magnetic field increases DNA strand breaks in rat brain cells. Bioelectromagnetics, **18**, 156-165.

[42] H. Lai and N. P. Singh, (2005) Interaction of microwaves and a temporally incoherent magnetic field on single and double DNA strand breaks in rat brain cells. Electromag Biol Med, **24**, 23-29.

[43] G. Gordon, (2007) Designed electromagnetic pulsed therapy: Clinical applications. Journal of Cellular Physiology, **212**, 579-582.

[44] G. Gordon, (2008) Extrinsic electromagnetic fields, low frequency (phonon) vibrations, and control of cell function: A non-linear resonance system. Journal of Biomedical Science and Engineering *(JBiSE)*, **1**, 152-156. (open accessible at http://www.srpublishing.org/journal/jbise/).

[45] K. C. Chou and N. Y. Chen, (1977) The biological functions of low-frequency phonons. Scientia Sinica, **20**, 447-457.

[46] C. Chothia and J. Janin, (1975) Principles of protein-protein recognition. Nature, **256**, 705-708.

[47] P. C. Painter and L. E. Mosher, (1979) The low-frequency Raman spectrum of an antibody molecule: Bovine IgG. Biopolymers, **18**, 3121-3123.

[48] P. C. Painter, L. E. Mosher, and C. Rhoads, (1981) Low-frequency modes in the Raman spectrum of DNA. Biopolymers, **20**, 243-247.

[49] P. C. Painter, L. E. Mosher, and C. Rhoads, (1982) Low-frequency modes in the Raman spectra of proteins. Biopolymers, **21**, 1469-1472.

[50] H. Urabe and Y. Tominaga, (1982) Low-frequency collective modes of DNA double helix by Raman spectroscopy. Biopolymers, **21**, 2477-2481.

[51] H. Urabe, Y. Tominaga, and K. Kubota, (1983) Experimental evidence of collective vibrations in DNA double helix Raman spectroscopy. Journal of Chemical Physics, **78**, 5937-5939.

[52] H. Urabe, Y. Sugawara, M. Ataka, and A. Rupprecht, (1998) Low-frequency Raman spectra of lysozyme crystals and oriented DNA films: Dynamics of crystal water. Biophys J, **74**, 1533-1540.

[53] P. Martel, (1992) Biophysical aspects of neutron scattering from vibrational modes of proteins. Prog Biophys Mol Biol, **57**, 129-179.

[54] K. C. Chou, (1983) Low-frequency vibrations of helical structures in protein molecules. Biochemical Journal, **209**, 573-580.

[55] K. C. Chou, (1983) Identification of low-frequency modes in protein molecules. Biochemical Journal, **215**, 465-469.

[56] K. C. Chou, (1984) Low-frequency vibration of DNA molecules. Biochemical Journal, **221**, 27-31.

[57] K. C. Chou, (1984) The biological functions of low-frequency phonons: 4. resonance effects and allosteric transition. Biophysical Chemistry, **20**, 61-71.

[58] K. C. Chou, (1985) Prediction of a low-frequency mode in BPTI. International Journal of Biological Macromolecules, **7**, 77-80.

[59] K. C. Chou, (1985) Low-frequency motions in protein molecules: Beta-sheet and beta-barrel. Biophysical Journal, **48**, 289-297.

[60] K. C. Chou, (1989) Low-frequency resonance and co-

operativity of hemoglobin. Trends in Biochemical Sciences, **14**, 212.
[61] K. C. Chou, G. M. Maggiora, and B. Mao, (1989) Quasi-continuum models of twist-like and accordion-like low-frequency motions in DNA. Biophysical Journal, **56**, 295-305.
[62] K. C. Chou, (1986) Origin of low-frequency motion in biological macromolecules: A view of recent progress of quasi-continuity model. Biophysical Chemistry, **25**, 105-116.
[63] K. C. Chou, N. Y. Chen, and S. Forsen, (1981) The biological functions of low-frequency phonons: 2. Co-operative effects. Chemica Scripta, **18**, 126-132.
[64] K. C. Chou, (1984) The biological functions of low-frequency phonons: 3. Helical structures and micro-environment. Biophysical Journal, **45**, 881-890.
[65] K. C. Chou, (1987) The biological functions of mechanism of allosteric transition in antibody molecules. Biopolymers, **26**, 285-295.
[66] K. C. Chou and G. M. Maggiora, (1988) The biological functions of low-frequency phonons: 7. The impetus for DNA to accommodate intercalators. British Polymer Journal, **20**, 143-148.
[67] K. C. Chou and B. Mao, (1988) Collective motion in DNA and its role in drug intercalation. Biopolymers, **27**, 1795-1815.
[68] K. C. Chou, and Y. S. Kiang, (1985) The biological functions of low-frequency phonons: 5. A phenomenological theory. Biophysical Chemistry, **22**, 219-235.
[69] K. C. Chou, C. T. Zhang, and G. M. Maggiora, (1994) Solitary wave dynamics as a mechanism for explaining the internal motion during microtubule growth. Biopolymers, **34**, 143-153.
[70] Z. Sinkala, (2006) Soliton/exciton transport in proteins. J Theor Biol, **241**, 919-927.
[71] K. C. Chou, (1988) Review: Low-frequency collective motion in biomacromolecules and its biological functions. Biophysical Chemistry, **30**, 3-48.
[72] R. Nuccitelli, X. Chen, A. F. Pakhomov, W. H. Baldwin, S. Sheik, J. L. Pomicter, W. Ren, C. Osgood, R. J. Swanson, J. F. Kolb, S. J. Beebe, and K. H. Schoenbach, (2009) A new pulsed electric field therapy for melanoma disrupts the tumor's blood supply and causes complete remission without recurrence. Internal Journal of Cancer, **125**, 438-445.
[73] J. Friedman, S. Kraus, Y. Hauptman, Y. Schiff, and R. Seger, (2007) Mechanism of short-term ERK activation by electromagnetic fields at mobile phone frequencies. Biochem J., **405**, 559-568.
[74] M. Jin, M. Blank, and R. Goodman, (2000) ERK1/2 Phosphorylation, Induced by Electromagnetic Fields, Diminishes During Neoplastic Transformation. Journal of Cellular Biochemistry, **78**, 371-379.
[75] D. Leszczynski, S. Joenvaara, J. Reivinen, and R. Kuokka, (2002) Non-thermal activation of the hsp27/p38MAPK stress pathway by mobile phone radiation in human endothelial cells: Molecular mechanism for cancer-and blood-brain barrier-related effects. Differentiation, **70**, 120-129.
[76] M. Simko, (2004) Induction of cell activation processes by low frequency electromagnetic fields. Scientific World Journal, Suppl 2, **4,** 4-22.
[77] M. Simko, C. Hartwig, M. Lantow, M. Lupke, M. O. Mattsson, Q. Rahman, and J. Rollwitz, (2006) Hsp70 expression and free radical release after exposure to non-thermal radio-frequency electromagnetic fields and ultrafine particles in human Mono Mac 6 cells. Toxicol Lett. **161**, 73-82.
[78] R. Marais, J. Wynne, and R. Treisman, (1993) The SRF accessory protein Elk-1 contains a growth factor-regulated transcriptional activation domain. Cell, **73**, 381-393.
[79] R. Janecht, W. H. Ernst, V. Pigoud, and A. Nordheim, (1993) Activation of TCF Elk-1 by MAP Kinases. EMBO J., **12**, 5097-5104.
[80] H. Gille, M. Kortenjann, O. Thomae, C. Moomaw, C. Slaughter, M. H. Cobb, and P. E. Shaw, (1995) ERK phosphorylation potentiates Elk-1-mediated ternary complex formation and transactivation. EMBO J., 14, 951-962.
[81] V. Sgambato, P. Vanhouttte, C. Pages, M. Rogard, L. Hipskind, M. J. Besson, and J. Caboche, (1998) In vivo expression and regulation of Elk-1, a target of the extracellular-regulated kinase signaling pathway, in the rat brain. J. Neurosci., **18**, 214-226.
[82] S. Rao and A. S. Henderson, (1996) Regulation of c-fos is affected by electromagnetic fields. J Cell Biochem, **63**, 358-365.
[83] X. Zhang, H. Zhang, C. Zheng, C. Li, X. Zhang, and W. Xiong, (2002) Cell Biology International, **26**, 599-603.
[84] H. Lin, M. Blank, and R. Goodman, (1999) A magnetic field responsive domain in the human HSP70 promoter. J Cell Biochem., **75**, 170-176.

Literature Cited

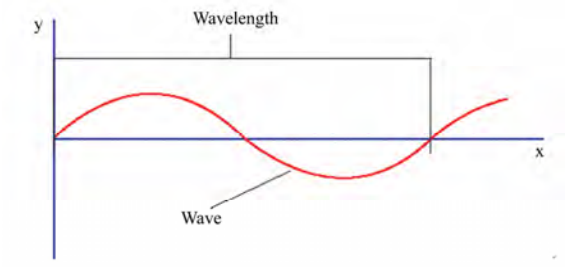

Legend: To facilitate an understanding of mechanisms, definition of the following terms should be helpful.

Wave - A wave is a disturbance traveling through a medium by which energy is transferred from one particle of the medium to another without causing any permanent displacement of the medium itself. The peaks of the wave are the maximum amount of energy.

Longitudinal Wave - a longitudinal wave is like a sound wave in air, where the pulse travels parallel to the direction of disturbance.

- Transverse Wave - a transverse wave is like a leaf floating in a lake. When a wave comes, the leaf goes up and then back down. So a transverse wave is where the motion is perpendicular to the direction of disturbance.
- Wavelength – A wavelength is the distance between any two repeating points, as shown in the diagram.
- Rise Time: The speed with which a pulse goes from zero to peak
- Measurement of field strength: Tesla/Gauss measure: 1 Tesla equals 10,000 gauss
- Frequency – The frequency of a wave is the number of times a point repeats in a certain amount of time.

While EMF signals come in various shapes (sine and square, pulsed etc.) through a sine wave or a series of sine waves. The delivery system of an electromagnetic field can be single pulse, repetive pulse and can be through Helmholtz and other coil configureation.

To understand the impact of EMF on cells and tissues it is important to understand specific acronyms. These include pulsed electromagnetic field (PEMF), time varying electromagnetic field (TVEMF) to pulsed electric stimulation (PES) and pulsed electromagnetic therapy (PEMT). The need to specifically design pulse and/or static field for maximal bio-efficacy.

Vol.1, No.3, 166-175 (2009)
doi:10.4236/ns.2009.13021

Ion exchange recovery of palladium (II) from nitrate weak acidic solutions

Olga N. Kononova[1*], Nataliya G. Goryaeva[1], Olga V. Dychko[1]

[1]Department of Chemistry, Siberian Federal University, Krasnoyarsk, Russian Federation; cm2@bk.ru

Received 12 August 2009; revised 2 September 2009; accepted 4 September 2009.

ABSTRACT

Sorption recovery of palladium (II) from nitrate weak acidic model solutions and solutions of spent catalysts on some ion exchangers with different physical and chemical structure has been investigated. The palladium concentration in contacting solutions was $5.0 \cdot 10^{-5}$ – $1.0 \cdot 10^{-3}$ mol/L at nitric acid and potassium nitrate concentrations 0.01 and 1.0 mol/L, respectively. It was shown that anion exchangers AV-17-8 as well as Purolite S 985 and A 500 possess the best sorption and kinetic properties. These sorbents can be recommended for selective recovery of palladium from solutions of spent catalysts.

Keywords: Palladium; Ion Exchange; Anion Exchangers; Nitrate Solutions

1. INTRODUCTION

As natural deposits of precious metals are being depleted, the technologies for precious metals recovery from different secondary raw materials are becoming more important. The hydrometallurgical methods are successfully used for these purposes [1-3]. One of the most promising methods for recovery of platinum group metals (in particular, of palladium) is sorption, characterized by high efficiency and selectivity [1,3-5]. However, the majority of investigations devoted to the sorption recovery of palladium, deal with chloride or sulfate solutions [6-14], and the studies of sorption of noble metals from nitric acidic media are rather limited [1,15-20]. At the same time, the recovery of palladium from some kinds of secondary sources (e.g. electronic scrap and exhausted nuclear fuel) requires its isolation from nitric acidic and nitrate solutions [1,21].

Our previous investigations were focused on sorption recovery of palladium from chloride model solutions and solutions of spent catalysts by various ion exchangers and carbon adsorbents [9,22,23]. Apart from this, we started the research of sorption concentration of palladium on carbon adsorbents during its recovery from model nitric acidic solutions [24]. We have revealed high sorption abilities of some carbon adsorbents to palladium (II) ions depending on initial concentrations of nitric acid and $Pd(II)$.

The present paper is focused on sorption recovery of palladium from nitrate weak acidic solutions (model and of spent catalysts) by some ion exchangers with different physical and chemical structure.

2. MATERIALS AND METHODS

2.1. Characteristics of Ion Echangers

Some ion exchangers from various manufacturers were taken for investigation. These sorbents possess different physical and chemical structure. Their physical-chemical characteristics are summarized in **Table 1**. It should be noted that ion exchangers produced by Purolite Company for the first time were used for recovery of platinum group metals. However, these ion exchangers were successfully applied in our previous investigations on sorption recovery of gold and silver [25].

Before sorption all the ion exchangers were prepared according to the standard procedures and then loaded with 1 M $NaCl$ solution, in order to convert them to chloride form (anion exchangers) or to Na^+, Cl^--form (amphoteric resin).

The acid-base properties of ion exchangers investigated were studied by a potentiometric titration with the glass electrode. Based on the experimental data obtained, we have calculated the average apparent ionization constants of functional groups of ion exchangers [5]. The calculation procedure is described below and the values of constants are presented in **Table 1.**

2.2. Preparation of Palladium Ntrate Solutions

The initial model stock solution of palladium was prepared according to works [26,27]. The accurately

Table 1. Physical-chemical properties of ion exchangers investigated.

Trade name	Exchanger type	Copolymer	Physical structure	Functional groups	Exchange capacity to Cl^- ion (mmol/g)	Swelling grade (%)	$p\overline{K_a}$	Manufacturer
Purolite A 500	Strong base anion exchanger	St – DVB	MP	QAB	1.2	15	2.31	Purolite, UK
Purolite A 530	Strong base anion exchanger	St – DVB	MP	QAB	0.60	12	1.15	Purolite, UK
Purolite S 985	Weak base anion exchanger	Ac – DVB	MP	PA	2.3	42	0.74	Purolite, UK
AV-17-8	Strong base anion exchanger	St – DVB	G	QAB	3.6	23	0.99	TOKEM, Russia
AN-25 1	Weak base anion exchanger	VP – DVB	MP	TAG, PN	5.3	10	1.78	Chercassy, Ukraine
ANKF-5	Amphoteric ion exchanger	VP – DVB	P	PAG, TAG, PN	3.8 (2.6 to Na^+)	22	1.42 ($p\overline{K_b}$ =1 1.83)	Chercassy, Ukraine

St-styrene; DVB-divinylbenzene; Ac-acryl; VP-vinylpyridine; MP-macroporous; G-gel; P-porous; QAB-quaternary ammonium base; PA-polyamine; TAG-tertiary aminogroups; PAG-phosphorylic acid groups; PN-pyridine nitrogen.

weighed metallic palladium (0.50 g) was dissolved under heating in concentrated HNO_3 (analytical grade) according to the following reaction:

$$3Pd + 8HNO_3 \rightarrow 3Pd(NO_3)_2 + 2NO\uparrow + 4H_2O \quad (1)$$

The palladium concentration in initial stock solution was 0.01 mol/L. The working solutions with palladium concentrations $5.0 \cdot 10^{-5} – 1.0 \cdot 10^{-3}$ mol/L were prepared from the stock solution. The nitric acid concentration in these solutions was 0.01 mol/L and the constant ionic strengths was made by means of 1.0 M KNO_3. Before the preparation of working solutions, the palladium concentration in initial stock solution was controlled by gravimetric method with dimethylglyoxime as a reagent [26]. The palladium (II) concentration in working solutions and in solutions after sorption was determined by spectrophotometrical with nitroso-R-salt [27,28].

We chose the range of palladium and nitric acid concentrations for our experiment, aiming to make it closer to real industrial conditions.

Apart from the model nitrate solutions of palladium, we also used the solutions of spent palladium-containing catalysts. These solutions were prepared as follows: the catalyst quantities (0.20 g) were dissolved under heating in concentrated nitric acid, similar to preparation of model solution. The working solutions of spent catalysts with palladium concentrations $5.0\ 10^{-5}$–$5.0\ 10^{-4}$ mol/L were prepared from the initial solution. Before dissolution of spent catalysts samples in nitric acid, we have determined their average composition by X-ray-fluorescence method. The results are represented in **Table 2.**

2.3. Batch Studies

The sorption of palladium was studied under batch experimental conditions: resin mass–0.20 g, volume of contacting solution–20.0 mL, stirring in a thermostat at (20 ± 1) ºC. The equilibrium time determined by special tests was about 24 h.

Sorption ability of ion exchangers investigated was estimated by means of the recovery degree ($R,\%$) and distribution coefficient ($D, L/g$), which were calculated from:

$$R = \frac{(C_0 - C_{eq})}{C_0} \cdot 100\% \quad (2)$$

$$D = \frac{EC}{C_{eq}} \quad (3)$$

where C_0 and C_{eq} are the initial and equilibrium molar concentrations of palladium solution; EC is the exchange capacity of the resin for palladium, mmol/g.

The kinetics of sorption of palladium from weak acidic nitrate solutions on ion exchangers investigated was studied by the “limited bath” method [29,30] and diffusion coefficients of $Pd(II)$ ($\overline{D_s}, cm^2/s$) were calculated. The kinetic experiment procedure is described below.

The desorption of palladium was carried out by 1 M thiourea solution in 0.01 M HNO_3 or in 1 M $NaOH$. The mechanism of palladium sorption recovery by ion exchangers from nitrate systems was studied by means of IR-spectroscopy and diffuse reflectance spectroscopy. The preparation procedures of samples are present below.

Table 2. Average composition of initial sample of palladium-containing spent catalyst.

Component	Content (%)
Palladium	0.79
Sodium	0.41
Aluminum oxide	~ 84
Silicon	0.03
Sulfur	0.12
Chlorine	0.80
Iron	0.19
Nickel	< 0.02
Zinc	< 0.02
Gallium	< 0.02

All the results were statistically processed by standard methods [31,32]. The average experimental error for 3-4 parallel runs was below 6 %.

2.4. Calculation of Apparent Constants of Acid-Base Ionization of Ion Exchangers

The constants values were calculated using potentiometric titration data. For each point of the titration curve, the functional groups content was determined and the apparent ionization degree (α) of the resin was calculated:

$$\alpha = \frac{\overline{[H^+]}}{C_0} \tag{4}$$

where $\overline{[H^+]}$ is the equilibrium concentration of H^+ ions in the ion exchanger phase, mmol/mL; C_0 is the initial concentration of the titrant solution (0.1 M HCl).

Then a curve was plotted on the coordinates $pH = f(\log\frac{\alpha}{1-\alpha})$ and at $\alpha = 0.5$, the apparent acid-base ionization constants of functional groups of the ion exchangers ($p\overline{K_a}$) were calculated from Henderson's equation:

$$p\overline{K_a} = pH - m\log(\frac{\alpha}{1-\alpha}) \tag{5}$$

where m is the slope angle tangent of the curve.

2.5. "Limited Bath" Method for Sorption Kinetics of Palladium (Ii)

The quantities of preswollen resin (0.10 g) were stirred with 25.0 mL of palladium nitrate solutions at (20 ± 1)ºC over a period of 30 s to 24 h. The suspensions were intensively stirred (more than 800 rev/min). After a certain time period, the resins and solutions were quickly separated and the concentration of $Pd(II)$ was determined in the solutions. Then the exchange degree (F) was calculated from

$$F = \frac{Q_t}{Q_\infty} \tag{6}$$

where Q_t and Q_∞ are the amounts (in mmol) of the palladium sorbed to the time t (s) and to the equilibrium time.

According to the Boyd's method [29,30,33], the kinetic coefficient B was calculated from

$$B = \frac{(1.08)^2 \cdot F^2}{t} \tag{7}$$

The data obtained were plotted as a function $Bt = f(t)$. If the process is controlled by gel diffusion [29,30,33], this function should be linear. After that, the diffusion coefficients ($\overline{D_s}$) were calculated according to the equation:

$$\overline{D_s} = \frac{Br^2}{\pi^2} \tag{8}$$

where r is the radius of the resin grain (cm).

The half-exchange time of the kinetic process ($t_{1/2}$) was calculated as follows:

$$t_{1/2} = \frac{r^2}{4\pi^2 \overline{D_s}} \tag{9}$$

2.6. Preparation of Sample for FT-IR-Spectroscopy

IR–spectra of ion exchangers investigated were recorded by means of FT-IR- spectrometer Vector 22 (Bruker). Before that, ion exchanger samples were dried during 4 h at 40ºC in convection drier. Then the samples were held in a vacuum-desiccator over freshly calcinated calcium chloride. The specimens were ground in a mechanical mill without air access and after that were pressed with spectrally pure KBr to discs. The quantities of resin samples and potassium bromide were constant (200 mg each of resin and KBr).

2.7. Preparation of Samples for Diffuse Reflectance Spectroscopy

The diffuse reflectance spectra were recorded by means of spectrometer PULSAR (Russia). The resin quantities (0.20 g) were preliminary saturated with palladium (II) ions with concentration $5.0 \cdot 10^{-4}$ mol/L during 24 h. After that, the resins were filtered and wet samples were placed into cell. Then the diffuse reflectance spectra

were recorded.

3. RESULTS AND DISCUSSIONS

3.1. Ionic State of Palladium in Contacting Solutions

It is known from [26,27,34,35] that the ionic state of platinum group metals in solutions depends on acidity of contacting solution as well as on concentration of chloride or nitrate ions (for chloride and nitrate systems, respectively). It is determined at present that $Pd(NO_3)_2 \cdot (H_2O)_2$ is formed after the dissolution of metallic palladium in concentrated nitric acid according to reaction (1) and subsequent diluting of the solution obtained [36,37]. It is also determined [38] that the hydrated palladium (II) ions $[Pd(H_2O)_4]^{2+}$ and their mononitrate complexes $[PdNO_3]^+$ are present in solution at $C_{HNO_3} \geq 1$ mol/L. With the increase in nitric acid con- centration, the amount of different nitrate cationic and anionic complexes as well as of neutral species is growing [19,20]: $[Pd(H_2O)_3NO_3]^+$, $[Pd(H_2O)_2(NO_3)_2]$, $[Pd(H_2O)(NO_3)_3]^-$, $[Pd(NO_3)_4]^{2-}$. When the nitric acid concentration diminishes from 1 mol/L to 0.01 – 0.001 mol/L, the formation of hydroxocomplexes with the general formula $[Pd(OH)_n]_{aq}^{(2-n)^+}$ is observed in solution [36,38]. That occurs due to the so-called "aging" of solutions, which takes place in weak acidic media, and especially after keeping of such solutions for longer than 24 h. This phenomenon is typical for solutions of platinum group metals [27,34,38]. At $C_{HNO_3} \leq 0.001$ mol/L, the solution does not contain aquatic $Pd(II)$ ions and its nitrate complexes, and only hydroxocomplexes of different composition exist in this media [38].

The above discussion concerns only the $Pd(II) - HNO_3$ systems, i.e. without adding background electrolytes. Our previous investigation [24] was focused on palladium (II) recovery from strong acidic solutions (C_{HNO_3} was 1, 2 and 5 mol/L) in the system sorbent $- Pd(II) - HNO_3$. However, the sorption of palladium from weak acidic solutions in the presence of salt background is also of practical interest, since such media are formed in number of technological schemes [1,3]. Therefore, we have also studied the following system: ion exchanger $- Pd(II) -$ 0.01 M $HNO_3 -$ 1 M KNO_3. It should be noted that data on ionic state of palladium in such systems are not available at present and this problem requires a special study. However, we have attempted to make some conclusions on this matter in the present paper, as discussed below.

Before studying the palladium sorption recovery, we have obtained electron absorption spectra of freshly prepared palladium solutions in 1 M HNO_3 and at pH=2, presented in **Figure 1**. It should be noted that palladium sorption was carried out from freshly prepared solutions to minimize their "aging". It can be seen from Figure 1 that absorption maximum in spectrum 1 (Pd in 1 M HNO_3) is located at 390 nm and indicates the presence of complexes $[Pd(H_2O)(NO_3)_3]^-$ as a prevailing form [36-38]. However, the absorption maxima in spectra 2 and 3 (Pd in 0.01 M HNO_3 in the presence of 1 M KNO_3) are also located at 390 nm and show presence of the same $Pd(II)$ complexes in solution. Probably, the formation of anionic nitrate complexes of palla dium (II) is promoted by the high concentration of nitrate ions, despite the weak acidity of solution (pH=2). Later, during our experiments on $Pd(II)$ sorption, we have not observed any precipitation of metal specimens on a surface of resins, unlike authors [20]. It means that there was no hydrolysis in the investigated systems under chosen conditions (fresh prepared weak acidic solutions and presence of 1 M KNO_3). However, the precipitation effect was clearly observed when palladium sorption was carried out from solutions kept more than 8 h or from freshly prepared solutions with pH=4. This proves the formation of different hydroxocomplexes. Therefore, we can conclude from the absorption spectra that complexes $[Pd(H_2O)(NO_3)_3]^-$ prevail in contacting freshly prepared solutions under the chosen conditions.

3.2. Sorption Recovery of Palladium from Model Nitrate Solutions

The sorption properties of ion exchangers investigated to palladium (II) are presented in **Table 3**. It can be seen from these data that in general all the resins reveal high sorption ability, since they recover Pd on the level ~70

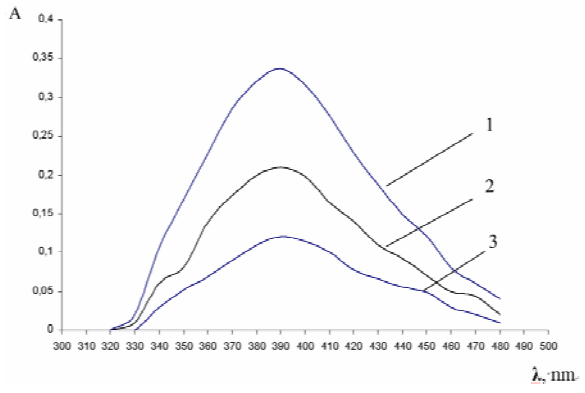

Figure 1. Absorption spectra of palladium (II) working solutions in 1 M HNO_3 (1) and in the system 0.01 M KNO_3 + 1.0 M KNO_3 (2,3), $C_0(Pd) = 2.0 \times 10^{-3}$ mol/L (1,2) and 1.0×10^{-3} mol/L (3).

% (ANKF-5) and more than 90 % (Purolite S 985). The studied sorbents can be arranged by their affinity grade to palladium in the following order: Purolite S 985 > Purolite A 530 > Purolite A 500 ~ AV-17-8 > AN-251 > ANKF-5.

It is interesting to note, that all ion exchangers except Purolite S 985 possess approximately equal affinity to Pd, despite of their different physical and chemical structure. The nature of functional groups of the ion exchangers investigated allows to form the following types of chemical bonds during their contact with noble metal ions [5,6,19,20]:

- ionic, i.e. ion – ion interaction, which takes place on strong basic anion exchangers;
- coordination, forming as a result of conservation of electron pair between ligand (electron-pair donor), which is the nitrogen atom of resin functional groups, and the metal (electron-pair acceptor); this bond takes place on weak basic anion exchangers.

The fact that amphoteric ion exchanger ANKF-5 recovers $Pd(II)$ ions from nitrate solutions on the same level (and even less) than anion exchanger AN-251 (both resins were synthesized on the basis of vinylpyridine), unambiguously points out to ionic state of $Pd(II)$ in contacting solution. If cationic hydroxocomplexes or hydrated ions $[Pd(H_2O)_4]^{2+}$ were present in this solution, the degree of palladium (II) recovery would probably be above 69% due to the activity of phosphorylic acid and pyridine nitrogen functional groups in weak acidic media.

Moreover, it is noteworthy that strong basic anion exchangers recover $Pd(II)$ to a greater extent (**Table 3**), although the additional complex formation of palladium ions with functional groups of quaternary ammonium base is impossible (unlike the weak basic anion exchangers). Therefore, we consider highly probable that anionic palladium complexes $[Pd(H_2O)(NO_3)_3]^-$ or $[Pd(NO_3)_4]^{2-}$ exist in the systems investigated in the presence of 1 M KNO_3.

Table 3. Sorption of palladium from nitrate model solutions on ion exchangers investigated Initial $Pd(II)$ concentration is $5.0 \cdot 10^{-4}$ mol/L, pH = 2.

Trade name	log *D*	*R*(%)	Trade name	log *D*	*R*(%)
Purolite A 500	2.79	86	AV-17-8	2.77	85
Purolite A 530	2.87	88	AN-251	2.54	78
Purolite S 985	3.23	94	ANKF-5	2.34	69

As for sorption recovery of palladium (II) on anion exchanger Purolite S 985, which reaches 94%, there is little doubt that this recovery proceeds according not only to anion exchange, but also to complexation process, taking into account the presence of polyamine groups in the structure of this sorbent.

3.3. FT-IR Study of Palladium Sorption

To study the palladium recovery from nitrate solutions in more detail, we have carried out IR-spectroscopic investigation. We have obtained IR-spectra of anion exchangers Purolite S 985, AV-17-8 and AN-251, the fragments of which are shown in **Figure 2.** IR-spectra of initial samples of these resins in chloride form are presented for comparison.

It can be seen from IR-spectra that appearance of intensive peaks in the range of 1400–1300 cm^{-1} (1384, 1352 and 1300 cm^{-1}) is observed for all the ion exchangers, independently of their basicity and structure of polymeric matrix. These peaks are assigned to vibrations of N–O bonds of nitrate ion: peak at 1384 cm^{-1} corresponds with stretching vibrations of free NO_3^- [20,39], whereas peaks at 1352 and 1300 cm^{-1} can be assigned to the N–O stretching vibrations in palladium complex [39]. It should be noted that the greatest intensity of these peaks is revealed in IR-spectrum of strong basic anion exchanger AV-17-8 (**Figure 2**, spectrum 5). It was mentioned above that the functional groups of this resin (quaternary ammonium base) cannot react with palladium through additional coordination. Therefore, it can be concluded that the anion exchange takes place in this case:

$$\overline{RCl} + [Pd(H_2O)(NO_3)_3]^- \Leftrightarrow \overline{R[Pd(H_2O)(NO_3)_3]} + Cl^- \quad (10)$$

Since the similar but less intensive peaks are revealed in IR-spectra of weak basic anion exchangers Purolite S 985 and AN-251 (**Figure 2**, spectra 1 and 3), it can be concluded that the reaction (10) is to some extent attributable to these resins too.

However, in case of $Pd(II)$ recovery on weak basic anion exchanger AN-251, the redistribution of the intensities in the range of 1700 – 1400 cm^{-1}, corresponding to symmetric and asymmetric stretching vibrations of pyridine ring, is observed in IR-spectrum of this resin (**Figure 2**, spectrum 3). The absorption bands at 1600, 1558, 1494 and 1417 cm^{-1} are assigned to C = C and C = N stretching in pyridine ring [20,39,40]. The reduction of peak intensity at 1510 cm^{-1} and depression of that one at 1492 cm^{-1} points out to the probable complexation between palladium and pyridine nitrogen [5,40].

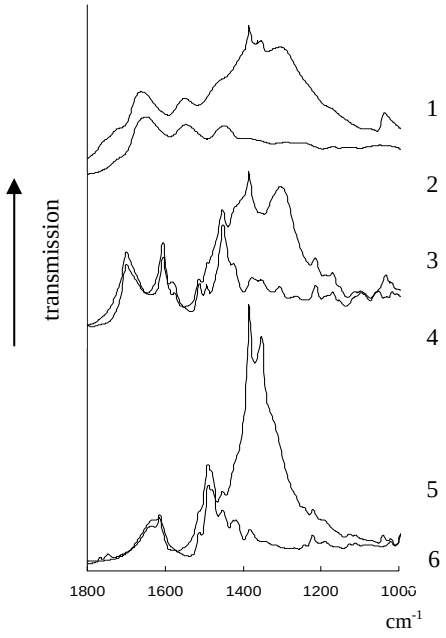

Figure 2. IR-spectra fragments of anion exchanger samples Purolite S 985 (1), AN-251 (3), AV-17-8 (5) saturated from nitrate solutions of palladium (II) $C_0(Pd) = 5.0 \times 10^{-4}$ mol/ L; $C_0(HNO_3) = 0.01$ mol/L; $C_0(KNO_3) = 1.0$ mol/L Spectra (2), (4) and (6) correspond respectively to initial samples of Purolite S 985, AN-251 and AV-17-8 in chloride form.

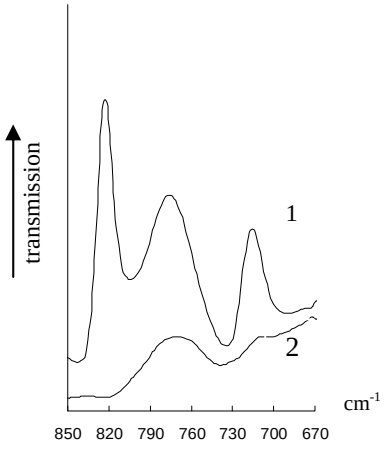

Figure 3. IR-spectra fragments of samples of anion exchanger Purolite S 985 saturated from nitrate palladium (II) solution (1) and of initial resin in chloride form (2) $C_0(Pd) = 5.0 \times 10^{-4}$ mol/L; $C_0(HNO_3) = 0.01$ mol/L; $C_0(KNO_3) = 1.0$ mol/L.

The IR-spectrum of weak basic anion exchanger Purolite S 985 saturated with palladium shows the greatest changes compared to the spectrum of its initial sample in chloride form (**Figure 2**, spectra 1 and 2). The peaks at 1384, 1352 and 1304 cm^{-1}, which correspond to nitrate ion and are characteristic for anion exchange in accordance with reaction (10), also appear in the spectrum 1. In the range of stretching vibrations of aminogroups (1550 – 1530 cm^{-1}), the reduction of peak intensities takes place, and in the range of 1450–1420 cm^{-1}, the peak disappears, corresponding to vibrations of methylene groups [5,40]. Such changes indicate that complexation processes in the sorbent's phase take place [5].

In case of Purolite S 985, special attention should be paid to the short-wavelength fragments of IR-spectra, shown in **Figure 3.** It contains an increase in peak intensity at 771 cm^{-1} and appearance of bands at 822 and 711 cm^{-1}. These changes correspond to deformation vibrations of $N \rightarrow Pd$ bond, which is characteristic for coordination compounds [5,40,41].

Therefore, it can be concluded that palladium sorption from nitrate weak acidic solutions on weak basic anion exchangers proceeds not only according to anion exchange mechanism (reaction (10)), but also is accompanied by coordination:

$$\overline{RN} + [PdL_n] \Leftrightarrow [\overline{RNPdL_{n-1}}] + L \qquad (11)$$

where $L = H_2O; NO_3^-; n = 2-4$.

3.4. Sorption Isotherm Studies

The isotherms of palladium sorption from nitrate solutions on anion exchangers Purolite S 985, A 500 and A 530 are represented in **Figure 4.** It is known [29,33] that the shape of these curves is an evidence of sorption selectivity. It can be seen from **Figure 4** that all the isotherms are convex curves and they are classified to Langmuir isotherms, which are described as follows:

$$EC = EC_\infty \cdot \frac{\overline{K_{eq}} \cdot C_{eq}}{1 + \overline{K_{eq}} \cdot C_{eq}} \qquad (12)$$

where EC_∞ is the maximal equilibrium exchange capacity of the resin to palladium, mmol/g; K_{eq} is the apparent constant of ion exchange equilibrium, L/mmol.

By transforming the **Eq. (12)** to the linear form, we calculated ion exchange equilibrium constants and determination coefficients (r^2), which are presented in **Table 4.** It can be seen from these data that coefficients r^2 are close to 1. This fact supports our hypothesis about Langmuir-type isotherms for palladium sorption.

3.5. Kinetics Studies

The successful application of ion exchangers in industrial conditions requires their good kinetic properties. That is why the research on kinetics of $\overline{Pd(II)}$ sorption on Purolite ion exchangers in the investigated systems is both of theoretical and practical interest. The

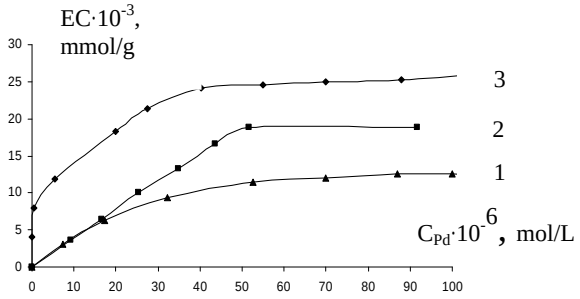

Figure 4. Isotherms of palladium sorption on anion exchangers Purolite A 530 (1), A 500 (2) and S 985 (3) $C_0(HNO_3) = 0.01$ mol/L; $C_0(KNO_3) = 1.0$ mol/L.

Table 4. Apparent constants of ion exchange equilibrium (K_{eq}) and determination coefficients (r^2) during recovery of palladium (II) from nitrate model solutions.

Trade name	$\overline{K_{eq}}$	r^2
Purolite A 500	135	0.894
Purolite A 530	34.4	0.991
Purolite S 985	588	0.975

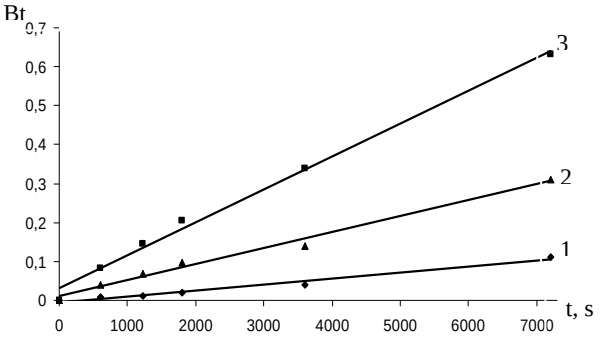

Figure 5. Kinetic dependencies of ***Bt*** function on time t for anion exchangers Purolite A 530 (1), S 985 (2) and A 500 (3).

Table 5. Kinetic parameters of palladium (II) sorption from nitrate model solutions $C_0(Pd) = 5.0 \times 10^{-4}$ mol/L; $C_0(HNO_3) = 0.01$ mol/L; $C_0(KNO_3) = 1.0$ mol/L.

Trade name	$\overline{\upsilon} \cdot 10^6$ (mmol/g·s)	$\overline{D_s} \cdot 10^8$ (cm^2/s)	$t_{1/2}$ (s)
Purolite A 500	11.70	8.26	1558
Purolite A 530	2.06	0.58	23164
Purolite S 985	9.26	5.94	2390

calculated main kinetic parameters are summarized in **Table 5** and **Figure 5** contains the dependencies $Bt = f(t)$.

It can be seen from **Figure 5** that dependencies $Bt = f(t)$ are the straight lines for all the resins Purolite investigated and comply with criterion of gel kinetics, i.e. the whole sorption process is controlled by interdiffusion of the ions exchanged in a resin grain [29,30,33]. As for the main kinetic parameters, it should be noted that average rate of ion exchange process is higher on strong basic anion exchanger Purolite A 500 (**Table 5**). Consequently, the value of average diffusion coefficient for this resin exceeds such values for the other sorbents and the half-exchange time is lesser. A comparison of kinetic process between anion exchangers Purolite S 985 and A 500 shows that such behavior of these sorbents is in good consistence with our above-mentioned assumptions about sorption mechanism. Since the palladium sorption on Purolite A 500 is not complicated by additional complexation (in contrast to Purolite S 985), the rate of this process is higher and diffusion coefficient values are also bigger, whereas the half-exchange times are lesser for this resin. However, it is interesting to note that the strong basic anion exchanger Purolite A 530, which is not practically distinguished from A 500 in its sorption properties (**Table 3**), compares much unfavorably with A 500 in its kinetic properties (**Table 5**). The average rate of ion exchange process on Purolite A 530 is about 5 times lower than on Purolite A 500. Also the average diffusion coefficient values for A 530 are by one order smaller and the half-exchange time is by one order greater (**Table 5**). Such behavior of anion exchanger Purolite A 530 in comparison with also strong basic resin A 500 can be probably explained by its exchange capacity, which is less by half than this value for A 500, and by its lesser swelling as well (**Table 1**). Moreover, it can be assumed that the sorbed complex ions of palladium (II), which possess a square spatial configuration [42], have not enough time to reach the active centers of the sorbent A 530, where the anion exchange occurs, because of its small exchange capacity (there are few available exchange centers on a resin surface). Certainly this phenomenon requires a special study, but from the practical point of view the anion exchanger Purolite A 500 is preferable than sorbent Purolite A 530 for recovery of palladium (II) from nitrate solutions.

3.6. Sorption of Palladium from Nitrate Solutions of Spent Catalysts

Further we have studied the sorption recovery of palladium (II) from solutions of spent catalysts on some anion exchangers chosen on the basis of their good sorption and kinetic properties. The results are summarized in **Table 6.**

It can be seen from these data that the anion exchangers in general possess good sorption ability to $Pd(II)$ ions, but this characteristic is slightly lower in compari-

son with the data obtained for model solutions, excluding anion exchanger AV-17-8 (**Table 3**). Partly the decrease in $Pd(II)$ recovery from real solutions can be explained by complex composition of initial solution of spent catalyst (**Table 2**), where a number of ions produce a competing effect on palladium sorption process.

In order to determine the form of palladium in contacting solution of spent catalyst as well as in the phase of strong basic anion exchanger, we have obtained the diffuse reflectance spectra presented in **Figure 6**. It can be seen from these data that the maximum in diffuse reflectance spectra is located at 410 nm. It corresponds with the maximum in absorption spectrum at 390 nm (**Figure 1**), since the bathochromic shift of maximum in diffuse reflectance spectra is observed during sorption concentration of noble metal ions in view of matrix effect of solid phase [43,44]. Therefore, the prevailing form of $Pd(II)$ existence in nitrate weak acidic solutions of spent catalysts is its complex $[Pd(H_2O)(NO_3)_3]^-$

It is known [2-5,15] that the desorption of noble metals from highly selective ion exchangers is hardly achievable process because of strong retention of adsorbed metal ions by functional groups of resins. Due to that, for the successful regeneration of these sorbents it is necessary to use the elution agents which form more stable complexes with the recovered metal ions than the complexes of these metals existing in the resin phase. From this point of view, the acidic or basic thiourea solutions are widely applied as eluting agent [1,15,19,22-24,27]. We have also used in the present work the thiourea solutions for palladium desorption after its sorption recovery. The results are shown in **Table 7**. It can be seen from the presented data that the palladium (II) elution degrees after its recovery from model solutions reach the level of 78-82% – the result which is considered quite satisfactory. However, the palladium desorption after its recovery from solutions of spent catalysts proceeds on the level of 22–25%. When carrying out this process, we have changed thiourea concentration and used its solutions in HNO_3 or $NaOH$, but the best result we could reach was ~ 25% by palladium elution with 1 M thiourea solution in 1 M $NaOH$. It should be noted that the recovery of noble metals from industrial solutions after their sorption on highly selective ion exchangers is often carried out by burning of such resins, since the value of noble metals exceeds the costs of ion exchange materials, even selective ones [2,4,24,45]. Therefore, it is necessary to continue the research for improving the palladium recovery after its sorption on selective ion exchangers from solutions of spent cata-lysts.

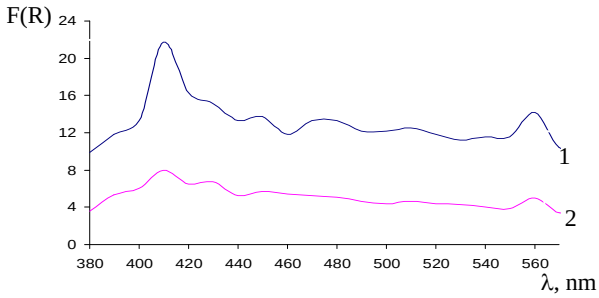

Figure 6. Diffuse reflectance spectra of anion exchangers' samples AV-17-8 (1) and Purolite A 500 (2) saturated with palladium (II) from nitrate solutions of spent catalysts. $C_0(Pd) = 5.0 \times 10^{-4}$ mol/L; $C_0(HNO_3) = 0.01$ mol/L; $C_0(KNO_3) = 1.0$ mol/L F(R) – diffuse reflectance coefficient.

Table 6. Sorption recovery of palladium (II) from nitrate solutions of spent catalysts $C_0(Pd) = 5.0 \times 10^{-4}$ mol/L; $C_0(HNO_3) = 0.01$ mol/L; $C_0(KNO_3) = 1.0$ mol/L.

Trade name	log D	R(%)
Purolite A 500	2.31	65
Purolite S 985	2.86	88
AV-17-8	2.72	84

Table 7. Elution of palladium from anion exchangers investigated by thiourea solution (1.0 mol/L) in 0.01 M HNO_3 after palladium sorption from nitrate weak acidic model solutions.

Trade name	Desorption degree (%)
Purolite S 985	78
Purolite A 500	82

4. CONCLUSIONS

Sorption recovery of palladium (II) from nitrate weak acidic model solutions and solutions of spent catalysts on some ion exchangers with different physical and chemical structure was investigated. Based on electron absorption spectra, it was determined that complexes $[Pd(H_2O)(NO_3)_3]^-$ prevail in contacting solutions. It was shown that ion exchangers investigated possess good sorption and kinetic properties.

The mechanism of palladium sorption recovery on strong and weak basic anion exchangers from nitrate weak acidic solution was outlined by means of FT-IR-spectroscopy. It was shown that strong basic anion exchangers sorb palladium according to anion exchange, whereas weak basic resins recover $Pd(II)$

complexes not only by anion exchange, but also by means of additional coordination with nitrogen atoms of functional groups.

The palladium (II) desorption after its recovery on selective ion exchangers from model solutions and solutions of spent catalysts was carried out using thiourea solutions. It was shown that the degree of palladium elution by 1 M thiourea solution in 0.01 M HNO_3 after its sorption from model solutions is on the level of 78 – 82 %, whereas this value does not exceed 25% after $Pd(II)$ sorption from solutions of spent catalysts. The improvement of this process should be a subject for further research.

Based on results of present investigation, the anion exchangers AV-17-8 as well as Purolite S 985 and A 500 can be recommended for selective recovery of palladium (II) from nitrate weak acidic solutions.

5. ACKNOWLEDGEMENT

The authors would like to express profound gratitude to the team of Moscow office of Purolite International Ltd, who kindly provided us with ion exchanger samples.

REFERENCES

[1] R. Pfrepper, (1988) Möglichkeiten Der Wiedergewinnung Von Pd Aus Sekundären Rohstoffquellen. ZFI-Mitteilungen. Akademie-Verlag, Berlin, 3-292.

[2] I. F. Khudyakov, A. P. Doroshkevich, S. V. Karelov, (1990) Metallurgy of the secondary non-ferrous heavy metals. Nauka, Moscow, 15-25.

[3] M. A. Meretukov and A. M. Orlov, (1990) Metallurgy of noble metals. Metallurgiya, Moscow, 27-30.

[4] A. G. Kholmogorov, (1986) Ion exchange in hydrometallurgical processing of palladium-containing spent catalysts. Sibir, Krasnoyarsk, 150-151.

[5] K. M. Saldadze and V. D. Kopylova-Valova, (1980) Complex-forming ion exchangers. Nauka, Moscow, 3- 336.

[6] S. A. Simanova, A. S. Tevlina, and I. S. Bazhanova, (1994) Formation of palladium complexes during sorption on high permeable sorbents with heterocyclic nitrogen atoms. J. Inorg. Chem., Moscow, **39(1)**, 121-126.

[7] I. A. Kovalev, G. I. Tsyzin, and A. A. Formanovskiy, (1995) Concentration of rhodium, palladium and platinum on sorbent with ethylenetriamine groups. J. Inorg. Chem., Moscow, **40(5)**, 828-833.

[8] I. A. Tarkovskaya, L. P. Tikhonova, and N. V. Kulik, (1997) Sorption of platinum group metals from aqueous solutions on inorganic and synthetic ion exchange materials. Khimiya I Tekhnologiya Vody, **19(3)**, 227-239.

[9] A. G. Kholmogorov, O. N. Kononova, S. V. Kachin, and S. V. Razvodovskaya, (1998) Sorption of palladium from chloride solutions on anion exchangers with macro-reticular and porous structure. J. Phys. Chem., Moscow, **72(2)**, 318-321.

[10] O. P. Shvoeva, V. P. Dedkova, and S. B. Savvin, (2004) Effect of masking compounds on color reactions of dithizone with Pd (II), Hg (II) and Ag (I) after sorption from chloride solutions on fibrous anion exchanger. J. Anal. Chem., Moscow, **59(7)**, 704-709.

[11] V. P. Dedkova, O. P. Shvoeva, and S. B. Savvin, (2005) Test-method for determination of palladium in chloride solutions in solid phase of fibrous ion exchanger. J. Anal. Chem., Moscow, **60(1)**, 85-89.

[12] Z. Hubicki and M. Leszczynska, (2005) Sorption of palladium (II) chloride complexes on weakly, intermediate and strongly basic anion exchangers. Desalination, **175**, 227-236.

[13] Z. Hubicki and A. Wolowicz, (2009) Adsorption of palladium (II) from chloride solutions on Amberlyst A 29 and Amberlyst A 21 resins. Hydrometallurgy, **96**, 159-165.

[14] Z. Hubicki and A. Wolowicz, (2009) A comparative study of chelating and cationic ion exchange resins for removal of palladium (II) complexes from acidic chloride media. J. Hazard. Mater., **164**, 1414-1419.

[15] V. V. Milyutin, S. V. Peskishev, and V. M. Gelis, (1994) Sorption of palladium, ruthenium and rhodium from nitric acidic solutions on different sorbents. Radiokhimiya, **36(1)**, 25-28.

[16] G. R. Anpilogova and E. V. Kondratieva, (1996) Study of palladium (II) sorption on polyethylene-monosulfide from nitric acidic solutions. J. Inorg. Chem., Moscow **41(3)**, 447-452.

[17] V. I. Skorokhodov, O. Y. Goryaeva, B. K. Radionov, (2004) Choice of optimal structure of ion exchangers for palladium sorption from nitric acidic solutions. Tsvennaya Metallurgiya, **1**, 31-33.

[18] Z. Hubicki, M. Leszczynska, B. Lodyga, and and A. Lodyga, (2007) Recovery of palladium (II) from chloride and chloride-nitrate solutions using ion exchange resins with S-donor atoms. Desalination, **207**, 80-86.

[19] K. A. Venkatesan, B. R. Selvan, M. P. Antony, T. G. Srinivasan, and P. R. V. Rao, (2007) Extraction of palladium (II) from nitric acid medium by imidazolium nitrate immobilized resin. Hydrometallurgy, **86**, 221-229.

[20] R. Kumaresan, K. N. Sabharval, T. G. Srinivasan, P. R. V. Rao, and G. Dhekane, (2008) Studies on the sorption of palladium using cross-linked poly(4-vinylpyridine- divinylbenzene) resins in nitric acid medium. Solv. Extr. Ion Exchange, **26**, 643-671.

[21] A. V. Belyaev, (2003) Chemical-technological problems of platinum group metals during processing of exhausted nuclear fuel. Zhurnal Strukturnoy Khimii, **44(1)**, 39-47.

[22] O. N. Kononova, A. G. Kholmogorov, and E. V. Mikhlina, (1998) Palladium sorption on vinylpyridine ion exchangers from chloride solutions obtained from spent catalysts. Hydrometallurgy, **48**, 65-72.

[23] O. N. Kononova, N. G. Goryaeva, N. B. Dostovalova, S. V. Kachin, and A. G. Kholmogorov, (2007) Recovery of palladium from acidic solutions using carbon adsorbents. Khimiya Tverdogo Topliva. **4**, 71-75.

[24] O. N. Kononova, A. N. Lukianov, M. V. Derevyashkin, A. G. Kholmogorov, S. V. Kachin, and N. G. Goryaeva, (2008) Sorption of palladium on carbon adsorbents from nitric acid solutions. J. Porous Mater. **15**, 61-66.

[25] O. N. Kononova, K. A. Shatnykh, K. V. Prikhodiko, D. M. Kashirin, and A. G. Kholmogorov, (2009) Sorption of gold (I) and silver (I) from thiosulfate solutions on anion

exchangers. Tsvetnye Metally, **1**, 40-43.
[26] F. E. Beamish, (1966) The analytical chemistry of the noble metals. Pergamon Press, Oxford, London, Edinburgh, New York, Toronto, Paris, Frankfurt, 41-45.
[27] S. I. Ginzburg, N. A. Ezerskaya, I. V. Prokofieva, N. V. Fedorenko, Y. I. Shlenskaya, and N. K. Belskiy, (1972) Analytical chemistry of platinum group metals. Nauka, Moscow, 165-166.
[28] F. Umland, A. Janssen, D. Thierig, and G. Wünsch, (1971) Theorie und praktische Anwendung von Komplexbildnern. Akademische Verlagsgesellschaft, Frankfurt am Main, 364-365.
[29] F. Helfferich, (1962) Ion exchange. McGraw-Hill, New York, 335-360.
[30] F. Helfferich and J. A. Marinsky, (1966) Ion exchange kinetics. (ed.) Ion exchange. A series of advances. McGraw-Hill, Buffalo, New York, 281-331.
[31] D. C. Harris, (1996) Quantitative chemical analysis. Freeman and Company, New York, 374-376.
[32] J. H. Pollard, (1977) A handbook of numerical and statistical techniques. Cambridge University Press, Cambridge, 342-345.
[33] Y. A. Kokotov, (1990) Ion exchangers and ion exchange. Khimiya, Leningrad, 47-52.
[34] Y. A. Zolotov, G. M. Varshal, and V. M. Ivanov, (2003) Analytical chemistry of platinum group metals. Editorial URSS, Moscow, 16-88.
[35] S. E. Livingstone, (1967) The chemistry of ruthenium, rhodium, palladium, osmium, iridium and platinum. Pergamon Press, Oxford, New York, Toronto, Sydney, Paris, Braunschweig, 178-211.
[36] R. A. Shoytsov, (1972) Spectrophotometrical investigation of palladium (2+) state in aqueous solutions. State University, Moscow, Moscow, PhD-thesis.
[37] V. S. Shmidt, N. A. Shorokhov, A. A. Vashman, and V. E. Samsonov, (1982) Study of complex $Pd(NO_3)_2 \cdot (H_2O)_2$. J. Inorg. Chem., Moscow, **27(5)**, 1254-1256.
[38] P. I. Antyukhin, (1993) About correlation between solubility constants of metal hydroxides and formation constants of their neutral hydroxocomplexes. Sibirskiy Khimicheskiy Zhurnal, **1**, 21-25.
[39] L. Bellami, (1963) Infrared spectra of complex molecules. Inostrannaya Literatura, Moscow, 383-590.
[40] V. A. Uglyanskaya, G. A. Chikin, V. F. Selemenev, and G. A. Zavialova, (1989) Infrared spectroscopy of ion exchange materials. Izdatelstvo VGU, Voronezh, 150-207.
[41] K. Nakamoto, (1986) Infrared and raman spectra of inorganic and coordination compounds. Wiley, New York, 360-536.
[42] F. A. Cotton and G. Wilkinson, (1969) Advanced inorganic chemistry. A Comprehensive Text, Mir, Moscow, 460-469.
[43] P. Kubelka, and F. Munk, (1931) Ein Beitrag Zur Optik Der Farbanstriche. Z. Techn. Phys., **12**, 593 -601.
[44] G. D. Brykina, D. Y. Marchenko, and O. A. Shpigun, (1995) Solid-phase spectrophotometry. J. Anal. Chem., Moscow, **50(5)**, 484-491.
[45] V. V. Barchenkov, (1982) Sorption technology of recovery of gold and silver from ores. Nauka, Moscow, 155-286.

Vol.1, No.3, 176-180 (2009)
doi:10.4236/ns.2009.13022

Natural Science

Fabrication of two-dimensional periodic TiO_2 pillar arrays by multi-beam laser interference lithography

Hiroyo Segawa[1], Hiroaki Misawa[2]

[1]Exploratory Nanomaterials Research Laboratory, National Institute for Materials Science, Tsukuba, Japan
[2]Research Institute for Electronic Science, Hokkaido University, Sapporo, Japan

Received 19 August 2009; revised 21 September 2009; accepted 22 September 2009.

ABSTRACT

Two-dimensional (2D) periodic TiO_2 pillar arrays, applicable to photonic crystals and microchannels, were fabricated by direct patterning of a TiO_2-organic hybrid material by multi-beam laser interference lithography and calcination of hybrid patterns. 2D periodic pillars of a TiO_2–organic hybrid material were prepared by irradiation with the interference pattern of femtosecond laser beams and removal of the non-irradiated portions. Two types of periodic pillar arrays, standing pillars and top-gathering pillars (four pillars gathered at the top), were obtained, depending on laser irradiation conditions. After calcination of TiO_2–organic hybrid pillars, TiO_2 pillar arrays were obtained without collapse.

Keywords: Lithography, Capillary Force, Assembly

1. INTRODUCTION

Two-dimensional (2D) periodic arrays of dielectric materials with submicrometer to micrometer repetitions have great potential in various applications, such as diffraction gratings [1], photonic crystals (PCs) [2,3], and molecular separation in a microchannel [4,5]. Most of these arrays are fabricated by lithography, in which dielectric materials are coated with photoresists, the photoresist patterns are fabricated by beams such as electron beams, lasers, and beams of UV light, and the patterns of the dielectric material are chemically etched in the area not covered by the photoresist. The patterns of the dielectric materials do not feature a high aspect ratio (pattern height to pitch), and complex patterns, e.g.,three-dimensional (3D) patterns, cannot be obtained easily, because dielectric materials are generally stable for chemical etchants.

However, patterns such as pillars [6,7], waveguides [8, 9,10], and diffraction gratings [11], can be fabricated in organic–inorganic hybrid materials by direct lithography. Organic–inorganic hybrid materials prepared by the sol–gel method are composed of inorganic networks modified with photosensitive organic molecules such as unsaturated hydrocarbons or β-diketonato ligands. When the hybrid films are exposed to UV light or a laser, photosensitive organic groups react, and the solubility of the exposed parts in alcohol decreases. Removing the unexposed portions produces the patterns of hybrid materials.

Hybrid materials are generally more flexible than inorganic materials due to the characteristics of the organic groups; therefore, they have been used to fabricate many types of thick films with thickness greater than 1 μm. Most thick films are prepared by the sol–gel method, using organosiloxanes, in which one or two alkoxyl groups of the silicone alkoxide change to functional organic groups. However, it is known to be difficult to fabricate thick films without using organosiloxane.

In our previous work, different types of photosensitive TiO_2–organic hybrid films were prepared by the sol–gel method [12,13,14]. TiO_2 hybrid films were prepared from a Ti alkoxide, and modified with a β-diketone and/or an unsaturated hydrocarbon. Two types of TiO_2 hybrid dot arrays, with a pitch spacing of 1.3 μm and a height of about 250–300 nm, were directly fabricated by multi-beam laser interference (MLI) lithography. In this method, photosensitive materials are exposed to the interference light pattern and developed in an appropriate solvent [13,14]. One type was fabricated by multi-photon absorption (MPA) of a femtosecond laser at 800 nm, while another was fabricated by a nanosecond laser at 351 nm. Hybrid films with a thickness of about 1 μm were used for the lithography; however, the light for photopolymerization was absorbed in the film, and moreover, photopolymerization did not occur over the entire film. Both types of TiO_2–organic hybrid dot arrays were calcined, and TiO_2 arrays were fabricated without collapse or exfoliation; however, patterns with a high aspect ratio could not be produced.

MPA is a well-known method of fabricating complex patterns by photopolymerization of organic compounds [15,16]. If MPA was used for producing patterns in

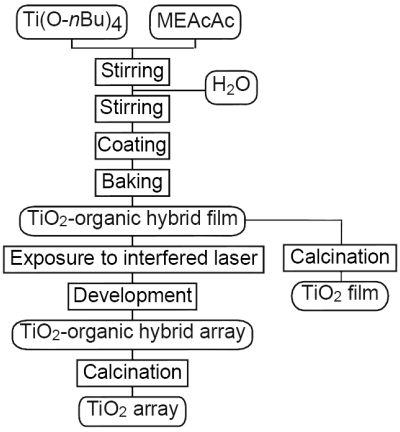

Figure 1. Flowchart of experimental procedure.

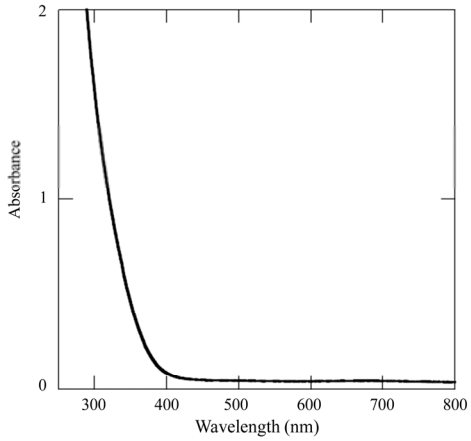

Figure 2. UV-VIS spectrum of TiO_2–organic hybrid film.

thick organic-inorganic hybrid films by lithography, fabrication of 3D patterns with a high aspect ratio would be possible. The hybrid materials could be easily changed to ceramics by calcination, resulting in complex ceramic patterns.

In this study, 2D periodic pillar arrays of TiO_2 with a high aspect ratio were fabricated directly from TiO_2–organic hybrid films with a thickness greater than 1 μm, using the MLI technique and by calcination of the organic groups.

2. EXPERIMENTAL PROCEDURE

A flowchart of the experimental procedure is shown in **Figure 1**. A TiO_2–organic hybrid gel film with a thickness greater than 1 μm was prepared by the sol–gel method [14]. Titanium tetra-n-butoxide (Ti(O-*n*Bu)$_4$, Kishida Chemical Co.) was reacted with 2-(methacryloyloxy)ethyl acetoacetate (MEAcAc, Acros Organics); the molar ratio between Ti(O-*n*Bu)$_4$ and MEAcAc was 1:1. After stirring the solution for 15 min at room temperature, H_2O was poured into the solution; the molar ratio between H_2O and Ti(O-*n*Bu)$_4$ was 2:1. The solution was stirred for 3 hat room temperature. The sol was then spin-coated at 1000 rpm for 20 sec on glass substrates. The hybrid film was baked at 80°C for 10 min.

The film was then exposed to the interference pattern of femtosecond laser pulses. The optical setup has been described previously [17]. In brief, a diffractive beam splitter (G1023A, MEMS Optical Inc.) divided the input laser beam into four beams, which were then collected on the film using two lenses. The femtosecond pulses were produced by a Ti:sapphire regenerative amplifier (800-nm wavelength, 150-fs pulse duration, 1-kHz repetition rate). The single-pulse energy (sum of all beams) was 20–35 μJ. After laser irradiation for 1–10 min, the films were developed in 2-ethoxyethanol for 1 min to remove the non-irradiated portions. After dryingthe 2-ethoxyethanol, the TiO_2–organic hybrid arrays remained on the substrates. The hybrid arrays were calcined at 450 °C for 1 h, finally producing TiO_2 arrays. The periodic arrays before and after calcination were imaged by ascanning electron microscope (SEM; JSM-6700FT, JEOL).

A UV-VIS spectrum of the prepared hybrid film was measured by a spectrometer (JASCO, V-570). The hybrid film was calcined at 120–750 °C for 1h, and refractive indices of the film after calcination were measured at 632.8 nm with a Metricon 2010 prism coupler.

3. RESULTS & DISCUSSIONS

Figure 2 shows the UV-VIS spectrum of the TiO_2–organic hybrid film. In the spectrum, the increase in absorption around 400 nm might be assigned to the diketonate chelate between MEAcAc and Ti(OBu)$_4$ [14]. As seen in **Figure 2**, the laser light at 800 nm was not absorbed by the hybrid film.

Typical SEM images of the TiO_2–organic hybrid pillar arrays are shown in **Figure 3**. In **Figure 3a, 3b**, and **3c**, the pillar arrays were obtained by irradiation with a 30-μJ single-pulse for 100, 140, and 300 sec, respectively. In the pillar arrays of **Figure 3a**, all pillars are gathered at the top, and top-gathering units composed of four (2 × 2) pillars are arranged periodically. In **Figure 3b**, all pillars are standing vertically on the substrate, and are arranged tetragonal, which corresponds to the light distribution. In **Figure 3c**, many pillars are gathered without any empty space between pillars, and have adhered to each other. The pillar diameter increased with increased laser irradiation time. When the laser irradiation time increases, the photopolymerization of the hybrid film proceeds, leaving a wider area on the substrate after development, resulting in thicker pillars. In **Figure 3**, the pillar arrays were fabricated on 1.4-μm thick films, and the height of the pillars was 1.4 μm. The height of pillars were improved from previous ones [14] and aspect ratio of the pillars became high. This represents that

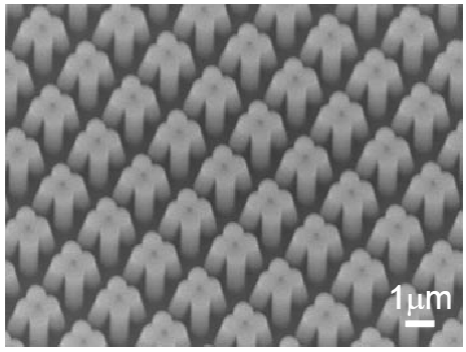

(a)

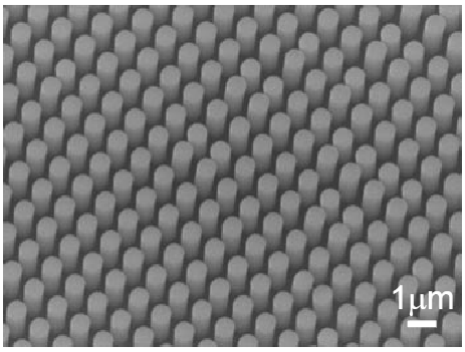

(b)

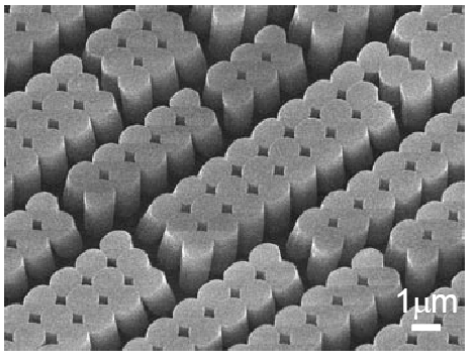

(c)

Figure 3. SEM images of typical TiO_2–organic hybrid pillar arrays fabricated by 30-μJ irradiation for (a) 100, (b) 140, and (c) 300 sec.

the photopolymerizaion occurred in the whole film by the two-photon absorption of the laser light, which were not absorbed by the hybrid film.

Figure 3 shows that the pillars gathered at the top when their diameter was either too small or too large. The gathering phenomenon is explained by the balance between the cohesive and restoring forces, which works on the pillars during the drying of 2-ethoxyethanol. When 2-ethoxyethanol dries after the development, a cohesive force is induced by the capillary force among the pillars, causing the pillars to approach each other. For periodic pillar arrays, in which pillars of height l_z and radius R are arranged with distance l_y between pillar centers, the capillary force P is expressed as [18]

$$p = \frac{2\pi R l_z \sigma \cos\theta}{(1 + D/d)} \quad (1)$$

where σ is the surface tension, θ is the contact angle of the developer, and $D = l_y - 2R$ is the gap size. The projection distance d (along the capillary force) corresponds to the distance between the liquid–pillar contact point and the pillar edge [$d \to 0$ at non-wetting condition ($\theta = \pi/2$), and $d \to R$ at full wetting condition ($\theta = 0$)]. When the pillars bend due to capillary force, the restoring force, F, operates. Assuming that the pillars are regarded as an elastic beam supported at one end, the force F can be expressed as [19]

$$F = \frac{2R^4}{l_z^4} E\delta \quad (2)$$

where the E is the Young's modulus of the pillars, and is the sway value.

When the pillar is excessively thin, the gap D is larger and R is smaller than those of the thick pillars. Thus, the capillary force is smaller, according to **Eq.1**. From **Eq.2**, the restoring power is also smaller than that for thick pillars. However, a comparison between **Eqs.1** and **2** indicates that the diameter might affect the restoring force more than the capillary force. Therefore, the pillars gather at the top, as shown in **Figure 3(a)**. On the other hand, the capillary force between thick pillars (from **Eq. 1**) is larger than that between thin pillars because of the smaller gap size, D, and larger radius, R. Thus, from **Eq. 2**, the restoring force increases. As shown in **Figure 3(c)**, the neighboring pillars seem to adhere to each other. This means that the laser irradiation time was too long to photopolymerize a wide area similar to the area filled with pillars; therefore, the pillars gather and adhere to each other.

Although the films had many cracks after calcination, the refractive index of the film is plotted as a function of calcination temperature in **Figure 4**. The refractive index of the film increases with an increase in calcination temperature. The highest value achieved by calcination

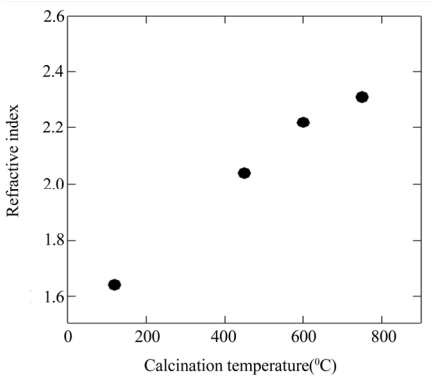

Figure 4. Refractive indices of film for different calcination temperatures.

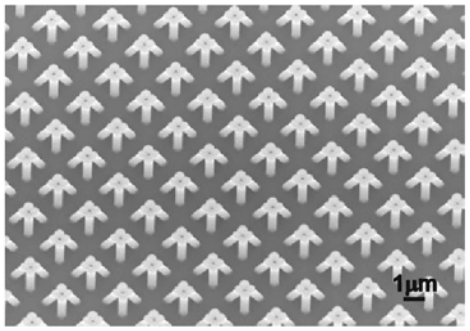

(a)

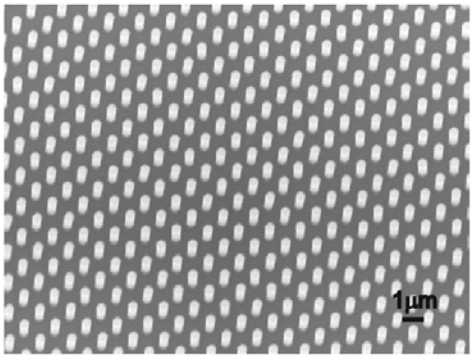

(b)

Figure 5. SEM images of TiO2 pillar arrays fabricated by irradiation at 30 μJ for (a) 100 and (b) 140 sec followed by calcination at 450 °C for 1h.

at 750 °C was 2.31-smaller than the refractive index of anatase (2.55) [20]. Since the films had cracks, the refractive indices might be assumed to be smaller than those of a dense TiO_2 film.

To investigate changes in morphology, SEM images of the periodic pillars calcined at 450 °C are shown in **Figure 5**. **Figure 5(a)** and **(b)** were calcined at 450 °C the TiO_2–organic hybrid arrays which were shown in **Figure 3(a)** and **(b)**, respectively.The top-gathering pillars in **Figure 5(a)** were calcined, after which they retained the top-gathering structure, although the size became smaller. **Figure 5(b)** shows that the pillar size decreased after calcination. The several kinds of organic compounds were remained in the hybrid pillars before calcination, and those were decomposed by the heating and removed. Thus, the pillars shrunk after the calcination. As shown in **Figure 5**, the pillars did not collapse. Generally, films without patterns were restricted by the substrate and subjected to large stresses during the calcination, resulting in the many cracks. In this case, the pillars were small not to restrict by the substrate and could shrink without stress during calcination.

XRD patterns of the periodic array after calcination at 450 °C are shown in **Figure 6**. All the peaks can be assigned to anatase. **Figure 4** shows that the refractive index of the film calcined at 450 °C was 2.04, which is smaller than the reported value of anatase (2.55) [20]. However, the refractive index of the pillars might be

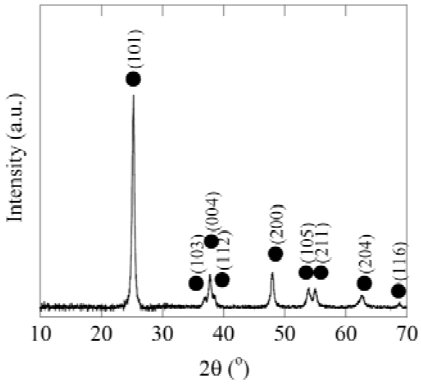

Figure 6. XRD pattern of TiO_2 pillar arrays.

larger than that of the film, since the pillars appear dense.

These results indicate that patterning of photosensitive hybrid materials by lithography and calcination of hybrid materials are excellent methods of creating fine patterns with high aspect ratios in ceramics. Generally, the preparation of the photosensitive hybrid films with chelate compounds are useful to obtain patterns of such as ZrO_2 [21] and $PbZr_{0.52}Ti_{0.48}O_3$ (PZT) [22]. If thick organic-inorganic hybrid films are obtained, complex ceramic patterns can be easily produced by direct lithography of hybrid films and calcination of hybrid patterns.

4. CONCLUSIONS

We produced TiO2 pillar arrays with a high aspect ratio by MLI lithography and calcination. Pillars with a high aspect ratio were successfully fabricated by the multiphoton absorption of a femtosecond laser. TiO_2–organic hybrid pillar arrays were fabricated by MLI, and two types of patterns, a periodic pillar array and a top-gathering pillar array, were obtained, depending on the laser irradiation time. The laser irradiation time affected the balance between the cohesive and restoring forces during the drying of the developer in lithography. After calcination of the hybrid patterns, TiO_2 patterns were obtained without collapse. This suggests that direct lithography of organic–inorganic hybrid materials and calcination can be applied to fabrication of complex patterns in ceramics.

REFERENCES

[1] H. P. Herzig (1997), Micro-optics. Taylor & Francis, Ltd., London, UK.

[2] J. D. Joannapoulos, R. D. Meade, and J. N. Winn, Photonic crystals.Princeton University Press, Princeton, NJ, 1995.

[3] E. Yablonovitch, (1993) Photonic band-gap structures. J.

Opt. Soc. Am. B, 10283-295.

[4] W. D. Volkmuth and R. H. Austin, (1992) DNA electrophoresis in microlithographic arrays. Nature, **358**, 600-602.

[5] N. Kaji, Y. Tezuka, Y. Takamura, M. Ueda, T. Nishimoto, H. Nakanishi, Y. Horiike, and Y. Baba, (2004) Separation of long DNA molecules by quartz nanopillar chips under a direct current electric field. Anal. Chem., **76**, 15-22.

[6] H. Segawa, Y. Yamazaki, T. Yano, and S. Shibata, (2006) Top-gathering periodic array derived from self-organization of hybrid organic-inorganic pillars. Jpn. J. Ceram. Soc., **114**, 120-124.

[7] H. Segawa, S. Yamaguchi, Y. Yamazaki, T. Yano, S. Shibata, and H. Misawa, (2006) Top-gathering pillar array of hybrid organic-inorganic material by means of self-organization. Appl. Phys. A, **83**, 447-451.

[8] H. Krug, F. Tiefence, P. W. Oliveira, and H. Schmidt, (1992) Organic-inorganic composite materials: Optical properties of laser-patterned and protective-coated waveguides. SPIE, **1758**, 448-455.

[9] H. Schmidt, J. Krug, R. Kasemann, and F. Tiefensee, (1991) Devel opment of optical wave guides by sol-gel techniques for laser patterning. SPIE, **1590**, 36-43.

[10] S. I. Najafi, T. Touam, R. Sara, M. P. Andrews, and M. A. Fardad, (1998) Sol-gel glass waveguide and grating on silicon. J. Lightwave Tech., **16**, 1640-1646.

[11] H. J. Jiang, X. C. Yuan, Y. Zhou, Y. C. Chan, and Y. L. Lam, (2000) Single-step fabrication of diffraction gratings on hybrid sol-gel glass using holographic interference lithography. Opt. Commun., **185** 19-24.

[12] H. Segawa, S. Adachi, Y. Arai, and K. Yoshida, (2003) Fine patterning of hybrid titania films by ultraviolet irradiation. J. Am. Ceram. Soc., **86**, 761-64.

[13] H. Segawa, H. Misawa, and S. Matsuo, (2004) Fabrication of fine-pitch TiO_2-organic hybrid dot arrays using multiphoton absorption of femstosecond pulses. Appl. Phys. A, **79**, 407-409.

[14] H. Segawa, N. Abrams, T. E. Mallouk, I. Divliansky, and T. S. Mayer, (2006) Fabrication of TiO_2-Organic hybrid dot arrays using nanosecond laser interference lithography. J. Am. Ceram Soc., **89**, 3507-3510.

[15] T. Kondo, S. Juodkazis, V. Vygantas, and H. Misawa, (2006) Holographic lithography of periodic two- and three- dimensional microstructures in photoresist SU-8. Opt. Exp., **14**, 7943-7953.

[16] J. Xing, X. Dong, W. Chen, X. Duan, N. Takeyasu, T. Tanaka, and S. Kawata, (2007) Improving spatial resolution of two-photo microfabrication by using photoinitiator. Appl. Phys. Lett., **80**, 131106.

[17] T. Kondo, S. Matsuo, S. Juodkazis, and H. Misawa, (2001) Femtosecond laser interference technique with diffractive beam splitter for fabrication of threedimensional photonic crystals. Appl. Phys. Lett., **79**, 725.

[18] J. N. Israelachvili, (1992) Intermolecular and surface forces. Academic Press Ltd., London, 2nd ed..

[19] (1984) JSME mechanical engineers' handbook, A4: Strength of materials. Japan Society of Mechanical Engineers, Tokyo.

[20] D. R. Lide ed., (1998) CRC handbook of chemistry and physics, 82th Ed., CRC Press Inc., Boca Raton, Florida.

[21] K. Kintaka, J. Nishii, and N. Tohge, (2000) Diffraction gratings of photosensitive ZrO_2 gel films fabricated with the two ultraviolet beam interference method, Appl.Opt., **39**, 489-493.

[22] N. Tohge and Y. Takama, (1999) Direct fine-patterning of PZT thin films using photosensitive gel films derived from chemically modified metal alkoxides. J. Mater. Sci.: Mater. Electron., **10**, 273-277.

Vol.1, No.3, 181-184 (2009)
doi:10.4236/ns.2009.13023

Natural Science

Hiding data in DNA of living organisms

Shu-Hong Jiao[1], Robert Goutte[2]

[1]Information and Telecom Department, Harbin Engineering University, Harbin, China
[2]Universite De Lyon , Lab Creatis Lrmn, INSA Lyon, France; goutte@creatis.insa-lyon.fr

Received 12 June 2009; revised 16 July 2009; accepted 18 July 2009.

ABSTRACT

Recent research has considered DNA an interesting medium for long-term and ultra compact information storage and a stegomedium for hidden messages. Artificial components of DNA with encoded information can be added to the genome of living organisms, such as common bacteria. With this approach, a medium for very height densities information storage, watermarks for protection patents of genetically modified organisms (GMOs) and secure public keys for decrypting hidden information in steganocryptography, can be obtained. In this paper, we have selected a Bacillus subtilis gene (tatAD) and use the specific properties of silent mutations to obtain a biologically innocuous product. An adapted code for the message insertion in this gene is proposed.

Keywords: DNA; Genome; Coding; Steganography; Living Organism

1. INTRODUCTION

There has been growing interest in using DNA to store information, one the main reasons being the very high storage densities that can be achieved. The durability of DNA would make it particularly useful for preserving archival material over extensive periods of time (long-term storage). Message DNA has been used in computations in biologic mathematics, in steganography and as a mean of short-term trademarks. These different fields use the specific properties of genetic code and the possibilities to encode artificial information.

However, the artificial introduction of a new gene or the modification of an existing gene in the DNA of a living organism, can involve prejudicial deterioration of the behavior and the reproduction of this species. The solution suggested must thus notably allow a great computer security, but also the genetic consequences of their implementation.

2. THE GENETIC CODE

The genetic code is the biochemical basis of heredity and nearly universal in all organisms (eukaryotes or prokaryotes): humans, animals, plants, bacteria and viruses.

DNA (deoxyribonucleic acid) is a long molecule, with two strands rolled up in a double helix. Each strand is formed by sugar phosphate backbone, connected with single molecules called bases, which contain carbon, nitrogen and cyclical structures. The four bases are known as adenine A, thymine T, guanine G and cytosine C.Any strand of DNA adheres to its complementary strand, in which T substitute for A, G for C, and vice versa. The links between pairs of bases are responsible for binding together two stands together to form the double helix.

The genetic information in DNA is found in the ordered sequence of these four bases (the double helix structure of DNA introduces redundant information, resulting in complementary nitrogenous base links).

Unlike DNA, RNA (ribonucleic acid) is a single stranded molecule and does not form of double helix. The bases are the same that DNA, except U (uracil), which replaces T. The complementarily becomes:

$$U \leftrightarrow A \text{ and } G \leftrightarrow C$$

Messenger RNA (mRNA) carries all the genetic information to ribosome for proteins synthesis by the cell.

A codon is a triplet of three bases (T,C,A and G). With these four letters, 43=64 combinations are possible. With three exceptions, each codon encode for one of the 20 amino acids, used in the proteins synthesis (the three exceptions are TAA, TAG and TGA: codons STOP).

ATG correspond at methionine within the gene; at the beginning of the gene, ATG is also a signal START. Ribosome assembles individual amino acids into peptide chains. Peptides are short chains of amino acids that are linked together. If the number of amino acids in the chain reaches around ten or more, such substances are called polypeptides and large polypeptides are called proteins.

First Position	Second Position of Codou T	Second Position of Codou C	Second Position of Codou A	Second Position of Codou G	Third Position
T	TTT Phe [F] TTC Phe [F] TTA Leu [L] TTG Leu [L]	TCT Ser [S] TCC Ser [S] TCA Ser [S] TCG Ser [S]	TAT Tyr [Y] TAC Tyr [Y] TAA Ter [end] TAG Ter [end]	TGT Cys [C] TGC Cys [C] TGA Ter [end] TGG Trp [W]	T C A G
C	CTT Leu [L] CTC Leu [L] CTA Leu [L] CTG Leu [L]	CCT Pro [P] CCC Pro [P] CCA Pro [P] CCG Pro [P]	CAT His [H] CAC His [H] CAA Gln [Q] CAG Gln [Q]	CGT Arg [R] CGC Arg [R] CGA Arg [R] CGG Arg [R]	T C A G
A	ATT Ile [I] ATC Ile [I] ATA Ile [I] ATG Met [M]	ACT Thr [T] ACC Thr [T] ACA Thr [T] ACG Thr [T]	AAT Asn [N] AAC Asn [N] AAA Lys [K] AAG Lys [K]	AGT Ser [S] AGC Ser [S] AGA Arg [R] AGG Arg [R]	T C A G
G	GTT Val [V] GTC Val [V] GTA Val [V] GTG Val [V]	GCT Ala [A] GCC Ala [A] GCA Ala [A] GCG Ala [A]	GAT Asp [D] GAC Asp [D] GAA Glu [E] GAG Glu [E]	GGT Gly [G] GGC Gly [G] GGA Gly [G] GGG Gly [G]	T C A G

Figure 1.1. The genetic code (DNA).

First Position	Second Position of Codou T	Second Position of Codou C	Second Position of Codou A	Second Position of Codou G	Third Position
T	Phe [F] TT	Ser [S] TC	Tyr [Y] TA	Cys [C] TG	T C A G
C	Leu [L] CT	Pro [P] CC	His [H] CA	Arg [R] CG	T C A G
A	Ile [I] AT	Thr [T] AC	Asn [N] AA	Ser [S] AG	T C A G
G	Val [V] GT	Ala [A] GC	Asp [D] GA	Gly [G] GG	T C A G

1) In yellow: The eight blocks with a single amino acid.
2) Blocks repaired with only two first bases.

Figure 1.2. Simplified code.

3. DEGENERACY OF GENETIC CODE

Many codons are degenerate, or redundant, meaning two or more codons (synonymous codons) may code for the same amino acid. See **Figure 1.1.** Degenerate codons typically differ in their third position. (e.g.: GAA, GAC for glutamine). See **Figure 1.2.**

The degeneracy of the genetic code is what accounts for the existence of "silent mutations". A mutation occurs when a DNA gene is damaged or changed. A silent mutation is a mutation that does not alter the amino acid of a gene, usually because of codon ambiguity.

4. STATE OF ART, PROPOSED CODE AND SPECIFIC PROPERTIES

The first paper on hiding messages in DNA was published by T. Clelland and al (ref 1) in 1999 and involved the insertion of a brief message in a sample of human DNA. In 2001, these same authors published a paper showing of possibilities of long-term storage of information in DNA and used a classical codon encoding for the English alphabet. In 2003, C. Smith and al (ref 3) described a possible code for encrypting data.

In DNA and Boris Shimannovsky and al (ref 4) proposed an interesting and original arithmetic code. Pak Chung Wong and al (ref 5) presented new potential applications for DNA organic data memory.

The advantages of these approaches in production keys were presented by Masanori Arita (ref 6) and Tanaka and all, in 2005 (ref 7). Recently, Nozomu Yachie and al (ref 8) presented a very complete methodology, simple, flexible and robust of data storage based on sequence alignment of genomic DNA of living organism. D. Heider and al publish, in 2007, a program called DNA Crypt whose use is centred on the patent protection of genetically modified organisms (GMOs) (ref 9).

In this work we propose a method of coding that satisfies two conditions:

Limitation of changes in the gene marker

Possibility to transfer the encrypted message in a key, made with a polypeptide chain.

5. CHOICE OF SITE

Bacillus subtilis is a non-pathogenic bacterium, which form pores that can survive in extreme conditions. This bacterium is a model which has already been chosen as storage of information by several teams.

To illustrate our proposed code, we have selected a component of this genome: the gene tatAD (alternate name ycbz). See **Figure 1.3.** This gene is very short; its length is 210 base pairs, which correspond to 70 amino acids. It is a protein classified stable.

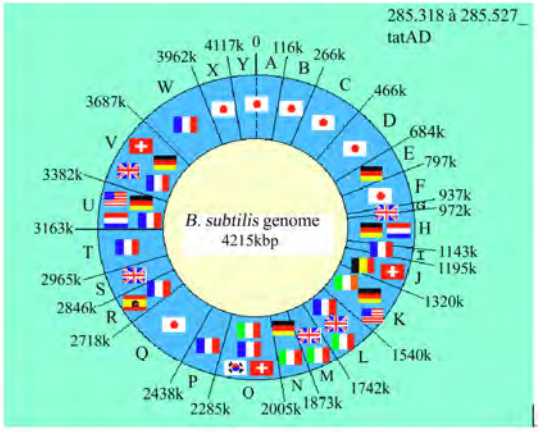

Figure 1.3. Bacillus subtilis.

The following table lists the genetic code of these 70 amino acids

ATG TTT TCA AAC ATT GGA ATA CCG GGC
TTG ATT CTC ATC TTC GTC
ATC GCC ATT ATT ATT TTT GGC CCT TCC AAG CTG CCG GAA ATC GGG
CGT GCC GCG AAA CGG ACA CTG CTG GAA TTT AAC AGC GCC ACA AAC
TCA CTT GTG TCT GGT GAT GAA AAA GAA GAG AAA TCA GCT GAG CTG
ACA GCG GTA AAG CAG GAC AAC AAC GCG GGC

A short list concern only the underlining codons: TCA GGA CCG GGC CTC ……, codons-owned blocks of the **Table 2**, in yellow mark.

6. IMPLEMENTATION

6.1. Encryption

By example, we consider the message "CODING". After translation with ASCII code (with 8 bits per character), this message requires 48 bits.

- C 0 1 0 0 0 0 0 1
- O 0 1 0 0 1 1 1 1
- D 0 1 0 0 0 1 0 0
- I 0 1 0 0 1 0 0 1
- N 0 1 0 0 1 1 1 0
- G 0 1 0 0 1 1 1 1

With the rate of 2 bits per codon, this message requires 24 codons. For his implementation, only 35 codons are selected (codons underlined).The beginning and the end of this message necessarily belongs to these 35 codons, so that only two 6 bits numbers (two times three codons) are needed for their localization.

If we assume that the beginning is located at the 9th codon, and is 48 bits long (24 codons), the end of the message will be located at 32 th codon.

Beginning at 9→ 00 10 01
End at 32→ 01 00 00

Six codons are needed for their localization.

/1 2 3/-//4 5 6//7 8///9 10 11 12 13 14 15 16 17 18 19 20 21 22 23 24 25 26 27 28 29 30 31 32///33 34 35.

The coding consists in replacing the 3rd base of these codons by A, C, G, T according this table:

A if 00 C if 01
G if 10 T if 11

Before coding we, in the first line have

ATG TTT TCA AAC ATT GGA ATA CCG GGC TTG ATT CTC ATC TTC GTC

After coding we obtain:

ATG TTT TCA AAC ATT GGG ATA CCC GGG TTG ATT CTA ATC TTC GTA

The first 24 codons selected on the short list are:

CCT TCC CTC CCG GGG CGT
GCC GCC CGG ACA CTG CTG
GCC ACA TCA CTT GTG TCT
GGT TCA GCT CTG ACA GCG

After coding, we obtain:

CCC TCA CTA CCT GGC CGA
GCT GCT CGC ACA CTC CTA
GCC ACA TCG CTC GTC TCA
GGT TCG GCC CTA ACC GCT

4 codons (underlined) are not modified by the coding. Only 25 codons of the original gene's 70 codons (tatAD) are modified. All the mutations are particular missense mutations: silent mutations; with its location, the encryption of this message requires 60 bits and 25 mutations. Thus, on average, each silent mutation can insert slightly more than 2 bits of hidden message.

6.2. Decryption

Decryption is particularly easy. After obtaining the beginning and the end of the message from the first 6 codons of the shortlist, it is sufficient to replace, in the sequence of codons corresponding to the message, the last base of each codon by its equivalent in bits:

(A→00, C→01, G→10, T→11)

In this example, a very short gene is used for demonstration purposes, but this method can be applied to longer genes, that are more than 10000 base pairs long (such as the gene srfAA de Bacillus subtilis) which then allows the insertion of messages 50 that are time longer (~2400 bits and therefore 300 ASCII characters).

7. MATERIALISATION OF THE KEY, COMPLEMENTS

7.1. Producing the Key

It is possible to replace the list of 30 codon, which can be synthesized and materialized in the form of a polypeptide, as in the preceding example, with a new list of 60 amino acids. Indeed, if we consider the beginning of the Short list (after coding):

TCA GGG CCC ……..We have the possibility to introduce a peptide chain:

Ser (TCA) Gly (GGG) Pro (CCC) ….

But it is not possible, with only this chain, to rediscover the different codons of the short list in reason of the redundancy of the genetic code.

Ser correspond to TCT TCC TCA TCG
Gly to GGT GGG GGA CGG and
Pro to CCT CCC CCA CCG

For resolve this difficulty we propose the following connections:

T C A G G G C C C
/\ /\ /\
T C X C A X' G G X G G X' C C X CCX'

If X =A and X'=C we obtain:

T C A C A C G G A G G C C C A C C C
Ser His Gly Gly Pro Pro

new peptidic chain. With the chain we can retrieve the three codons of the short list

For this, it is sufficient to conserve uniquely two bases/in each codon.

T C C A G G G G C C C C and to regroup:

T C G G C C
C A G G C C

T C A G G G C C C

for obtain the three original codons.

7.2. Complements

It is possible to associate this encryption method with a binary encryption algorithm (AES, RSA, Blowfish). In this case, the inserted message is not the clear version, but a secure version after using these specific algorithms.

7.3. Simplified Version

If, in spite of the precaution to using silent mutations during the identification of genetically modified organisms, residual biological changes still exist in the host organism, then a simplified version of the method discussed above can be used.

From the gene initially modified by the agrochemical firm (if this gene is accessible to the user), we propose to use this gene as stegomedium, to produce a custom key. This key can allow access to the reference of manufacturer. With this goal in mind, in the preceding example (with the message "CODING" of 48bits), we select 24 codons of the 70 existing in the tatAD gene.

Each codon selected is identified by its rank in the chain (7 bits per codons are necessary, here corresponding to a total of 24x7=168 bits). These 168 bits are the customized key (customizations results from the different possible orders in this gene's chain), The last base of the codon selected (A,T,C or G) allows access to the bits 01, 10 ,00, 11 that form the message. It is important to note that the marker gene is not altered by this operation. Information on origin and dates of manufacture concerning these seeds can be obtained. Security comes both the use of the key and the specific nature of the changes, made voluntarily by the manufacturer on the original gene, for obtain the desired biological effects.

8. CONCLUSIONS

The use of the degeneracy of the genetic code and, in particular, the silent mutations, produces coding that does not practically alter the properties of the inserted gene, nor the characteristics of the host genome (very important conditions when we working with the live organisms). Memorization of the key information and the production of the hidden message in the form of a physical polypeptide provide additional data transfer security, while the coding protocol is being implemented).

DNA is a storage medium extremely effective: it is compact and his signature is innocuousness and secrecy. In the spore form, Bacillus subtilis is resistant to extremes terrestrial and extraterrestrial environment during the interstellar travel, for example (ref 10). In the nearly future, this bioengineering method can be used in routine, for protection of the gene patents, digital copyrights and tool for the marking in biodiversity

REFERENCES

[1] C. C. Taylor, V. Risca, and C. Bancroft, (1999) Hiding messages in DNA microdots. Nature, **399**, 533-534.

[2] C. Bancroft, T. Bowler, B. Bloom, and C. C. Taylor (2001) Long-term storage of information in DNA. Science, **293(5536)**, 1763-1765.

[3] G. C. Smith, C. C. Fiddes, J. P. Hawkins, and J. P. L. Cox, (2003) Some possible codes for encrypting data in DNA. Biotechnology, **25**, 1125-1130.

[4] B. Shimanovsky, J. Feng, and M. Potkonjak, (2003) Hiding data in DNA, LNCS **2578**, 373-386.

[5] P. C. Wong, K. K. Wong, and H. Foote, (2003) Organic data memory using the DNA approach, Communication of the ACM, **46(1)**.

[6] M. Arita and Y. Ohashi, (2005) Secret signature inside genomic DNA biotechnol. Prog, **20 (5)**, 1605-1607.

[7] K.Tanaka, A. Okamoto, and I. Saito, (2005) Public-key system using DNA as a one way function for key distribution. Biosystems, **81(1)**, 25-29.

[8] N. Yachie, K. Sekiyma, J. Sugahara, Y. Ohashi, and M. Tomita, (2007) Alignment-based approach for durable data storage into living organisms biotechnol. Prog., **23**, 501-505.

[9] D. Heider and A. Barnekow, (2007) DNA-based watermarks using the DNA-Crypt algorithm, BMC Bioinformatica, **8**, 176.

[10] W. L. Nison, N. Munakata, G. Horneck, H. J. Melosh, and P. Setlow, (2000) Resistance of Bacillus endospores to extreme terrestrial and extraterrestrial environments. Micbiol. Mol. Bio. Rev., **64(3)**, 548-57.

Vol.1, No.3, 185-190 (2009)
doi:10.4236/ns.2009.13024

Natural Science

Preparation of lignin derivatives and their application as protease adsorbents

Run Fang[1,2], Yin Lin[1] Xian-Su Cheng[*1]

[1]College of Material Science and Engineering, Fuzhou University, Fuzhou, China
[2]Department of Chemistry and Chemical Engineering, Minjiang University, Fuzhou, China; Corresponding author: cxs2222@sina.com

Received 1 September 2009; revised 25 September 2009; accepted 27 September 2009.

ABSTRACT

Synthesis of two lignin derivatives, lignophenol and lignin-aminophenol, were presented in this article. The chemical structure and the functional groups of lignin derivatives were characterized through FT-IR analysis. The immobilization of three proteases (papain, trypsin and pepsin) on lignin and lignin derivatives was carried out using adsorption technique. The influence of contact time and pH on the enzyme adsorption by different adsorbents was investigated. Furthermore, enzyme activity recovery was also evaluated. Results showed that lignin and lignin derivatives could adsorb proteases effectively and the adsorption capacity of lingophenol and lignin-aminophenol was higher than that of pure lignin. Meanwhile, the activity recovery of papain and pepsin immobilized on lignin derivatives was very high. This phenomenon suggested that there is a supramolecular interaction between enzymes and lignin derivatives which do not inhibit enzyme activity. Therefore, lignophenol and lignin-aminophenol are both promising adsorbents for enzyme immobilization under acid and neutral conditions.

Keywords: Lignin Derivative; Papain; Trypsin; Pepsin; Adsorption

1. INTRODUCTION

Papain, trypsin and pepsin are all of proteases found in plant and animal cells that break down proteins or peptides by catalyzing the hydrolysis of peptide bonds. These enzymes, after being immobilized, offer several advantages over their free form equivalent. Examples include better stability, possible reuse, greater sensitivity and greater reproducibility of effectiveness. The immobilization technology of enzyme has been playing an important role in biological industry, medicine and clinical diagnosis, chemical analysis, environmental protecttion and energy exploitation. Apart from recycling the biocatalyst, immobilization yields further advantages, such as the easy removal of the biocatalyst from the reaction mixture and thus, simplified product purification. Different immobilization techniques have been developed including covalent coupling [1,2], enzyme crosslinking molecules [3], adsorption on a carrier [4] and the encapsulation in polymeric gels or membranes [5,6].

Support material is a key factor in enzyme immobilization and considerable attention has been paid to the searching for ideal support materials, which may give the best combination of high remaining activity, low cost and friendly to human health and environment. Lignin (EH-lignin) isolated from the residue of enzymatically hydrolyzed cornstalks (a by-product of fuel ethanol industry) is a novel organosolv lignin developed in recent years [7]. Making use of this biomaterial will not only enhance economic benefits of bioindustry but also diminish potential environmental pollutions.

Lignin is a totally renewable aromatic polymer noted for its versatility and applicability in a variety of uses. Since they are safe to human consumption and environment, some lignin derivatives can even been used as food additives which has been permitted by EPA and FDA. Due to the unique isolation procedures, the content of polar functional groups, such as carbonyl, hydroxyl and phenolic hydroxyl, is very high in EH-lignin. This characteristic makes it possible to utilize EH-lignin, after mild modification, as enzyme immobilization supports. Furthermore, the crosslink structure of modified lignin is helpful in improving the chemical and structure stability of support materials. Enzymes immobilized on lignin derivatives are advantageous because of the capability of transferring active compounds to heterogeneous reactions and the easy separation of them from the reaction mixture subsequently.

The adsorption of endotoxin and bromelain on lignin and lignin derivatives has been reported in our previous works [8,9]. It has been found that lignin derivatives,

prepared through phenol or amino modification, are ideal supports for enzyme immobilization with good adsorption capacity and high remaining activity. In this work, we present the synthesis of two lignin derivatives (lignophenol and lignin-aminophenol) and their application as protease adsorbents. The immobilization of three proteases (papain, trypsin and pepsin) on EH-lignin and lignin derivatives was evaluated by measuring the enzyme adsorption capacity and the activity recovery. The influence of contact time and pH on the enzyme adsorption was discussed in detail.

2. EXPERIMENTAL

2.1. Materials

EH-lignin was isolated from the residue of enzymatically hydrolyzed cornstalks and purified in laboratory according to the procedures described in literature [7]. Papain, trypsin and pepsin as well as 4-aminophenol and 4-cresol were purchased from Sinopharm Chemical Reagent Co., Ltd, China. All other reagents were of analytical grade.

2.2. Preparation of Reagents

The papain, trypsin and pepsin solutions with different pH were prepared by dissolving a certain amount of solute in 0.1mol/l phosphate buffer, 0.05mol/l Tris-HCl buffer and 0.05mol/l lactic acid and sodium lactate buffer respectively. Thermo Orion 828 (Orion, U.S.) pH meter was employed in determining pH values of the solutions.

2.3. Preparation of Lignophenol and Lignin-Aminophenol

Lignophenol was prepared by modifying EH-lignin in a two-phase system composed of p-cresol and 72% sulfuric acid. The preparation procedures and the characteristics of lignophenol were introduced in our previous works [10].

Synthesis of 4-aminophenol modified EH-lignin (lignin-aminophenol) was carried out in a jacketed reactor flask equipped with a stirrer and a reflex condenser. 0.5mol/l 4-aminophenol solution was prepared by adding 3g 4-aminophenol into 55ml distilled water in the reactor and dissolved at 80℃. 5g EH-lignin and 35ml glyoxal was then added into this solution with stirring. After 1h reaction at 80℃, the precipitates were filtered, washed with distilled water and ethanol repeatedly and then dried in a vacuum oven at 50℃ until a constant weight was obtained. Spectrum 2000 FT-IR spectrometer (Perkinelmer, U.S.) was employed in FT-IR analysis of the derivatives.

2.4. Adsorption of Enzyme on Lignin and Lignin Derivatives

50mg support material (EH-lignin, lignophenol and lignin-aminophenol) was incubated with 5ml enzyme solution in a shaker at 25℃ for a period of time, the initial enzyme concentration C_0 was varied depending on experiments. At the end of this period, the supernatant was separated by centrifuging at 3000 rev/min and then diluted with buffer to 25mL. Meanwhile, the precipitate was collected and vacuum dried for enzyme activity assay. The amount of immobilized enzyme was determined by measuring the concentration of the free enzyme in the supernatant before and after adsorption with Cary50 UV/VIS spectrophotometer (Varian, U.S.). Reference samples were prepared according to identical procedures described above by adding 5mL buffer instead of enzyme solutions.

2.5. Enzyme Activity Assay

The activities of free enzymes were determined by measuring the tyrosine amount produced by enzyme-catalyzed hydrolysis of casein according to Chinese drug standards: papain [11]. One unit of enzyme activity is defined as the amount of enzyme that produces 1μg tyrosine from casein per min at 40℃. The concentration of tyrosine was determined at 275nm using UV/VIS spectrophotometer. The activity of enzymes immobilized on EH-lignin and its derivatives was measured using the same method as above, except that the enzyme solutions were replaced by a given amount of immobilized enzymes.

3. RESULTS AND DISCUSSIONS

3.1. Characteristics of Lignin and Lignin Derivatives

EH-lignin is a kind of organosolv lignin isolated from the residue of enzymatically hydrolyzed cornstalks. Compared with traditional lignin derivatives, such as lignosulfonate, EH-lignin possesses some valuable characteristics such as high content of functional groups, less impurities and narrow molecular weight distribution [12].

In the 4-cresol concentrated acid system, lignin fractions contact with acid for a short time may give reactive carbocations (α C^+), which are stabilized quickly by 4-cresol and results in the formation of diphenyl-methane type materials (lignophenol) presented in **Figure 1**. Preliminary studies show that lignophenol is a kind of cross-linked polymer with lots of phenolic hydroxyl groups [10].

Lignin-aminophenol was prepared by modifying EH-lignin with 4-aminophenol, glyoxal act as cross-linking agent. By introducing amino and phenolic hydro- xyl groups into EH-lignin, the enzyme adsorption capacity

and the molecular structure of lignin- aminophenol were of great difference to that of native EH-lignin. FT-IR spectra of EH-lignin, lignophenol and lignin-aminophenol are presented in **Figure 2**. It can be found in the spectrum of lignin-aminophenol that, compared with EH-lignin, the relative intensity of the adsorption bands at 3200-3600cm^{-1} (assigned to –OH and –NH_2 stretching vibration) and 1637cm^{-1} (assigned to N–H bending vibration) increase significantly while the intensity of other bands remain nearly unchanged. Similar phenomenon can be observed in the spectrum of lignophenol at 3200-3600cm^{-1} (assigned to –OH stretching vibration). Therefore, it can be tell from FT-IR analysis that the content of –OH on lignophenol and the content of –OH and –NH_2 on lignin-aminophenol have been greatly enhanced after modification.

3.2 Adsorption of Enzymes on Lignin and Lignin Derivatives

The influence of contact time (t) and initial pH of enzyme solution on the adsorption amount of different enzymes on EH-lignin, lignophenol and lignin- aminophenol were studied in this paragraph.

For initial pH studies, the papain solutions were prepared with phosphate buffer, pH vary form 5.0 to 8.0; the trypsin solutions were prepared with Tris-HCl buffer, pH vary form 7.0 to 9.0 and the pepsin solutions were prepared with lactic acid and sodium lactate buffer, pH form 2.5 to 5.0. The initial concentration of enzyme was C_0=5.0 mg/ml and the contact time t=50 min. For contact time studies, the papain solutions were prepared with phosphate buffer pH 8.0, the trypsin solutions were prepared with 0.05mol/L Tris-HCl buffer pH 9.0 and the pepsin solutions were prepared with 0.05mol/L lactic acid and sodium lactate buffer pH 3.0. The initial concentration of enzyme was 3.0 mg/ml. All the adsorption experiments were performed at 25℃ according to procedures mentioned in 2.5.

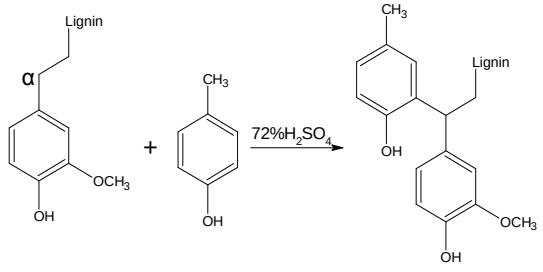

Figure 1. Molecular structure of lignophenol.

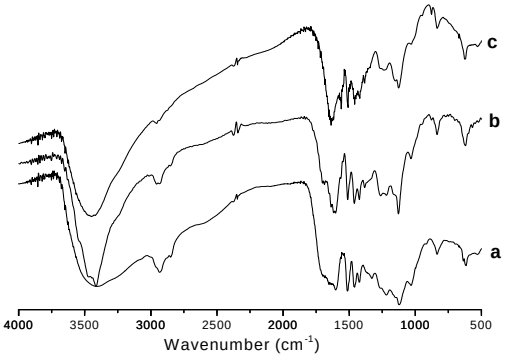

Figure 2. IR spectra of (a) EH-lignin; (b) lignophenol; (c) lignin-aminophenol.

3.2.1. Effect of pH

The influence of pH on the adsorption amount of papain, trypsin and pepsin on lignin and lignin derivatives is presented in **Figure 3. Figure 3a** shows the papain adsorption by different support materials at pH 5.0, 6.0, 7.0 and 8.0. In these cases, the adsorption of papain increased with increasing pH. The maximum adsorption amount 265 mg.g^{-1} was reached at pH 8.0 by lignin-aminophenol and 193 mg.g^{-1} at pH 8.0 by lignophenol. Similarly, the adsorption amount of trypsin on three adsorbents (**Figure 3b**) increased with the rising of pH until equilibrium was reached at pH 8.0-9.0. The maximum adsorption amount 233 mg.g^{-1} was reached at pH 9.0 by lignin-aminophenol and 171 mg.g^{-1} at pH 9.0 by lignophenol. The variation of adsorption amount of pepsin (**Figure 3c**) was a little different from that of papain and trypsin. With increasing pH, three peaks of adsorption amount on different adsorbents appeared at pH 3.0 simultaneously. Further increase of pH led to the decrease of enzyme adsorption amount. The largest adsorption amount was 361 mg.g^{-1} by lignin-aminophenol and 344 mg.g^{-1} by lignophenol.

It has been reported that the isoelectric point of papain is pH 8.6 [13]. Meanwhile, we noticed that the adsorption amount of papain on three adsorbents increased with the rising of pH value, especially when it was close to the isoelectric point of papain. Similarly, the adsorption amount of trypsin and pepsin reached the maxima when the pH values were closed to their isoelectric point, i.e. about 8.2 and 2.8 respectively [14,15].

This phenomenon may be related to induce polarization that the variation of pH leads to a corresponding change in the relative abundance of positive and negative sites on the adsorbents and enzymes, thus modulating the strength of the electrostatic interactions between them.

3.2.2. Effect of Contact Time

The influence of contact time on the adsorption amount of papain, trypsin and pepsin on three different adsorbents is shown in **Figure 4**.

It can be seen in **Figure 4a** that the adsorption of papain by lignin and lignin derivatives was rapid in the first 30 min and a contact time of only 1h was required to attain the equilibrium adsorption. The adsorption amounts of papain on lignophenol and lignin-aminophenol increased up to the highest level i.e. 189 mg/g^{-1} at 50 min and 259 mg/g^{-1} respectively at 70 min respectively, and then remained almost constant. Similar adsorption

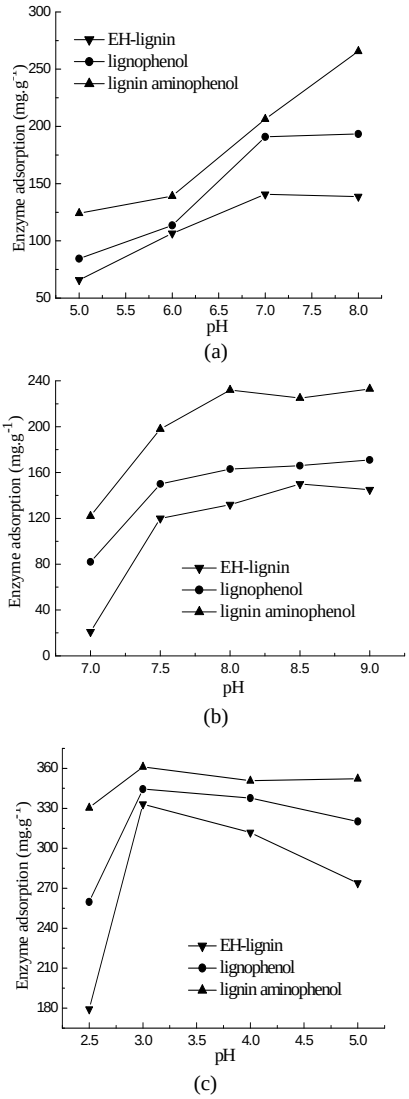

Figure 3. Influence of initial pH of enzyme solution on the adsorption amount of three proteases. C_o=5.0 mg/ml, t=50min,T=25℃ (a) papain; (b) trypsin; (c) pepsin.

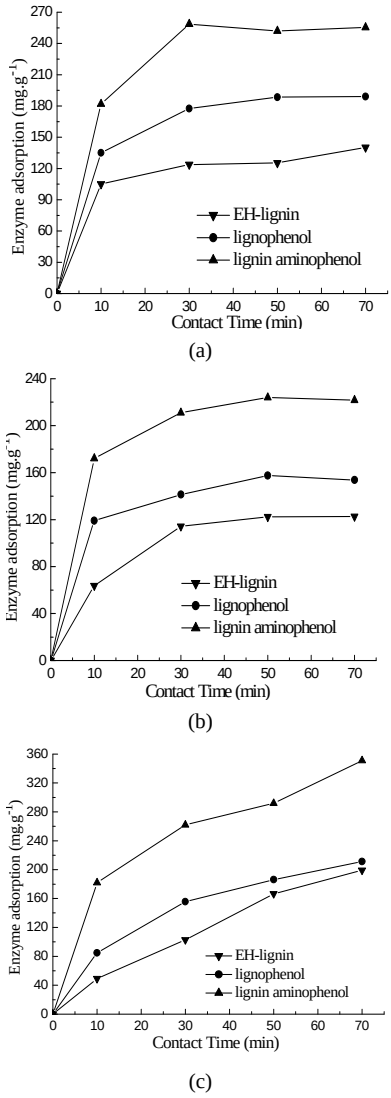

Figure 4. Influence of contact time on the adsorption amount of three proteases. C_o=3.0 mg/ml, T=25℃ (a) papain at pH 8; (b) trypsin at pH 9; (c) pepsin at pH 3.

behavior can be seen in **Figure 4b**. The adsorption of trypsin reached a maximum value of 158 mg/g^{-1} by lignophenol and 224 mg/g^{-1} by lignin-aminophenol at 50min. The adsorption of pepsin (**Figure 4c**) increased steadily with extending contact time and the highest adsorption amount was 211 mg/g^{-1} at 70min by lignophenol and 351 mg/g^{-1} at 70min by lignin-aminophenol. In all these studies, the sequence of enzyme adsorption amount goes as follows: lignin-aminophenol > lignophenol > EH-lignin.

It can be found from **Figure 3** and **Figure 4** that the adsorption amount of pepsin on lignin derivatives is higher than that of papain and trypsin, which may indicated stronger interactions between lignin derivatives and pepsin. The features of their chemical structure and the higher adsorption capacity of lignin derivatives under acid condition are both possible reasons.

Despite the variation of contact time and initial pH, the sequence of enzyme adsorption amount of three support materials goes unchanged as follows: lignin-aminophenol > lignophenol > EH-lignin. Therefore, it is clear that the enzyme adsorption capacity of lignin derivatives increase significantly after modification. On considering the chemical structure, as has been mentioned in 3.1, the content of phenolic hydroxyl groups was increased in lignophenol and both of amino and phenolic hydroxyl groups were enriched in lignin-aminophenol after modification. These polar functional groups, which may interact with amino and carboxyl groups on enzymes, will favor the enzyme adsorp-

Table1. The activities of three proteases before and after adsorption.

Proteases	Adsorbent	Before adsorption /U·mg^{-1}	After adsorption /U·mg^{-1}	Activity recovery /%
Papain	EH-lignin	1.68×10^3	0.19×10^3	11.3
	lignophenol	1.16×10^3	0.65×10^3	55.7
	lignin-aminophenol	0.96×10^3	0.51×10^3	53.1
Trypsin	EH-lignin	6.98×10^3	0.52×10^3	7.5
	lignophenol	1.37×10^4	0.13×10^4	9.6
	lignin-aminophenol	1.42×10^4	0.31×10^4	21.5
Pepsin	EH-lignin	5.15×10^3	0.65×10^3	12.6
	lignophenol	6.62×10^3	5.00×10^3	75.5
	lignin-aminophenol	5.20×10^3	3.65×10^3	70.3

tion through the formation of hydrogen bonding [16,17]. Furthermore, due to their hydrophilic characteristic, the introduction of amino and hydroxyl groups into support materials will lead to a better contact between lignin derivatives and free enzymes suspended in aqueous solution and thus, a larger quantity of enzymes become linked.

3.3. Remaining Activity Analysis

The remaining activities of immobilized enzymes were evaluated and the results were compared to that of free enzymes. Since we have already investigated the influence of adsorption time and pH value on enzyme adsorption, the optimum conditions mentioned in 3.2.1 were used in the activity recovery experiments. The activities of free and immobilized enzymes were determined following the method mentioned in 2.6.

Table 1 shows the activities of papain, trypsin and pepsin before and after adsorption by lignin and lignin derivatives. It can be seen in **Table 1** that the activities recovery of all three proteases immobilized on lignophenol and lignin-aminophenol is higher than that of proteases adsorbed by native EH-lignin. Compared with EH-lignin, the larger enzyme adsorption capacity of lingophenol and lignin-aminophenol is an important factor that leads to higher activity recovery which has been discussed in 3.2. Another factor, the interaction between enzymes and support materials, also makes a contribution to this outcome. Enzyme immobilization can causes changes in the tertiary structure of the protein which in turn may influence the activity under specific conditions. Therefore, the activity decrease after immobilization can be explained by the intermolecular interaction between enzymes and support materials that change the conformation of the enzymes. The high activity recovery of papain and pepsin adsorbed on lignophenol and lignin-aminophenol indicates a supra-molecular interaction between enzymes and lignin derivatives which has little side-effect on the activity of the enzymes. Modified EH-lignin is a high molecular composed of phenylpropane skeleton as the hydrophobic group and amino, hydroxyl and carboxyl as the hydrophilic groups. Therefore, the supramolecular interaction may be a combination of hydrogen bonding and hydro- phobic interaction [18].

Another phenomenon that deserves our attention is the significant difference of the activity recovery between three enzymes adsorbed on the same adsorbent. Despite the variation of support materials, the sequence of activity recovery of three enzymes goes unchanged as follows: pepsin > papain > trypsin. The variation of adsorption amount of three enzymes is a factor that will affect the activity recovery. However, as was shown in 3.2, the adsorption amount of different enzymes on the same support material do not differ a great deal, which means that other influencing factors should also be taken into account.

From the standpoint of the physical characteristics, this phenomenon may be ascribed to the influence of pH on the dissolution of lignin and lignin derivatives in aqueous solutions. It has been pointed out in some studies that as the pH of the solution increases, the dissolvability of lignin and lignin derivatives will increase simultaneously [19]. It was also found in our research that when the buffer turned to alkaline, the dissolvability of lignin and lignin derivatives increased rapidly. The adsorption of pepsin, papain and trypsin was carried out under the optimum conditions at pH 3.0, 8.0 and 9.0, respectively. The dissolution of support materials under alkaline condition decreased the stability and the yield of immobilized enzymes, which in turn reduced the activity recovery of trypsin remarkably. These analyses indicate that lignin and lignin derivatives are more suitable for papain and pepsin immobilization under acid or neutral conditions.

4. CONCLUSIONS

The preparation and characteristics of two lignin derivatives, lignophenol and lignin-aminophenol, was presented in this article. Compared with native lignin, the content of amino and phenolic hydroxyl groups was greatly enhanced after modification.

The results received from adsorption experiments show that three proteases (papain, trypsin and pepsin) can be adsorbed by lignin and lignin derivatives effectively. The adsorption capacity was affected by contact

time and pH depending on the feature of enzymes. Despite the variation of enzymes, the sequence of enzyme adsorption capacity goes as follows: lignin-aminophenol > lignophenol > EH-lignin, which is attributed to the enrichment of polar functional groups, such as –OH and $–NH_2$, in lignin derivatives after modification.

The activity recovery of pepsin and papain immobilized on lignin derivatives under acid and neutral conditions was very high which indicates a combination of hydrogen bonding and hydrophobic interaction between enzymes and lignin derivatives. These intermolecular interactions greatly enhance enzyme adsorption and hardly inhibit enzyme activity. Therefore, lignophenol and lignin-aminophenol are promising support materials for enzyme immobilization under acid and neutral conditions.

5. ACKNOWLEDGEMENT

This paper has received support from the fund of State Key Laboratory of Guangzhou Institute of Chemistry, Chinese Academy of Science (LCLC-2004-158）.

REFERENCES

[1] F. Hildebrand and S. Lutz, (2006) Immobilization of alcohol dehydrogenase from *Lactobacillus brevis* and its application in a plugflow reactor. Tetrahedron Asymmetry, **17**, 3219-3225.

[2] C. Mateo, O. Abian, L. R. Fernandez, and J. M. Guisan, (2000) Increase in conformational stability of enzymes immobilized on epoxy-activated supports by favoring additional multipoint covalent attachment. Enzyme Microb. Technol., **26**, 509–515.

[3] R. Schoevaart, M. W. Wolbers, M. Golubovic *et al*., (2004) Preparation, optimization and structures of cross-linked enzyme aggregates (CLEAs). Biotechnol. Bioeng., **87**, 754-762.

[4] R. A. Sheldon, R. Schoevaart, and L. M. Van Langen, (2005) Cross-linked enzyme aggregates (CLEAs): A novel and versatile method for enzyme immobilization. Biocatal. Biotransform., **23**, 141-147.

[5] A. C. Pierre, (2004)The sol-gel encapsulation of enzymes. Biocatal. Biotransform., **22**, 145-170.

[6] L. Veum, U. Hanefeld, and A. Pierre, (2004) The first encapsulation of hydroxynitrile lyase from *Hevea brasiliensis* in a sol-gel matrix. Tetrahedron, **60**, 10419-10425.

[7] X. S. Cheng and X. L. Liu, (2006) Separation of lignin from cornstalks residue by enzymatic hydrolysis and its properties. Morden Chemical Industry, Supplement, **26**, 99-102.

[8] X. H. Zhang, X. S. Cheng, and J. Tang. (2006) Adsorption of bromelain with HBS lignin and its derivatives. The Chinese Journal of Process Engineering, **6**, 87-90.

[9] Y. Q. Jin and X. S. Cheng, (2006) Study on the adsorption of endotoxin by HBS lignin and its derivatives. Journal of Xi'an University of Engineering Science and Technology, **20**, 723-726.

[10] M. J. Li and X. S. Cheng, (2004) Research on the adsorption of endotoxin by lignophenol. Journal of Cellulose Science and Technology, **12**, 1-6.

[11] Y. X. Luo, (2000) Studies on the determination of enzymatic active for papain. Chinese Pharmaceutical Journal, **35**, 556-558.

[12] R. Fang, X. S. Cheng., J. Fu., and Z. B. Zheng, (2009) Research on the graft copolymerization of EH-lignin with acrylamide. Natural Science, **1**, 17-22.

[13] S. Solis, J. Paniagua, J. C. Martınez, and M. Asomoza, (2006) Immobilization of papain on mesoporous silica: pH effect. J. Sol-Gel Sci. Technol., **37**, 125-127.

[14] L. Qiao and Y. Liu, (2008) A nanoporous reactor for efficient proteolysis. Chem. Eur. J., **14**, 151-157.

[15] M. Casas1 and J. Miñones1, (1992) Effect of polymerized silicic acid on mixed lipid-protein monolayers used as cell-membrane models II pepsin-sphingomyelin films. Colloid. Polym. Sci., **270**, 485-491.

[16] S. Dumitriu, P. Magny, D. Montane, P. F. Vidal, and E. Chornet, (1994) Polyionic hydrogels obtained by complexation between xanthan and chitosan: their properties as supports for enzyme immobilization. J. Bioact. Compat. Polym., 9, 184-209.

[17] N. Dizge, C. Aydiner, E. Demirbas, M. Kobya, and S. Kara, (2008) Adsorption of reactive dyes from aqueous solutions by fly ash: Kinetic and equilibrium studies. J. Hazard. Mater., **150**, 737–746.

[18] B. Al-Duri and Y. P. Yong, (2000) Lipase immobilisation: An equilibrium study of lipases immobilised on hydrophobic and hydrophilic/hydrophobic supports. Biochem. Eng. J., **4**, 207–215.

[19] P. Kauper, (2004) From production to product Part 1: Solution states of alkaline bagasse lignin solution. Industrial Crops and Products, **20**, 151-157.

Vol.1, No.3, 191-194 (2009)
doi:10.4236/ns.2009.13025

Natural Science

Behaviour of radioactive iodide and bromide ions from aqueous solution on ion exchange resins Amberlite IRA-400

Pravin Singare[1*], Ram Lokhande[2]

[1]Department of Chemistry, Bhavans College, Mumbai, India
[2]Department of Chemistry, University of Mumbai, Mumbai, India

Received 15 June 2009; revised 2 July 2009; accepted 5 July 2009.

ABSTRACT

The ion exchange resin Amberlite IRA-400 in iodide and bromide form where equilibrated separately with the respective labeled iodide and bromide ion solution of different concentrations varying from 0.005M to 0.100M in the temperature range of 32.0 °C to 48.0 °C. The distribution coefficient K_d values calculated for iodide and bromide ion exchange increases with rise in ionic concentration of the external solution, however with rise in temperature the K_d values calculated where found to decrease. Also the K_d values calculated where higher for iodide exchange than bromide exchange. Among the different alternative techniques available for obtaining the K_d values, the radioactive tracer technique used in the present experimental work offers high detection sensitivity. It is expected that the distribution coefficient data obtained from such experimental work will significant in environmental impact assessment on the disposal of radioactive waste.

Keywords: Ion Exchange Resin; Amberlite IRA-400; Distribution Coefficient; Temperature Effect; Concentration Effect; ^{131} I; ^{82} Br; Radioactive Tracer Isotope

1. INTRODUCTION

There are number of liquid processes and waste streams at nuclear power plants, fuel reprocessing plants and nuclear research centers that require treatment for removal of radioactive contaminants. One of the most common treatment methods for such aqueous streams is the use of ion exchange, which is a well developed technique that has been employed for many years in nuclear industries [1,2]. The ion exchange process is very effective at transferring the radioactive content of a large volume of liquid into a small volume of solid. Efforts to develop new ion exchangers for specific applications are continuing. In spite of their advanced stage of development, various aspects of ion exchange technologies have been continuously studied to improve the efficiency and economy of their application in radioactive waste management. The selection of an appropriate ion exchange material for the liquid radioactive waste treatment is possible on the basis of information provided by the manufacturer. However since the selection of the appropriate ion exchange material depends on the needs of the system, it is expected that the data obtained from the actual experimental trials will prove to be more helpful. Generally the selected ion exchange materials must be compatible with the chemical nature of the radioactive liquid waste such type and concentration of ionic species present as well as the operating parameters notably temperature. Also while designing an ion exchange processing system it is desirable to have an adequate knowledge of the distribution coefficient values of the ion exchange resin towards different ions present in radioactive liquid waste. These distribution coefficients are very important parameter for environmental impact assessment on the disposal of radioactive waste arising from research institutes [3].

Although there are different alternative methods available to know the distribution coefficient values, but radioactive isotopic technique is expected to be the most appropriate method as it offer several advantages such as high detection sensitivity, capability of in-situ detection, and physico-chemical compatibility with the material under study [4-8]. Attempts where made by the previous researchers to study the concentration and temperature effect on cation exchange systems for computing the distribution coefficient values [9-15]. However very little work was done to study the distribution coefficient values in anion exchange systems [16]. Therefore, in the present investigation, attempts where made to study the effect of external ionic concentration and temperature on

distribution coefficient, for which radioactive tracer technique was used.

2. EXPERIMENTAL

Ion exchange resin Amberlite IRA-400 (by Rohm and Haas Company, USA), was a strongly basic anion exchange resin in chloride form. The resins where converted in iodide and bromide form by eluting with 10 % KI and KBr solution in a conditioning column. The 1.000 g (***m***) of conditioned resins in iodide and bromide form was equilibrated separately with labeled 250 mL (***V***) of 0.005 M iodide and bromide ion solution respectively under continuous and uniform mechanical stirring. The solution was uniformly stirred using the mechanical stirrer for 3h at a constant temperature of 32.0 ^{0}C so as to attain equilibrium.

The ion exchange reaction taking place can be represented as follows:

$$R\text{-}I + I^{*-}_{(aq.)} \rightleftharpoons R\text{-}I^{*} + I^{-}_{(aq.)} \quad (1)$$

$$R\text{-}Br + Br^{*-}_{(aq.)} \rightleftharpoons R\text{-}Br^{*} + Br^{-}_{(aq.)} \quad (2)$$

where $I^{*-}_{(aq.)}$ and $Br^{*-}_{(aq.)}$ represent aqueous solution of iodide and bromide labeled with radioactive isotope ^{131}I and ^{82}Br respectively.

The initial activity (A_i) and final activity (A_f) in counts per minutes (c.p.m.) of the labeled solutions was measured on γ-ray spectrometer having Na (I) Tl scintillation detector. From the knowledge of A_i and A_f, the K_d value was calculated by the equation

$$K_d = [(A_i - A_f) / A_f] \times V / m \quad (3)$$

The experimental sets where repeated in the same manner by increasing the ionic concentrations up to 0.100 M and the temperature varying up to 48.0 ^{0} C. The K_d values for different sets where calculated by **Eq.3**.

The ^{82}Br isotope used was an aqueous solution of ammonium bromide in dilute ammonium hydroxide having activity 5mCi, γ- energy 0.55 MeV, and $t_{1/2}$ 36h. The ^{131}I isotope used was an aqueous solution of sodium iodide in dilute sodium sulfite, having activity 5mCi, γ-energy 0.36 MeV, and $t_{1/2}$ 8.04d [17].

3. RESULTS AND DISCUSSIONS

In the present research work the ion exchange resin in iodide and bromide form where equilibrated for 3 h with labeled iodide and bromide ion solution respectively of known initial activity. From the results of previous work [4-8,18-24]; it was observed that this time duration was sufficient to attain equilibrium. Due to ion isotopic exchange reactions taking place the activity of the solution decreases with time. The decrease in activity of the solu

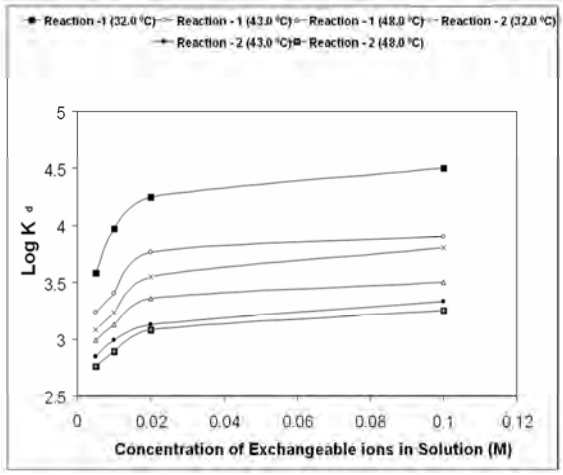

Figure 1. Variation of distribution coefficient with ionic concentration and temperature.

Table 1. Effect of ionic concentration on distribution coefficients. Temperature = 32.0 ^{0}C, amount of resin= 1.000 g, volume of solution = 250 mL.

Concentration (M)	Log Kd	
	Iodide ions	Bromide ions
0.005	3.58	3.08
0.010	3.97	3.23
0.020	4.25	3.55
0.100	4.50	3.80

Table 2. Effect of temperature on distribution coefficients. Concentration of labeled ionic solution = 0.005M, amount of resin= 1.000 g, volume of solution = 250 mL.

Temperature ^{0} C	Log Kd	
	Iodide ions	Bromide ions
32.0	3.58	3.08
43.0	3.23	2.85
48.0	2.99	2.76

tion was measured after 3h which represent the final activity exchanged on the resin. From the knowledge of initial and final activity, the K_d values where calculated by **Eq.3** to study the effect of temperature and concentration. Heumann *et al.* [16] in the study of chloride distribution coefficient on strongly basic anion-exchange resin observed that the selectivity coefficient between halide ions increases at higher electrolyte concentrations. Adachi *et al.* [9] observed that the swelling pressure of

the resin decreased at higher solute concentrations resulting in larger distribution coefficient values. The temperature dependence of the distribution coefficient on cation exchange resin was studied by Shuji *et al.* [11], they observed that the distribution coefficients increased with decreasing temperature. The present experimental results also indicates that the distribution coefficient K_d values calculated for iodide and bromide ions increases with increase in ionic concentration of the external solution (**Table 1**), however with rise in temperature the K_d values calculated where found to decrease (**Table 2**). Also the K_d values calculated where higher for iodide ions as compared to that for bromide ions (**Tables 1** and **2**). The variation of K_d values for iodide and bromide ions with temperature and concentration of external ionic solution is graphically represented in **Figure 1**.

4. CONCLUSIONS

In heavy metal removal processes the rate of removal is considered to be important factor from the practical aspect of reactor design and process optimization [25]. Earlier research was performed demonstrating the feasibility of using the bioresin in a continuous system for decontaminating pool water of ^{60}Co [26]. It is important here to note that in all the above decontamination processes, distribution coefficient K_d values plays a very prominent role in deciding about proper selection of resins. The work carried out in the present experiment is a demonstration showing application of radioactive active tracer technique to study the parameters affecting the distribution coefficient. The same technique can be extended further to study the K_d values of different ion exchange resins for various ions in liquid radioactive waste. The data base so obtained on K_d value will serve as a very important parameter for environmental impact assessment on the disposal of radioactive waste [3].

REFERENCES

[1] (1967) International atomic energy agency, operation and control of ion exchange processes for treatment of radioactive wastes. Technical Reports Series, **78**, IAEA, Vienna.

[2] (1984) International atomic energy agency, treatment of low- and intermediate-level liquid radioactive wastes. Technical Reports Series, **236**, IAEA, Vienna.

[3] T. Shin'ichi and A. Masayoshi, (2001) Development of database on the distribution coefficient. Preparation of Database, Nippon Genshiryoku Kenkyujo JAERI, Data, Code, **102(2)**.

[4] R. S. Lokhande, P. U. Singare, and A. B. Patil, (2007) Application of radioactive tracer technique on industrial grade ion exchange resins Indion-830 (Type-1) and Indion-N-IP (Type-2). Radiochim. Acta, **95(1)**, 111-114.

[5] R. S. Lokhande, P. U. Singare, and A. R. Kolte, (2007) Study on kinetics and mechanism of ion-isotopic exchange reaction using strongly basic anion exchange resins Duolite A-101 D and Duolite A-102 D. Radiochim. Acta, **95(10)**, 595-600.

[6] R. S. Lokhande, P. U. Singare, and P. Karthikeyan, (2007) The kinetics and mechanism of bromide ion isotope exchange reaction in strongly basic anion-exchange resin Duolite A-162 determined by the radioactive tracer technique. Russ. J. Phys. Chem., A, **81(11)**, 1768-1773.

[7] P. U. Singare, R. S. Lokhande, and A. B. Patil, (2008) Application of radioactive tracer technique for characterization of some strongly basic anion exchange resins, Radiochim. Acta, **96(2)**, 99-104.

[8] R. S. Lokhande, P. U. Singare, and T. S. Prabhavalkar, (2008) The application of the radioactive tracer technique to study the kinetics of bromide isotope exchange reaction with the participation of strongly basic anion exchange resin Indion FF-IP. Russ. J. Phys. Chem., A, **82(9)**, 1589-1595.

[9] S. Adachi, T. Mizuno, and R. Matsuno, (1995) Concentration dependence of the distribution coefficient of maltooligosaccharides on a cation-exchange resin. J. Chromatography A, **708(**2), 177-183.

[10] S. Adachi, T. Watanabe, and M. Kohashi (1989) Role of swelling pressure on the distribution coefficient of maltooligosaccharide in a cation-exchange resin, Agricultural and Biological Chemistry, **53(12)**, 3203-3208.

[11] A. Shuji, M. Takcshi, and M. Ryuichi, (1996) Temperature dependence of the distribution coefficient of maltooligosaccharides on cation-exchange resin in na^+ form. Bioscience, Biotechnology, and Biochemistry, **60(2)**, 338-340.

[12] S. Adachi and R. Matsuno, (1999) Apparent distribution coefficients of glucose and fructose to cation-exchange resins in some ionic forms. J Appl Glycosci, **46(1)**, 9-14.

[13] T. N. Van Der Walt and P. P. Coetzee, (1996) Distribution coefficients and ion exchange behaviour of some elements with Purolite S-950 in hydrochloric acid. Anal Bioanal Chem., **356(7)**, 420-424.

[14] F. W. E. Strelow, (1986) The influence of resin loading on cation exchange distribution coefficients of some elements in hydrochloric acid. Solvent Extraction and Ion Exchange, **4(6)**, 1193-1208.

[15] P. R. Sangurdekar, J. S. Melo, and S. F. D. Souza, (2005) Proceedings of Nuclear and Radiochemistry Symposium, Amritsar, India, 361.

[16] K. G. Heumann and K. Baier, (1982) Chloride distribution coefficient on strongly basic anion-exchange resin: Dependence on co-ion in alkali fluoride solutions. Chromatographia, **15(11)**, 701-703.

[17] D. D. Sood, A. V. R. Reddy, S. R. K. Iyer, S. Gangadharan, and G. Singh, (1998) Proceedings of international conference on applications of radioisotopes and radiation in industrial development. Ed. Mumbai, India, 47.

[18] R. S. Lokhande, P. U. Singare, and M. H. Dole (2006) Comparative study on bromide and iodide ion-isotopic exchange reactions using strongly basic anion exchange resin Duolite A-113. J. Nuclear and Radiochemical Sciences, **7(2)**, 29-32.

[19] R. S. Lokhande, P. U. Singare, and M. H. Dole, (2007) Application of radiotracer technique to study the ion iso-

tope exchange reactions using a strongly basic anion-exchange resin Duolite A-113. Radiochemistry, **49(5)**, 519-522.

[20] R. S. Lokhande and P. U. Singare, (2007) Comparative study on ion-isotopic exchange reaction kinetics by application of tracer technique, Radiochim. Acta, **95(3)**, 173-176.

[21] R. S. Lokhande and P. U. Singare, (2008) Comparative study on iodide and bromide ion-isotopic exchange reactions by application of radioactive tracer technique. J. Porous Mater, **15(3)**, 253-258.

[22] R. S. Lokhande, P. U. Singare, and V. V. Patil, (2008) Application of radioactive tracer technique to study the kinetics and mechanism of reversible ion-isotopic exchange reaction using strongly basic anion exchange resin Indion-850. Radiochemistry, **50(6)**, 638-641.

[23] R. S. Lokhande, P. U. Singare, and S. A. Parab, (2008) Application of radioactive tracer technique to study the kinetics of iodide ion- isotopic exchange reaction using strongly basic anion exchange resin Duolite A-116. Radiochemistry, **50(6)**, 642-644.

[24] R. S. Lokhande, P. U. Singare, and S. R. D. Tiwari, (2008) Study of bromide ion-isotopic exchange reaction kinetics using a weakly basic macro porous resin Indion-860. Radiochemistry, **50(6)**, 633-637.

[25] J. H. Suh and D. S. Kim, (2000) Comparison of different sorbents (inorganic and biological) for the removal of Pb^{2+} from aqueous solutions. J. Chem. Technol. Biotechnol., **75(4)**, 279-284.

[26] P. R. Sangurdekar, J. S. Melo, S. F. D. Souza, and D. P. Pimputkar, (2003) Proceedings of Nuclear and Radiochemistry Symposium, BARC, Mumbai, India, 545.

Vol.1, No.3, 195-203 (2009)
doi:10.4236/ns.2009.13026

Natural Science

A biomass gasification system for synthesis gas from the new method

Li-Qun Wang[1], Yu-Huan Dun[2], Heng Tang[3], Tong-Zhang Wang[3]

[1]Department of Energy and Power Engineering, Jiangsu University, Zhenjiang, China; thwlq2000@163.com
[2]Department of Energy and Power Engineering, Jiangsu University, Zhenjiang, China; dunyuhuan1985@126.com
[3]Department of Energy and Power Engineering, Jiangsu University, Zhenjiang, China

Received 27 June 2009; revised 20 July 2009; accepted 22 July 2009.

ABSTRACT

This paper describes a single fluidized bed by the two-step gasification of the working method, process and biomass and coal co-gasification by a certain proportion of the results of a typical run. The results show that the biomass gasification technology for raw materials has a wide adaptability, the tar content in the gas is less than 10mg/m^3,component in it ,the H_2+CO>70%, H_2/C ≈1~2,especially suitable for biomass from hydrogen, synthetic alcohol fuel, is a promising approach.

Keywords: Fuidized Bed; Double Bed; Biomass; Synthesis Gas; Co-Gasification; Steam Gasification

1. INTRODUCTION

In the growing depletion of traditional fossil fuel, mankind is facing increasing environmental pollution cases, countries around the world are actively developing renewable energy sources. And other types of biomass energy have unparalleled advantages, it can be stored and is the only low-carbon renewable energy, with lower sulfur and nitrogen, small environmental pollution and zero emissions of greenhouse gases, it is mature technology and can be made of the excellent transport liquid fuel alternative energy, automobile and caused consumers a wide range of great importance, as well as a major agricultural country, Brazil, the United States, Europe, China and other areas of the development of biomass energy in the walk in the world. At present, the production of bio-ethanol and bio-diesel used as a substitute for gasoline and diesel is a hot research and development, the process mainly through the use of bio-fermentation starch or sugar of biomass into ethanol.

Brazil, mainly use sugar cane as raw material, while the United States and China, with corn as the main raw material. With the development of biomass fuel and expansion, as well as international food prices, the international community to the best alternative to new energy sources of oil-bio-fuel ethanol opposition is growing. Causing people to question the professionals to reflect on the current bio-fuel ethanol production is the vast majority of food crops as raw materials, in the long run with the scale of restrictions and non-sustainability of lignocellulose raw materials to the second generation of bio-fuel ethanol is the future key to large-scale alternative to oil. The Chinese government approval in 2006 no longer agree the grain as raw materials to fuel ethanol production companies, shifting to second-generation bio-fuels research and development. The United States and the European Union has drawn up development plans, increase the second- generation bio-fuel ethanol technology, the pace of study. However, current technology development, fuel cellulosic ethanol technology in the pretreatment of raw materials and reduce the cost of a major breakthrough in enzyme takes time. U.S. Department of Energy is expected to cellulose ethanol fuel in 2012 may be about to get a major breakthrough, and a number of research institutions in Europe think that in 2015 to 2020. In addition to fuel ethanol, some companies have chosen to research and development of biomass gasification production of alcohol fuel, biodiesel, Fischer-Topsch synthesis of diesel and other key issues of technology, the application of reserves for the future technology, laying the foundation for the market to seize the future. The use of biomass gasification method to high-quality biomass into fuel, and bio-technology comparison with a broad range of sources of raw materials (agriculture, forestry, waste, garbage, etc.) into efficient, production intensity, and almost no waste, easy to mass production, the production process of the environmental impact of small, less greenhouse gas emissions. At present, biomass gasification system for synthesis gas from the basic approach is to use non-N_2 gasification agent or change the way the heating biomass pyrolysis and gasification, gas composition obtained for H_2, CO, CH_4 and CO_2, the specific methods of oxygen gasification, steam gasification and fluidized-bed gasification method dou-

ble. Gasification as a result of oxygen-free N_2 gas in the gas, a higher calorific value gas, the CO, H_2 with a high level, CH_4 low, due to oxygen gasification free to adjust the reaction temperature, the reaction completely and higher gas production, gasification higher efficiency, the technology is mature, simple, stable operation and suitable for large- scale production, as a result of oxygen equipment, investment and operating costs are higher, it is difficult to adapt to storage and transportation of biomass resources, the high cost of dispersed and difficult to mass production characteristics. The water vapor is a strong endothermic reaction gasification, biomass pyrolysis and gasification temperature above 800℃ need to have a higher reaction rate, it is generally difficult to achieve this temperature steam requirements, so less gas production, gasification and low efficiency. The advantage is to form H_2, CH_4 more, CO_2,CO and other content in a relatively small amount of synthesis gas in favor of simplifying the follow-up process. The using of steam gasification process in the world is very few, mainly used in laboratory research. The last century 80's, Professor Kunii, D. first dual fluidized bed gasification technology methods [1-3]. Packages are equipped with a

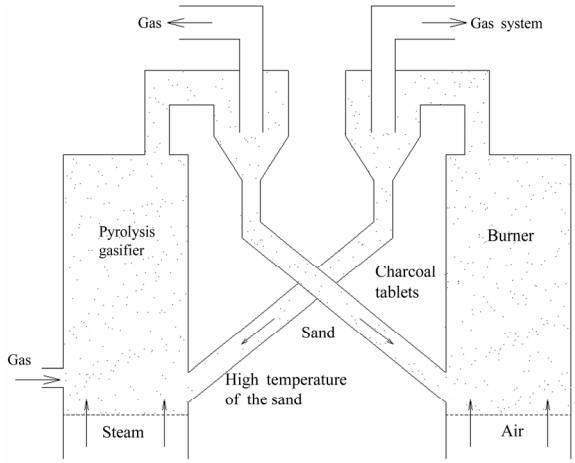

Figure 1. The gasifier of two fluidized beds of biomass.

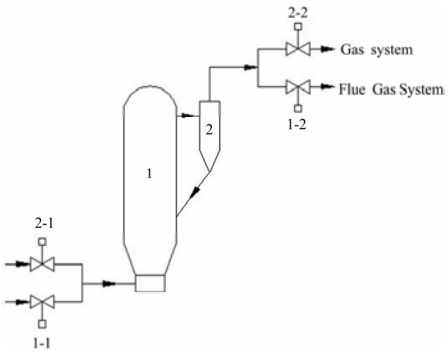

Figure 2. Single fluidized bed gasification two-step working principle, 1-1 Air control valve, 1-2 Flue control valve, 2-1 Steam Control Valve, 2-2 Gas Control Valve.

fluidized bed gasifier and the composition of fluidized bed combustion furnace (**Figure 1**). Burner for heating air combustion of coke particles in the gasifier heating inert particles, while for the steam gasifier and high temperature so that biomass particles in the flow of inert state pyrolysis reaction occurs to produce hydrogen-rich synthesis gas. This method does not require external heat source, and therefore do not require oxygen equipment and low cost operation. However, due to the volume and temperature of heat carrier restrictions, not more than gasifier temperature of 800℃, resulted in lower gasification efficiency, on the other hand, un-time as a result of coke and the heat carrier are at a high temperature cycle, it is difficult to quantitatively control, temperature easy to change, it is difficult to stable operation, restrictions on use of the fact that, at present there is no practical case of industrialization. Professor Wang Tongzhang, Jiangsu University, at the conclusion of the research team based on previous experience, in 1990 put forward a single fluidized bed by two-step gasification method. Synthesis gas was prepared with steam gasification agent. And obtained a patent in China [4,5]. Principle of the work of this process known as fluidized-bed water gas gasifier (FWG). The equipment with coal as raw materials has industrialized. With biomass as raw material the equipment being promoted in this paper technological processes of the gasification process, the scope of application and the moving results are introduced.

2. A SINGLE FLUIDIZED BED TWO-STEP GASIFICATION PROCESS AND DEVICE [6]

Water vapor and carbon for the gasification agent of raw materials to form H_2, CO, CH_4 and CO_2, the main reaction is:

$$C + H_2O \rightarrow CO + H_2 \quad -162.3\ MJ \quad (1)$$

$$C + 2H_2O \rightarrow CO_2 + 2H_2 \quad -75.2\ MJ \quad (2)$$

$$CO + H_2O \rightarrow CO_2 + H_2 \quad -43.56\ MJ \quad (3)$$

$$C + 2H_2 \rightarrow CH_4 \quad +87.36\ MJ \quad (4)$$

$$C + O_2 \rightarrow CO_2 \quad +408.86\ MJ \quad (5)$$

Endothermic reaction is basically, in order to enable the reaction can be carried out, it is necessary to provide the necessary reaction heat. To this end will be in the same fluidized bed biomass gasification process is divided into two processes: First, the combustion process (the heating process); First, the process of pyrolysis and gasification. To the gasifier for combustion into the air and raw materials, so that flow of raw materials in a state of combustion heat release style (5), so that the material layer gasifier rapid increase in temperature is expected when the temperature rise to the scheduled (scheduled for 1000℃), to stop for air, the end of the combustion process; gasifier turn to pyrolysis and gasification proc-

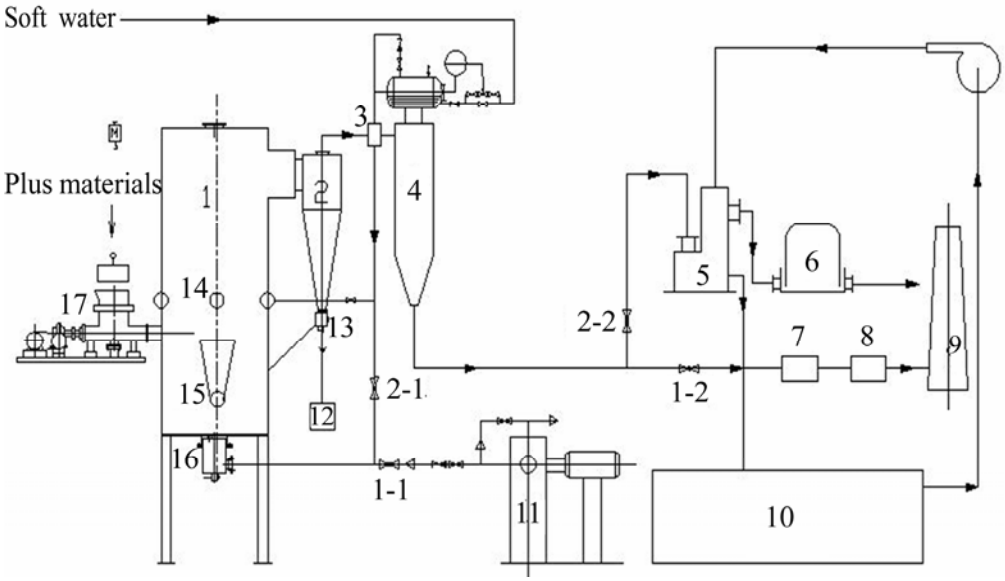

1 Fluidized bed biomass gasifier, 2 High-temperature cyclone, 3 Superheater, 4 Waste heat boile, 5 Scrubber, 6 Bell type gasholder, 7 Air preheater, 8 Precipitator(dust collector), 9 Chimney, 10 Setting pond, 11 Roots blower, 12 Reserve gray box, 13 Feed back, 14 Air, steam nozzle, 15 Spiral feeding machine with biomass bunker, 16 Wind Room, 17 Spiral feeding machine with coal bunker.

Figure 3. The process flow of the water gas gasifier of fluidized bed of biomass.

ess, into the steam for the gasifier and biomass to biomass and the original high-temperature materials in the water vapor layer of the under the conditions in the flow of pyrolysis and gasification reaction occurred, resulting in the synthesis of H_2-rich gas, because the process is endothermic reaction, the rapid temperature decline in bed when the bed temperature dropped to predetermined temperature (scheduled for the 900℃), gasification process is over. The gasifier gets into the combustion process. The two processes repeated conversion to achieve the production of synthesis gas purpose. Two processes in the fluidized bed gasifier through imports and exports of two pairs of control valves: air control valve 1-1, vapor control valves 2-1 and Flue control valves 1-2, gas control valves 2-2 to achieve (see **Figure 2**) flue and gas, respectively, into the flue system and gas system, the gate valve by the furnace temperature control.

Figure 3 Biomass fluidized bed water gas gasifier (BFWG) process. Fluidized bed biomass gasifier (1) with two feeders, screw feeder biomass (15) and coal screw feeder (17) for the conduct of the total biomass and coal gasification, gasifier start when run-time, water vapor control valve 2-1 and gas control valve 2-2 to close,air control valve 1-1 and flue control valve 1-2 open when the combustion channels in working condition, when Roots blower (11) through the air control valve 1-1 at the bottom of the wind from the gasifier chamber (16) for the first time into the air, at the same time coal screw machine (17) adding coal to the furnace (0~6mm), to enable complete combustion of fuel in the heater do, in the furnace equipped with a secondary air nozzle (14), secondary air jet from the nozzle to increase, so that paragraph into the suspension of particles of incomplete combustion of carbon and the gas composition to continue to burn, so that the furnace temperature the rapid increase in high-temperature combustion gas from the gasifier cyclone export to high temperatures, (2) after the beginning of dust into the superheater (3) and waste heat boiler (4) heat exchanger, the flue gas temperature to about 400℃ below the flue control valve 1-2 to enter the air preheater (7), flue gas temperature to 200℃ the following into the dust collector (8), purified by the chimney (9) into the atmosphere. Under the high temperature cyclone separation carbon dust by the return feeder (13) returns to re-combustion gasification gasifier. When the furnace temperature up to set temperature (1000℃), the end of the combustion process, when the air control valves, flue control valves 1-1 and 1-2 followed by self-closing, steam control valve2-1 and gas control valve 2-2 automatically open one after another, from the waste heat boiler (4) water vapor generated by the steam superheater (3), the steam control valve 2-1 by the wind Room (16) into the gasifier, while biomass feeder (15) to adding biomass furnace (0~10mm), then high-temperature material layer and adding biomass state in the flow of pyrolysis and gasification reaction occurred, resulting in hydrogen-rich gas. Since the reaction is endothermic reaction, the furnace temperature dropped quickly when the high temperature gas generated by cyclone (2) after the separation of carbon dust by

the return under the feeder (13) into the re-gasification furnace, after the separation of crude gas into the waste heat boiler (4) for heat exchange cooling to below 400 ℃,the gas control valves, 2-2 to enter the scrubber tower (5),by the washing water after the cooling device into the gas cabinet (6),for users. When the furnace temperature down to set temperature(900℃),the gasification process, steam control valves 2-1 and gas control valve 2-2 automatically shut down one after another, the air control valves1-1andflue control valves 1-2 followed by open, into the gasifier and the combustion process, alternating back and forth these two processes to work, production of the H_2-rich syngas. Since the fluidized bed gasifier with a uniform temperature characteristic, temperature control in bed for two processes is not only conducive to the stability of production quality, and temperature can be arbitrary in order to obtain the synthesis gas components of satisfaction. General low-temperature limit determined by the reaction rate of raw materials, high temperature limit determined by the ash melting point of raw materials. Two waste heat recovery processes can be generated by steam gasification to meet their own needs.

3. BIOMASS FLUIDIZED BED WATER GASIFIER IS RUNNING RESULTS AND ANALYSIS

Biomass feedstock to 0~10mm smash into the furnace, due to the shape of biomass particles of diversity, so that net flow of biomass is more difficult biomass powder usually include a certain amount of inert particles such as sand, to improve the Health the flow of material performance, as a result of China's coal-dominated energy structure, the authors selected coal (0~6mm) in place of the inert particles, such coal to improve the flow of not only played the role of performance, because coal is a hot body, together with the biomass total gasification, coal and biomass in the physical and chemical properties of many complementary aspects, such as the coal density high, fixed carbon content high, ash melting point high, chemical activity low; and biomass density low, fixed carbon contentlow, ash melting point low, high volatile, highchemical activity and easy to gasification, gasification of the two were complementary to each other will receive such good results. Therefore this section will be a comprehensive discussion of this technology to coal, biomass gasification and the two kinds of co-gasication were the result of the operation [6].

3.1. The Operation of Coal as Raw Materials Results

Table 1 shows the results of the operation in the type FWG 1.6 gasifier.

The three kinds of coal in the long-term continuous operation, results showed that regardless of coal for the weak or strong adhesive bonding of all long-term stable operation and good results. The strong bond not only of coal coking phenomenon did not happen, and gas indicators are generally better than the weak bonding of coal, mainly air and water vapor at 950℃ and above the turn of coal particles for combustion and gasification reactions, so that caking coal rapid destruction of the gluey layer, the strong bond of coal can be a smooth operation. Fluidized bed water gas gasifier is automatically adjustable, the results in Table 1 is a coal gasification process of running the results can be seen from the gas composition, gas composition in the H_2 high,CH_4 content is generally 5~7%. The CO content of less than 20%,which is due to the process of coal gasification, when there are complex reaction mechanism, when the water vapor and carbon bed water-gas reaction to produce high gas mixtures containing H_2, has just joined the Fan coal in such a high temperature pyrolysis atmosphere makes reaction CH_4 and H_2 gas in a marked increase in the content, and some scholars believe that the main CH_4 from the hydrogenation reaction (4).

Table 2. Different ways of coal feeding have an effect on gas composition. Coal feeding in different ways, from changing in gas composition obviously. In the process of coal gasification, coal is fed, the component of the H_2 and CH_4 in the gas increased obviously, while reducing CO, for high volatile coal, the greater difference. This factor is a gasifier to provide a more convenient, that is, through different ways to increase coal output is suitable for the requirements of different gas components.

3.2. Biomass as Raw Materials Moving Results

Water fluidized bed biomass gasifier (BFWG) set up two feeders: biomass and coal screw feeders. Generally the gasifier was fed with biomass powder(0-10mm) in the gasification process(0~10mm), coal combustion process by adding(0~6mm), this study used corncob, rice husk, wood chips as raw material, high in the inner diameter 300×4000mm bed water-gas gasifier in operation results (**Table 3**).

3.3. Discussion and Analysis of the Results

From the corn cob, sawdust, rice husk three experiments show that the agricultural and forestry waste (**Table 4**), The diversity of the types of biomass does not affect the performance of their gasification, the gas composition, calorific value, the efficiency of gasification, tar and other parameters in the same operating conditions, the results were similar. The results from **Table 5** show that the impact of gasification temperature gasification gas production rate and efficiency of key parameters, (the technology can easily adjust the parameters), with the increase in transition temperature, gas production rate and a corresponding increase in efficiency gasification,

Table 1. The results of three coal.

Item / The type of coal	Lean coal	Coke	Semi-anthracite
Industry Analysis wt%			
Total Moisture	8.11	7.8	3.37
Inherent moisture	0.8	0.42	0.77
Fixed carbon	65.37	53.94	56.42
Volatile	13.66	14.53	18.62
Ash	12.86	23.67	21.24
Sulfur content	0.32	0.3	0.35
Calorific value of coal KJ/Kg	25103	23268	23040
Characteristics of coke residue	3	6	4
Roca Index	Non-bonded	75	Weak bond
Ash melting point（℃）			
Deformation temperature	1470	＞1400	＞1200
Softening temperature	1500	＞1400	＞1200
Operating Temperature	950~1000	950~1000	950~1000
Gas composition vol%			
CO_2	10.6	8.4	9.4
CO	15.3	19.5	19.4
H_2	61.12	59.5	58.81
CH_4	6.83	6.9	6.92
O_2	0.3	0.1	0.14
N_2	5.58	5.7	5.63
$H_2S(mg/m^3)$	120	120	120
tar content（mg/m^3）	3.3	3.3	3.3
Gas calorific value（KJ/m^3）	11201	11453	11227
Water gas production rate（m^3/Kg）	1.2	1.2	1.19
Gasification efficiency （%）	52	59	58
Thermal efficiency（%）	85	85	85

Table 2. Gas components under different coal feed ways.

Operation Mode	Gas composition						Calorific value（KJ/m^3）
	CO_2	O_2	CO	CH_4	H_2	N_2	
Combustion process feed coal	17.5	0.3	17.9	2.06	58.13	4.11	9207
Gasification process feed coal	10.6	0.3	15.3	6.83	61.12	10.12	10120

Table 3. The industrial materials analysis and elemental analysis of the materials.

Types of raw materials	Industry Analysis/%				Elemental analysis/%				Calorific value
	M_t	A_{ar}	V_{ar}	FC_{ar}	C_{ar}	H_{ar}	N_{ar}	O_{ar}	Q KJ/Kg
Corncob	5.6	6.24	76.92	11.24	47.63	4.91	0.85	46.61	17245
Sawdust	13.44	1.42	75.91	9.23	46.18	6.28	0.14	47.4	15672
Rice husk	7.4	11.01	73.78	7.81	45.13	5.04	0.76	49.07	14557
Test Coal	4.7	26.5	7.94	60.86	62.31	2.86	1.02	1.9	23120

Table 4. Moving results of biomass.

Item	Corncob	Sawdust	Rice husk
The amount of biomass kg/h	140	140	140
The amount of coal kg/h	35	35	35
Biomass/Coal	4/1	4/1	4/1
Air for combustion stage	270	270	270
For the amount of water vapor gasification stage kg/h	110	110	110
Steam/Biomass (S/B)	0.79	0.79	0.79
Operating temperature range ℃	900-950	900-950	900-950
Gas composition（Vol %）			
H_2	38.87	37.78	38.6
CO	32.29	30.23	32.70
CH_4	11.62	9.43	7.73
CO_2	13.7	14.88	13.41
O_2	0.2	0.8	0.4
N_2	7.32	6.88	7.7
Gas calorific value KJ/m^3	12579	11766.3	11496.24
content of tar oil mg/m^3	＜10mg	＜10mg	＜10mg
Gas production rate m^3/kg daf	1.15	1.17	1.1
Gasification efficiency %	84	88	86.80
The thermal efficiency of gasifier %	85	85	85
Gasification intensity kg/(m^2 h)		3000	

Table 5. Corncob interval at different temperatures of the test results.

Item	Temperature range（℃）		
	850－900	900－950	950－1000
The amount of biomass kg/h	120	120	120
The amount of coal kg/h	30	30	30
Biomass/Coal	4/1	4/1	4/1
Air for combustion stage m^3/h	286	286	286
For the amount of water vapor gasification stage kg/h	108	108	108
Steam/Biomass（S/B）	0.9	0.9	0.9
Gas composition（Vol %）			
H_2	28.70	38.30	46.30
CO	26.10	29.40	28.30
CH_4	19.7	11.20	8.40
CO_2	18.20	13.70	10.50
O_2	0.4	0.2	0.4
N_2	6.0	7.20	6.1
content of tar oil mg/m^3	1.20	0.9	0.7
Gas production rate m^3/kg daf	1.00	1.20	1.25
Gas calorific value KJ/m^3	14315	12414	12043
Gasification efficiency ％	83	86.4	87.3

Table 6. The current production methods of medium-heating value compared with the technique.

Item	Methods	Steam gasification	Oxygen gasification	Dual fluidized bed gasification	Two-step gasification method
Gasification conditions	Gasification medium	Steam	O_2	Steam	Steam
	Gasification temperature /℃	550~750	850~950	600~800	900~1000
	The main auxiliary equipment	Steam generator	Oxygen generator	Waste heat recovery unit	Waste heat recovery unit
	Gasifier type	Fluidized bed	Fluidized bed	Fluidized bed	Fluidized bed
	Gasification efficiency /%	~55	80	65	85
	Gasification yield /m³/kg	~0.46	1.0	~0.55	~1.1
	Gasification calorific value /MJ/m³	20	13.0	16	14
	Gasification intensity /kg/(m³·h)	1000	3000	1500	3000
Gas composition	CO_2	24.0	28.0	15.0	15.0
	CO	27.0	30.0	44.0	30.0
	CH_4	20.0	13.0	16.0	10.0
	C_nH_m	8.0	4.0	5.5	
	H_2	20.0	25.0	18.0	40
	N_2	1.0	2.0	1.0	5.0
	O_2	0.3	0.5	0.5	0.4
Technical and economic evaluation	Technical difficulty	General	General	Higher	General
	Stability	General	Better	Poor	Better
	One-time investment	General	Higher	Higher	General
	Running costs	General	Higher	Lower	Low
	Content of tar oil	More	Less	More	Trace
	Application of	Little	More	Less	Application

Table 7. 10,000 tons / year to estimate the scale of investment in manufacturing plant (equipment).

Serial number	Item	Total（Million）
1	Part of biomass gasification（prepare feed、Gasifier、Purification Storage cabinets,Counter to the gas purification）	1000
2	Fine desulfurization 、Dechlorination	95
3	Compression Section	130
4	Synthesis of dimethyl ether	210
5	Distillation of dimethyl ether	50
6	Electrical instrumentation	130
7	Other	100
Total		1715

and gas heat values increase with the transition temperature decreased. H_2 is mainly expressed in the increase as the temperature increases, and decreases due to CH4. S/B is the impact of gas composition, gas yield and gas calorific value of the important parameters in **Figure 4** that the gas temperature of 900-950℃, corn cob/coal ratio of 4/1,gas H_2,CH_4,CO content and S/B relationship. As well as gas production rate and the S/B relationship (**Figure 5**), gas heat value and the S/B relationship. (**Figure 6**).

Table 8. Estimates of consumption of fixed costs (per ton of DME).

Serial number	Name	Units	Amount	Units（yuan）	Amount（yuan）
1	Straw	t	4.4	200	880
2	Coal	t	1	400	400
3	Electricity	Kwh	600	0.5	300
4	Water	t	300	0.2	60
5	Steam	t	1.5	60	90
6	Catalyst	Kg	2.5	40	100
7	Subtotal				1830
8	Other				500
9	Cost of sales	t			2330

As can be seen from the chart, in the experimental conditions, the gas content in H_2 increases with the S/B increasing, and CH_4, CO content both reduces with the S/B increasing.

4. CONCLUSION AND OUTLOOK

4.1. Conclusion

Fluidized bed biomass gasifier water and put into service, after a long-term operation test, indicating that the stability of the furnace is running, convenient operation, stable performance. In this paper, biomass and coal ratio under different experimental results show the feasibility of gasification technology and economic advantages (**Table 6**). The results from the pilot to see in biomass synthesis gas preparation methods, this technology has the following characteristics.

1) Applies to a wide range of raw materials: agricultural and forestry waste and organic solid waste can be used effectively. Biomass as a result of agriculture, forestry, raw material suppliers subject to seasonal changes, can be adjusted to ensure that the coal to security of energy supplies.

2) This technology is particularly applicable to a total of coal and biomass gasification. A result of coal in the combustion process can be quickly obtained by adding the necessary high-temperature gasification process and heat conditions. So the process of biomass gasification

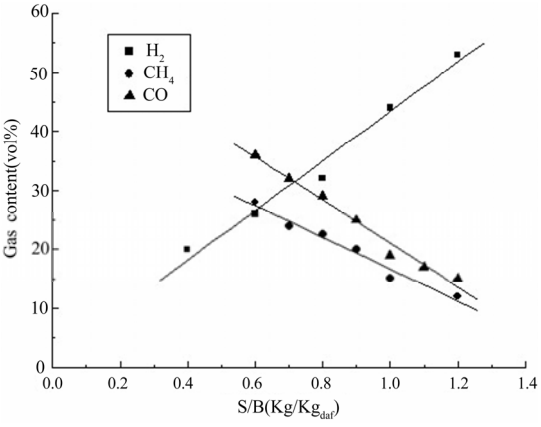

Figure 4. The influence to the H_2, CH_4 and CO percents of the product gas by the value of S/B.

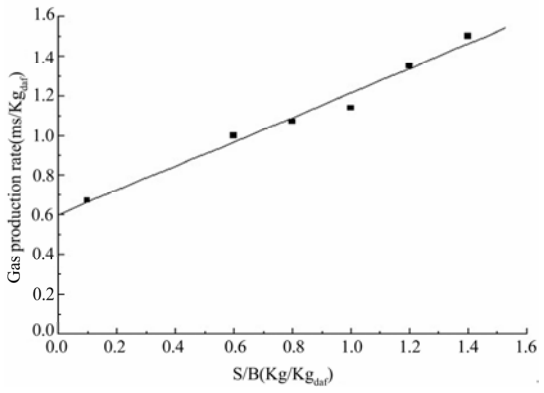

Figure 5. The influence to the yield of the product gas by the value of S/B.

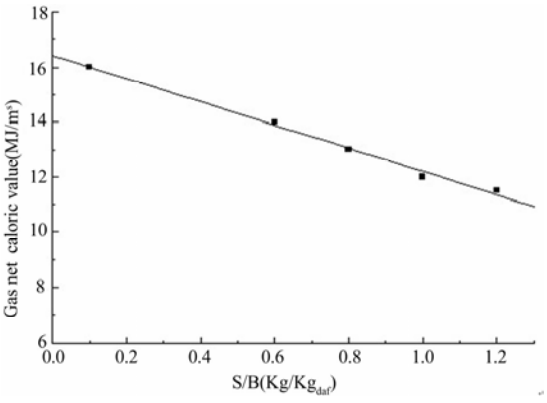

Figure 6. The influence to the heat value of the product gas by the value of S/B.

has been transformed into efficient. Due to high temperature, the role of water vapor in the gas under very low tar content, so easy to deal with gas purification, resolved biomass gasification gas with high tar problems.

3) High levels of H_2 gas, H_2 + CO>70%, H/CO = 1~2, is a synthetic alcohol fuel components suitable for the synthesis of alcohol fuel, the preparation of H_2 technology to provide a viable route.

4.2. Outlook

The development and utilization of oil alternatives and renewable sources of energy is the world's largest energy development trends and hot, renewable energy, the biological resources into liquid fuels to replace oil with other types of energy unparalleled advantage. At present, many countries in the corn to sugar cane as raw material, through the biological alternative fuel ethanol into gasoline has been noticed, as the existing technology of powdered sugar to starch-based, people struggle with food concerns, has been transferred to wood cellulose as raw materials on behalf of the Section 2 the development of biomass fuels. Due to technical and economic reasons, the second generation of fuel ethanol industry takes time. Even cellulose as raw materials process technology, the future level of industrialization can be achieved. Due to the diversity of straw cellulose, in the production process we also need to deal with the residue. In this paper, the biomass gasification technology is more perfect to deal with these types of materials technology. Biological ferment and gasification methods both integrated development, to make the development and utilization of biomass energy achieve better results. Technology is now under the operation of indicators, the production of 1 ton each of dimethyl ether (DME), the need for 4.4 tons of straw and 1 ton of coal. China based on the current market price, 200 yuan per ton of straw,400 yuan per ton coal, it is estimated the technology ton DME production plant of economic indicators. (**Table 7**, **Table 8**)

Taking into account the cost of capital, a total investment of about 3000 million, at current market price of DME 5,000 yuan per ton, production of 1~2 years to recover their investment. The technology of biomass for hydrogen production, due to purification, separation technologies are mature technologies [7-9], 1 kg of hydrogen to be consumed 12kg of straw plus 3kg of coal. renewable energy technology in the economic advantage. As a result of this two-step technique, in the production process, about half the time the combustion process will be used to provide heat for the gasification process, the line considerable. The calorific value of hydrogen is the fuel units 3 times, which can be seen the application of The resulting hydrogen can be projected cost per ton of about 4,000~5,000 yuan. This is the current cost of gaso same-size models of fluidized-bed gasifier for gasification than oxygen for gasification agent law, and its production capacity will be less 1/2. However, due to the biomass distribution of a wide set shipped difficulties and is not suitable for large-scale production. This small-scale production plant, built near the highway to the highway for the trunk to form a supply network, so that raw materials can be extensive and products combine the mobility of, do the local sales of local production.

A wide range of biomass distribution of a large amount of earth each year, the total biomass (dry) of about 1400-1800 billion tons, equivalent to the annual world energy consumption 10 times the biomass wish for the adoption of this technology to do economic development of mankind a contribution.

REFERENCES

[1] J. corella, J. M .Toledo, and G. Molina, (2007) A review on dual fluidized-bed biomass gasifiers. [J] Ind. Eng .Chem .Res., **46**, 6831-6839.

[2] J. corella, J. M. Toledo, and G. Molina, (2008) Biomass gasification with pure steam in fluidized bed. [J] Int, J. Oil., Gas and coal Technology, **1(1/2)**.

[3] C. Z. Wu, B. Y. Xu, Z. F. Luo, *et al*. (1995) Analysis of biomass gasification for MHV fuel gas. [J]. Coal Gas and Heating Power, **15(2)**, 8-14.

[4] T. Z. Wang, L. Q. Wang, and H. S. Zhou, A king of biomass and coal co-gasification method and derice of the fluidized bed, **4**, CN200410013943.

[5] T. Z. Wang and L. Q. Wang, A kind of water gas gasification method and device, ZL90105680.

[6] L. Q. Wang, X. Song, H. S. Zhou, *et al*. (2008) Development study on co-gasification of biomass and coal in fluidized bed gasifier. (II)[J] Acta Energiae Solaris Sinica, **29(3)**, 354-359.

[7] D. L. Xie, G. Y. Yi, Z. W. Li, W. Y. Qiao, (2007) Selection of fluidzed bed technology for hydrogen production from biomass gasification. [J] Sino-global Energy. **12**, 20-24.

[8] S. T. Turn, Z. Zhang, *et al*. (1998) An experiment investigation of hydrogen production from bimass gasification. [J] Int. J. Hydrogen Energy., **23(8)**, 641-648.

[9] X. Y. Su, Z. W. Wang, C. M. Cheng, *et al*. (2000) Study on biomass pyrolysis and gasification in a fluidized bed. [J] Jounal of Fuel Chemistry and Technology, **28(4)**, 298-305.

Vol.1, No.3, 204-209 (2009) **Natural Science**
doi:10.4236/ns.2009.13027

Wavelet chaotic neural networks and their application to continuous function optimization

Jia-Hai Zhang[1], Yao-Qun Xu[2]

[1]College of Electrical and Automatic Engineering, Sanjing University, Nanjing, China; zhangjh6688@sohu.com
[2]Institute of Computer and Information Engineering Harbin Commercial University, Harbin, China; xuyaoq@hrbcu.edu.cn

Received 7 September 2009; revised 10 October 2009; accepted 12 October 2009.

ABSTRACT

Neural networks have been shown to be powerful tools for solving optimization problems. In this paper, we first retrospect Chen's chaotic neural network and then propose several novel chaotic neural networks. Second, we plot the figures of the state bifurcation and the time evolution of most positive Lyapunov exponent. Third, we apply all of them to search global minima of continuous functions, and respectively plot their time evolution figures of most positive Lyapunov exponent and energy function. At last, we make an analysis of the performance of these chaotic neural networks.

Keywords: Wavelet Chaotic Neural Networks; Wavelet; Optimization

1. INTRODUCTION

Hopfield and Tank first applied the continuous-time, continuous-output Hopfield neural network (HNN) to solve TSP [1], thereby initiating a new approach to optimization problems [2,3]. The Hopfield neural network, one of the well-known models of this type, converges to a stable equilibrium point due to its gradient decent dynamics; however, it causes sever local-minimum problems whenever it is applied to optimization problems. M-SCNN has been proved to be more power than Chen's chaotic neural network in solving optimization problems, especially in searching global minima of continuous function and traveling salesman problems [4].

In this paper, we first review the Chen's chaotic neural network. Second, we propose several novel chaotic neural networks. Third, we plot the figures of the state bifurcation and the time evolution of most positive Lyapunov exponent. Fourth, we apply all of them to search global minima of continuous functions, and respectively plot their time evolution figures of most positive Lyapunov exponent and energy function. At last, simulation results are summarized in a Table in order to make an analysis of their performance.

2. CHAOTIC NEURAL NETWORK MODELS

In this section, several chaotic neural networks are given. And the first is proposed by Chen, the rest proposed by ourselves.

2.1. Chen's Chaotic Neural Network

Chen and Aihara's transiently chaotic neural network [5] is described as follows:

$$x_i(t) = f(y_i(t)) = \frac{1}{1+e^{-y_i(t)/\varepsilon}} \quad (1)$$

$$y_i(t+1) = ky_i(t) + \alpha\left[\sum_j W_{ij}x_j + I_i\right] - z_i(t)(x_i(t) - I_0) \quad (2)$$

$$z_i(t+1) = (1-\beta)z_i(t) \quad (3)$$

where $x_i(t)$ is output of neuron i; $y_i(t)$ denotes internal state of neuron i; W_{ij} describes connection weight from neuron j to neuron i, $W_{ij} = W_{ji}$; I_i is input bias of neuron i, a a positive scaling parameter for neural inputs, k damping factor of nerve membrane, $0 \le k \le 1$, $z_i(t)$ self-feedback connection weight (refractory strength) ≥ 0, β damping factor of $z_i(t)$, $0 < \beta < 1$, I_0 a positive parameter, ε steepness parameter of the output function, $\varepsilon > 0$.

2.2. Morlet Wavelet Chaotic Neural Network (MWCNN)

Morlet wavelet chaotic neural network is described as follows:

$$x_i(t) = f(y_i(t)) = e^{-(uy_i(t))^2/2}\cos(5uy_i(t)) \quad (4)$$

$$y_i(t+1) = ky_i(t) + \alpha\left[\sum_j W_{ij}x_j + I_i\right] - z_i(t)(x_i(t) - I_0) \quad (5)$$

$$z_i(t+1) = (1-\beta)z_i(t) \quad (6)$$

where $x_i(t)$, $y_i(t)$, W_{ij}, α, k, I_i, $z_i(t)$, I_0 are the same with the above. And the **Eq.4** is the Morlet wavelet function. u is a steepness parameter of the output function which is varied with different optimization problems.

2.3. Mexican Hat Wavelet Chaotic Neural Network (MHWCNN)

Mexican hat wavelet chaotic neural network is described as follows:

$$x_i(t) = f(y_i(t)) = \frac{2}{\sqrt{3\sqrt{\pi}}}(1-(uy_i(t))^2)e^{-(uy_i(t))^2/2} \quad (7)$$

$$y_i(t+1) = ky_i(t) + \alpha\left[\sum_j W_{ij}x_j + I_i\right] - z_i(t)(x_i(t) - I_0) \quad (8)$$

$$z_i(t+1) = (1-\beta)z_i(t) \quad (9)$$

where $x_i(t)$, $y_i(t)$, W_{ij}, α, k, I_i, $z_i(t)$, I_0, u are the same with the above. And the **Eq.7** is the Shannon wavelet function.

3. RESEARCH ON CONTINUOUS FUNCTION PROBLEMS

In this section, we apply all the above chaotic neural networks to search global minima of the following three continuous functions.

The three continuous functions are described as follows [6]:

$$f_1(x_1, x_2) = \frac{\sin^2\sqrt{x_1^2 + x_2^2} - 0.5}{[1+0.001(x_1^2 + x_2^2)]^2} - 0.5 \quad |x_i| \le 100 \quad (10)$$

$$f_2(x_1, x_2) = 4x_1^2 - 2.1x_1^4 + x_1^6/3 + x_1x_2 - 4x_2^2 + 4x_2^4 \quad |x_i| \le 5 \quad (11)$$

$$f_4(x_1, x_2) = (x - \frac{5.1}{4\pi^2}x_1^2 + \frac{5}{\pi}x_1 - 6)^2 + 10(1-\frac{1}{8\pi})\cos x_1 + 10$$
$$-5 \le x_1 \le 10, 0 \le x_2 \le 15 \quad (12)$$

The minimum value of **Eq.10**, **11**, **12** respectively are -1, -1.0316285, 0, 0.398 and its responding point are (0, 0), (0.08983, -0.7126) or (-0.08983, 0.7126), (-3.142, 2.275) or (3.142, 2.275) or (9.425, 2.425).

In order to make comparison conveniently, we set some parameters such as the annealing speed β, the self-feedback $z(0,0)$ and the initial value of internal state $y(0,0)$ as follows: β =0.002, $z(0,0)$ =[0.8, 0.8], $y(0,0)$ =[0.283, 0.283]. Meanwhile, we set the iteration as large as 5000 so as to get stable state of a global minimum.

3.1. Chen's Chaotic Neural Network

1) Simulation on the First Continuous Function

The rest parameters are set as follows:

$$k=1, \alpha=0.5, \varepsilon=1/10, I_0=0.85.$$

The time evolution figures of the biggest positive Lyapunov exponent and energy function of Chen's in solving the first continuous function are shown as **Figure 1, Figure 2.**

The global minimum and its responding point of the simulation are respectively -0.99989 and (0.0073653, 0.0073653).

2) Simulation on the Second Continuous Function

The rest parameters are set as follows:

$$k=1, \alpha=0.02, \varepsilon=1/20, I_0=0.85.$$

The time evolution figures of most positive Lyapunov exponent and energy function of Chen's in

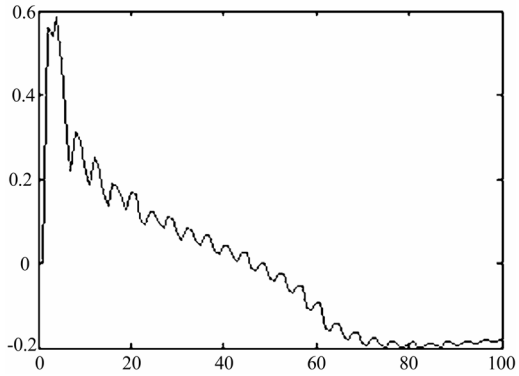

Figure 1. Time evolution figure of Lyapunov exponent.

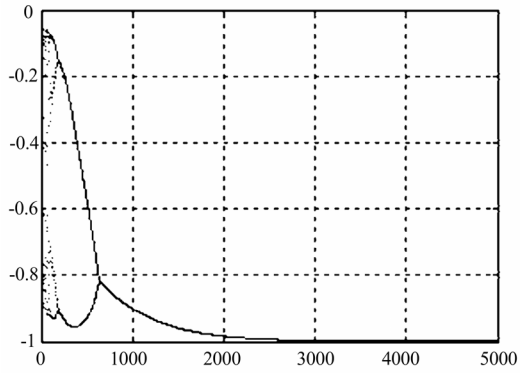

Figure 2. Time evolution figure of energy function.

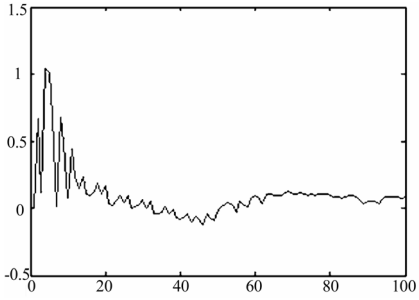

Figure 3. Time evolution figure of Lyapunov exponent.

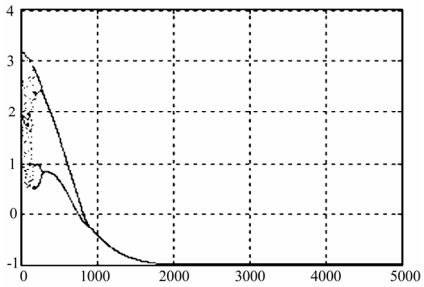

Figure 4. Time evolution figure of energy function.

solving the first continuous function are shown as **Figure 3**, **Figure 4**.

The global minimum and its responding point of the simulation are respectively -1 and (0, 0.70712).

3) Simulation on the Third Continuous Function

The rest parameters are set as follows:

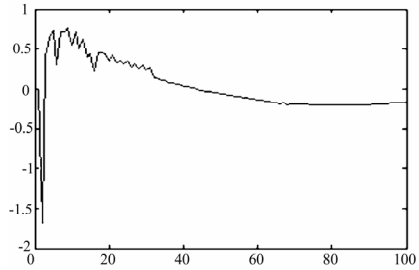

Figure 5. Time evolution figure of Lyapunov exponent.

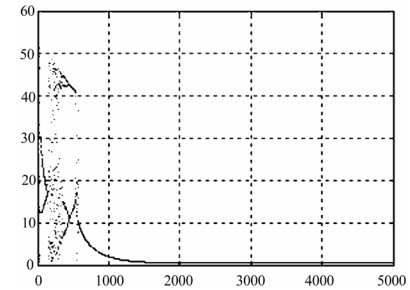

Figure 6. Time evolution figure of energy function.

$$k=1, \alpha=0.2, \varepsilon=1, I_0=0.5.$$

The time evolution figures of most positive Lyapunov exponent and energy function of Chen's in solving the first continuous function are shown as **Figure 5**, **Figure 6.**

The global minimum and its responding point of the simulation are respectively 0.39789 and (9.4246, 2.4747).

3.2. Morlet Wavelet Chaotic Neural Network (Mwcnn)

1) Simulation on the First Continuous Function

The rest parameters are set as follows:

$$k=1, \alpha=0.5, u=0.5, I_0=0.65.$$

The time evolution figures of most positive Lyapunov exponent and energy function of MWCNN in solving the first continuous function are shown as **Figure 7, Figure 8.**

The global minimum and its responding point of the simulation are respectively -0.99997 and (0.0038638, 0.0038638).

2) Simulation on the Second Continuous Function

The rest parameters are set as follows:

$$k=1, \alpha=0.05, u=0.7, I_0=0.2.$$

The time evolution figures of most positive Lyapunov exponent and energy function of MWCNN in solving the first continuous function are shown as **Figure 9**, **Figure 10.**

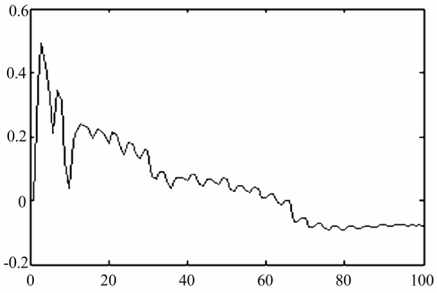

Figure 7. Time evolution figure of Lyapunov exponent.

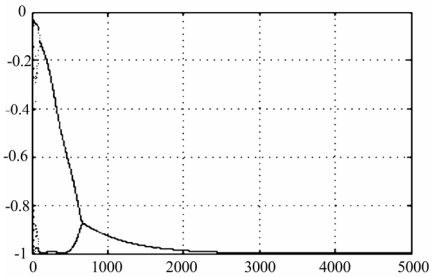

Figure 8. Time evolution figure of energy function.

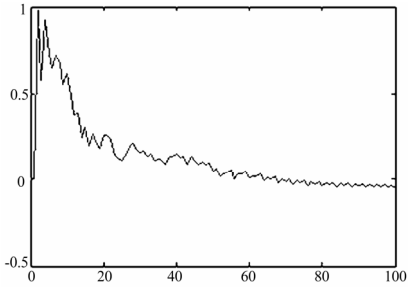

Figure 9. Time evolution figure of Lyapunov exponent.

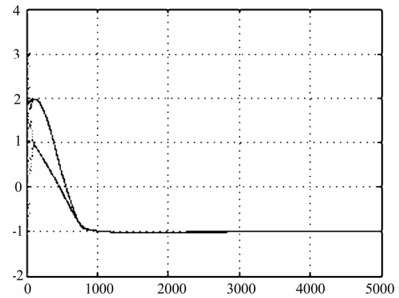

Figure 10. Time evolution figure of energy function.

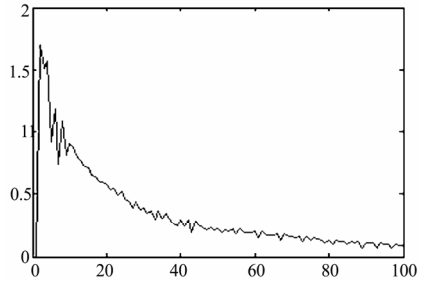

Figure 11. Time evolution figure of Lyapunov exponent.

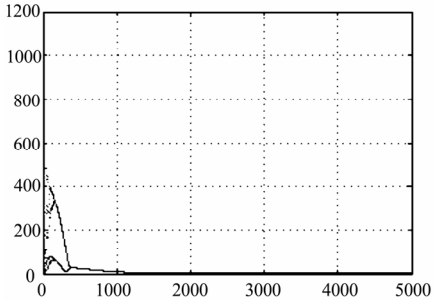

Figure 12. Time evolution figure of energy function.

The global minimum and its responding point of the simulation are respectively -1.0021 and (-0.074007, 0.76863).

3) Simulation on the Third Continuous Function

The rest parameters are set as follows:

$$k=1, \alpha=0.02, u=0.09, I_0=0.2.$$

The time evolution figures of most positive Lyapunov exponent and energy function of MWCNN in solving the first continuous function are shown as **Figure 11, Figure 12.**

The global minimum and its responding point of the simulation are respectively 0.39789 and (3.1413, 2.2733).

3.3. Mexican Hat Wavelet Chaotic Neural Network (MHWCNN)

1) Simulation on the First Continuous Function

The rest parameters are set as follows:

$$k=1, \alpha=0.5, u=0.2, I_0=0.8.$$

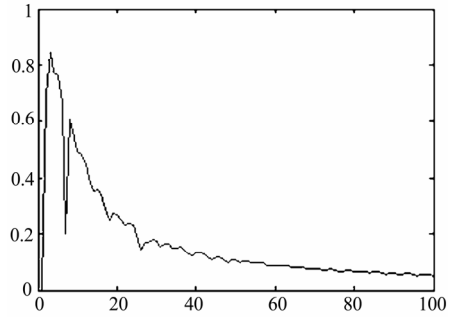

Figure 13. Time evolution figure of Lyapunov exponent.

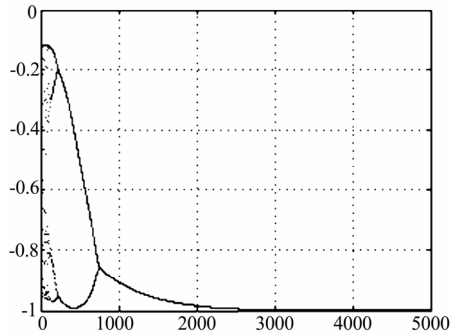

Figure 14. Time evolution figure of energy function.

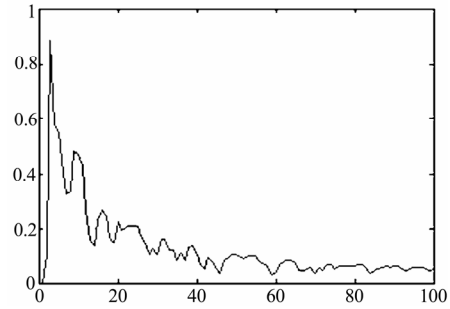

Figure 15. Time evolution figure of Lyapunov exponent.

The time evolution figures of most positive Lyapunov exponent and energy function of MHWCNN in solving the first continuous function are shown as **Figure 13**, **Figure 14.**

The global minimum and its responding point of the simulation are respectively -0.99996 and (0.0043259, 0.0043259).

2) Simulation on the Second Continuous Function

The rest parameters are set as follows:

$$k=1, \alpha=0.05, u=2.8, I_0=0.05.$$

The time evolution figures of most positive Lyapunov exponent and energy function of MHWCNN in solving the first continuous function are shown as **Figure 15**, **Figure 16.**

The global minimum and its responding point of the simulation are respectively -1.0316 and (-0.089825, 0.71263).

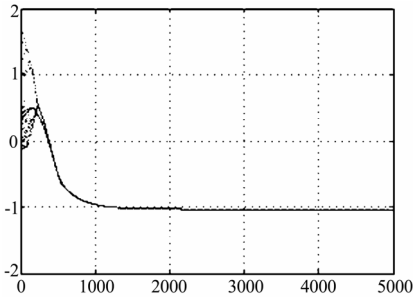

Figure 16. Time evolution figure of energy function.

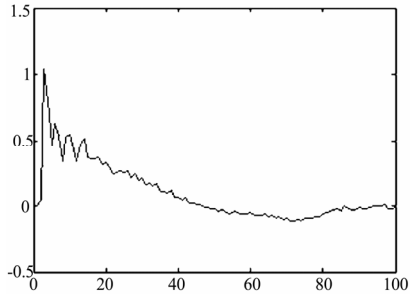

Figure 17. Time evolution figure of Lyapunov exponent.

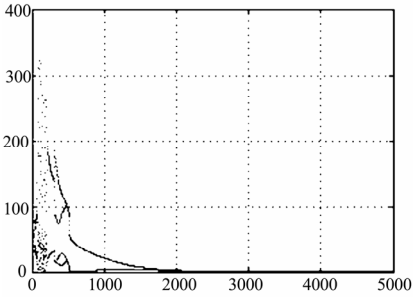

Figure 18. Time evolution figure of energy function.

Table 1. the simulation results of the chaotic neural networks.

Fun	Model / GM/ER	Chen's	MWCNN	MHWCNN
f_1	TGM	-1	-1	-1
	PGM	-0.99989	*-0.99997*	-0.99996
	ER	0.00011	0.00003	0.00004
f_2	TGM	-1.0316285	-1.0316285	-1.0316285
	PGM	-1	-1.00021	-1.0316
	ER	0.0316285	0.0314185	0.0000285
f_4	TGM	0.398	0.398	0.398
	PGM	0.3789	0.3789	0.3789
	ER	0.0191	0.0191	0.0191
AVE	AVER	0.01270962	0.01263712	0.00479212

3) Simulation on the Third Continuous Function**.**

The rest parameters are set as follows:

$$k=1, \alpha=0.05, \quad u=0.3, I_0=0.2.$$

The time evolution figures of most positive Lyapunov exponent and energy function of MHWCNN in solving the first continuous function are shown as **Figure 17**, **Figure 18.**

The global minimum and its responding point of the simulation are respectively 0.39789 and (3.1415, 2.2743).

4. ANALYSIS OF THE SIMULATION RESULTS

Simulation results are summarized in **Table 1**. The columns "GM/ER", "TGM", "PGM" and "AVER" represent, respectively, global minimum/error rate; theoretical global minimum; practical global minimum; average error.

Seen from the **Table 1**, we can conclude that the wavelet chaotic neural networks are superior to Chen's in AVER

5. CONCLUSIONS

We have introduced Chen's and wavelet chaotic neural networks. We make an analysis of them in solving continuous function optimization problems, and find out that wavelet chaotic neural networks are superior to Chen's in general.

REFERENCES

[1] J. J. Hopfield and D. W. Tank, (1985) Neural computation of decision in optimization problems. Biol. Cybern., **52**, 141-152.

[2] J. Hopfield, (1982) Neural networks and physical systems with emergent collective computa-tional abilities. In: Proc Natl Acad Sci, **79**, 2554-2558.

[3] J. Hopfield, (1984) Neural networks and physical systems with emergent collective computational abilities. 81, Proc. Natl. Acad. Sci., 3088-3092.

[4] Y. Q. Xu, M. Sun, and G. R. Duan, (2006) Wavelet chaotic neural networks and their application to optimization problems. Lecture Notes in Computer Science.

[5] L. P. Wang and F. Y. Tian, (2000) Noisy chaotic neural networks for solving combinatorial optimization problems. International Joint Conference on Neural Networks. Italy, IEEE, 37-40.

[6] L. Chen and K. Aihara, (1995) Chaotic simulated annealing by a neural network model with transient chaos. Neural Networks., **8**, 915-930.

[7] L. Wang, (2001) Intelligence optimization algorithm and its application. Press of TUP.

[8] C. Q. Xie, C. He, and H. W. Zhu, (2002) Improved noisy chaotic neural networks for solving combinational optimization problems. Journal of Shanghai Jiaotong university, **36**, 351-354.

[9] Y. Q. Xu and M. Sun, (2006) Gauss-morlet-sigmoid chaotic neural networks. ICIC, LNCS.

Vol.1, No.3, 210-215 (2009)
doi:10.4236/ns.2009.13028

Natural Science

Development on ethanol production from xylose by recombinant *Saccharomyces cerevisiae*

Jin-Ying Yang, Jian-Ren Lu*, Hong-Yue Dang, Yan Li, Bao-Sheng Ge

Center for Bioengineering and Biotechnology of China University of Petroleum, Qingdao, China

Received 26 August 2009; revised 28 September 2009; accepted 30 September 2009.

ABSTRACT

Xylose is the second major fermentable sugar present in lignocellulosic hydrolysates, so its fermentation is essential for the economic conversion of lignocellulose to ethanol. However, the traditional ethanol production strain *Saccharomyces cerevisiae* does not naturally use xylose as a substrate. A number of different approaches have been used to engineer yeasts to reconstruct the gene background of *S. cerevisiae* in recent years. The recombinant strains showed better xylose fermentation quality by comparison with the natural strains. This review examines the research on *S. cerevisiae* strains that have been genetically modified or adapted to ferment xylose to ethanol from three aspects including construction of xylose transportation, xylose-metabolic pathway and inhibitor tolerance improvement of *S. cerevisiae*.

Keywords: *Sacchromyces cerevisiae*; Xylose; Ethanol; Metabolic Engineering

1. INTRODUCTION

Rising concerns over the cost of petroleum and the prospect of global warming are driving the development of technologies for the production of alternative fuels such as ethanol [1]. Cellulosic biomass is an attractive feedstock for fuel ethanol production since it is readily available, e.g., as a waste from the pulp and paper or agricultural industries, and also due to the fact that it is renewable with cycles many orders of magnitude shorter compared with those of fossil fuels. Hydrolysates of cellulosic biomass will contain mixtures of sugars, including glucose, galactose, mannose, xylose and arabinose, and other constituents in variable proportions depending on the source [2]. Successful industrial production of ethanol from lignocellulosic hydrolysate depends on the quantitative conversion of carbon present in the biomass. It is well known that one of the most effective ethanol-producing organisms for hexose sugars is *Saccharomyces cerevisiae*, which shows high ethanol productivity, high tolerance to ethanol, and tolerance to inhibitory compounds present in the hydrolysate of lignocellulosic biomass [3-5]. However, *S. cerevisiae* does not naturally use xylose as a substrate. Only a few yeasts such as *Pichia stipitis* [6] and *Pachysolen tannophilus* [7] are able to ferment xylose. Genetic engineering can be used to enable *S. cerevisiae* to transport and ferment xylose including modeling, mutation, deletion and so on.

The pentose phosphate pathway (PPP) [8] is a process that serves to generate NADPH for reductive biosynthesis reactions within cells and the synthesis of pentose (5-carbon) sugars for the synthesis of the nucleotides and nucleic acids. There are two distinct phases in the pathway. The oxidative phase converts the hexose, D-glucose 6P, into the pentose, D-ribulose 5P, plus CO_2 and NADPH. The non-oxidative phase converts D-ribulose 5P into D-ribose 5P, D-xylulose 5P, D- sedoheptulose 7P, D-erythrose 4P, D-fructose 6P and D- glyceraldehyde 3P. D-Xylose and L-arabinose enter the PPP through D-xylulose (**Figure 1**)

In bacteria, xylose is directly isomerized to xylulose by xylose isomerase (XI) before entering pentose phosphate pathway. In xylose-fermenting yeasts, xylose is first reduced to xylitol by xylose reductase (XR) and then oxidized to xylulose by xylitol dehydrogenase (XDH) [9]. Xylulokinase (XK) phosphorylates xylulose to xylulose 5-phosphate, which is then metabolized through the PPP and glycolysis (**Figure 2**). *S. cerevisiae* is not able to metabolize xylose due to the lack of XR and XDH activity, but it can utilize the isomeric form xylulose.

2. ENGINEERING YEASTS FOR XYLOSE METABOLISM

2.1. Xylose Uptake

Xylose is not readily fermentable in wild-type strains of *S. cerevisiae*. To circumvent this problem, different

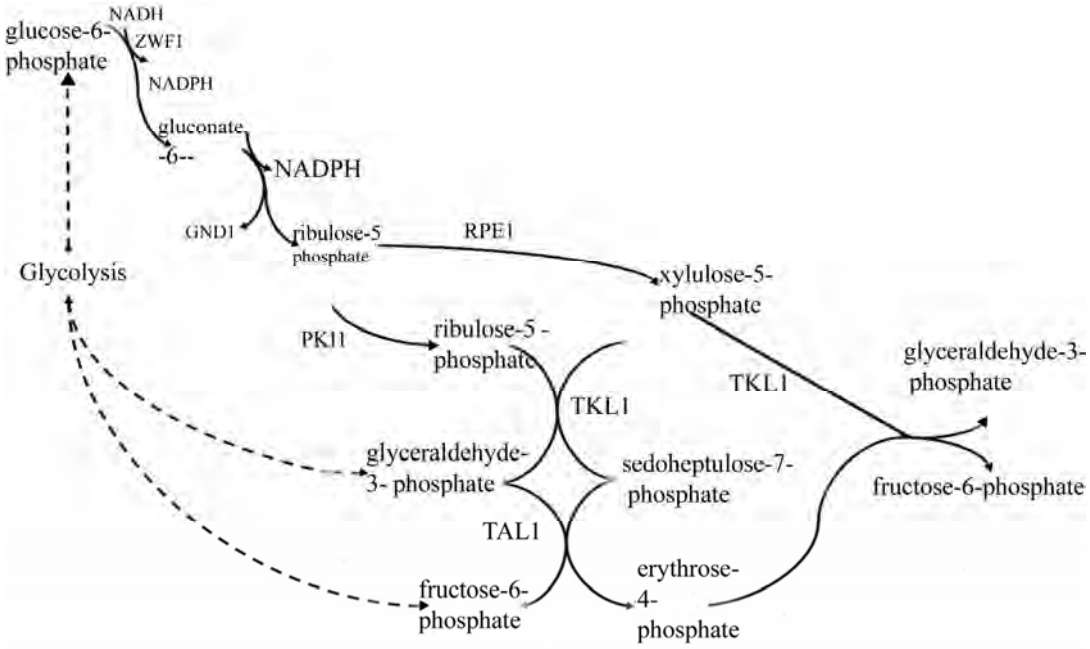

Engineering pentose metabolism in yeasts. The pentose phosphate pathway (PPP) in yeasts contains the oxidative phase, which consists of glucose 6-phosphate dehydrogenase (ZWF1) and 6-phosphogluconate dehydrogenase (GND1), and the non-oxidative phase, which is carried out by D-ribulose-5-phosphate 3-epimerase (RPE1), ribose-5-phosphate ketol-isomerase (RKI1), transketolase (TKL1) and transaldolase (TAL1).

Figure 1. The pentose phosphate pathway.

metabolic engineering strategies have been applied to enable xylose metabolism, and pentose-fermenting strains of *S. cerevisiae* have been created principally by engineering the pathways for converting xylose to xylulose-5-phosphate [10,11]. However, fermentation of xylose still remains significantly less efficient than that of glucose by these strains. The uptake of xylose into the cell is one of the reasons.

The *S. ceresiave* genome contains 20 genes that encode for hexose transporters but does not contain genes for xylose-specific transport system like natural xylose-utilizing yeasts [12]. Uptake of xylose by *S. cerevisiae* has been proposed to be mediated more or less unspecifically by its hexose-transport system. This is composed of a large family of 18 related transporter proteins called Hxts and additional sugar transporters with broader substrate specificity [13,14].

Hamacher *et al.* [12] found that after deletion of all of the 18 hexose-transporter genes, the ability of *S. cerevisiae* cells to take up and to grow on xylose was lost. Re-introduction and constitutive expression of individual HXT genes in strain TMB3201 revealed that at 2% xylose concentrations, high- (Hxt7 and Gal2) and intermediate-affinity (Hxt4 and Hxt5) glucose transporters are required for xylose uptake.

Several studies have indicated that in *S. cerevisiae* glucose and xylose appear to share the same transport facilities and competitively inhibit their mutual transport [15,16]. Competition with glucose restricts xylose assimilation, so heterologous expression of a specific xylose transporter could be very useful.

Researchers have tried to identify genes target for improved xylose assimilation. Two genes (*GXF1*and *GSX1*) encoding xylose/glucose transporters from *Candida intermedia* were isolated by Leandro *et al.* [17], and expressed in *S. cerevisiae*. *Gsx1* is the first yeast xylose/glucose–H^+ symporter to be characterized in *Arabidopsis thaliana* at the molecular level. Except GSX1, xylose transporters from *Arabidopsis thaliana*

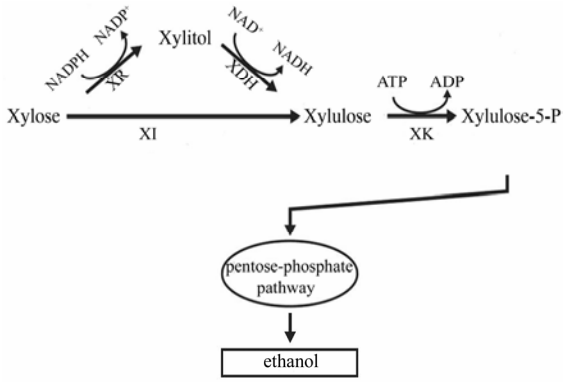

XR: Xylose reductase; XDH : xylitol dehydrogenase; XK : Xylulokinase

Figure 2. The metabolism of xylose in bacteria.

(At5g59250) and *Escherichia coli (xylE)* were also expressed in *S. ceresiave* TMB3120 and failed to support vigorous growth of the recipient *S. cerevisiae* strain on xylose. Even though, the results warrant further investigations for the development of efficient bioethanol production processes from lignocellulosic materials.

The presence of three sugar transporters in *P. stipitis, Sut1, Sut2 and Sut3* has been reported. Although all three transporters have a higher affinity for glucose than for xylose, the Sut1 transporter has a higher *Vmax* for xylose uptake compared to other two Sut transporters and for hexose transporters [18,19]. Satoshi Katahira [20] *et al.* introduced SUT1 into a xylose-assimilating *S. cerevisiae* strain that expresses xylose reductase, xylosedehydrogenase and xylulokinase. The results showed that expression of Sut1 in xylose-assimilating *S. cerevisiae* increased both xylose uptake ability and ethanol productivity during xylose fermentation. Also, the enhancement of xylose uptake enables to accelerate the ethanol productivity during xylose/glucose co-fermentation. However, there are researchers with different opinions. Gárdonyi *et al*. [21,22] concluded that xylose transport in *S. cerevisiae* strains has low control over the rate of xylose utilization, unless the xylose pathway is significantly improved. In-depth study of the transporters' mechanism along with new modeling should continue to drive this field forward.

2.2. Construction of Recomnant *S.* Cerevisiae Strains with Xylose-Fermenting Ability

2.2.1. Recombinant *S. cerevisiae* Expressing XR, XDH, and XK

Researchers have engaged in the development of engineered yeast strains capable of xylose fermentation by introducing XR and XDH into *S. cerevisiae*. Both of these enzymes have been isolated and characterized due to the central role they play in xylose metabolism.

The purified monomeric XR was NADPH-dependent with an apparent MW of 37 kDa, which was firstly purified and characterized by Kuhn *et al*. [23] XDHs also have been purified and characterized from various xylose-fermenting yeasts.

Kötter *et al*. [24] first reported the construction of a *S. cerevisiae* strain expressing the XR- and XDH-encoding genes XYL1 and XYL2 derived from the xylose-utilizing yeast *P. stipitis*. Walfridsson *et al*. [25] also genetically engineered *S. cerevisiae* to utilize xylose by introducing the XYL1 and XYL2 genes on either multicopy plasmids or by integrating them into the chromosome.

Although these strains can ferment xylose to ethanol, the excretion of xylitol occurs unless a co-metabolizable carbon source such as glucose is added. One of the most important reason is intercellular redox imbalance due to a different coenzyme specificity of xylose reductase (with $NADPH^+$) and XDH (with NAD^+) [26]. Protein-engineering of $NADPH^+$-preferring XR and/or NAD^+-dependent XDH is an alternative approach to solve the problem.

Anderlund [27] constructed four chimeric genes encoding fusion proteins of *XYL1* and *XYL2* with different orders of the enzymes and different linker lengths. These genes were expressed in *S. cerevisiae*. The fusion proteins exhibited both XR and XDH activity when XYL1 was fused downstream of XYL2. The results showed that the xylitol yield was lower in these strains than in strains expressing only native XR and XDH monomers, 0.55 and 0.62, respectively, and the ethanol yield was higher.

By analyzing the amino acid of coenzyme-binding domain of XDH, Watanabe [28] modified XDH from *P. stipitis* by three- and four-site direct mutagenesis. The triple mutant (D207A/I208R/F209S) and quadruple mutant (D207A/I208R/F209S/N211R) showed more than 4500-fold higher values in *kcat/Km* with $NADP^+$ than the wild-type enzyme, reaching values comparable with *kcat/Km* with NAD^+ of the wild-type enzyme.

In recent years, the research group introduced these mutated PsXDHs with the PsXR WT to *S. cerevisiae* and estimated effect(s) of the functional modification(s) of PsXDH on fermentation of xylose to ethanol in recombinant *S. cerevisiae* [29]. The results showed that recombinant yeast strains gave the highest ethanol production and the lowest xylitol excretion.

Zeng *et al.* [30] altered the coenzyme specificity of *P. stipitis* XR via rational design based on the 3D structure. Lys21, the only one amino acid that has hydrogen binding interaction with $NADP^+$ but not with NAD^+ in the binding pocket, were changed to Ala and Arg respectively. The results showed that the coenzyme dependence of K21A was completely reversed to $NADH^+$.

2.2.2. Recombinant *S. cerevisiae* Expressing Xylose Isomerase

Xylose isomerase (XI), encoded by the *xylA* gene, catalyzes the isomerization of xylose to xylulose in bacteria and some fungi [31]. *xylA* has been cloned into *S. cerevisiae* from several bacteria. However the XI produced by the recombinant *S. cerevisiae* strains was inactive. Improper protein folding, postranslational modifications, inter- and intramolecular disulfide bridge formation, and the internal pH of yeast have been suggested as possible reasons [32].

In 1996, Walfridsson *et al*. [33] cloned the *Thermus thermophilus xylA* gene encoding xylose (glucose) isomerase and successfully expressed in *S. cerevisiae* under the control of the yeast *PGK1* promoter. The recombinant xylose isomerase showed the highest activity at 85℃ with a specific activity of 1.0 U/mg. It was the first successful attempt to express the procaryotic gene *xylA* for the enzyme XI in the eucaryote *S. cerevisiae*,

which could be due to the relatedness between the two organisms. The recombinant strains could not covert xylose to ethanol efficiently because the temperature and pH optimum for the recombinant enzyme are high.

The *XylA* gene from the anaerobic fungus *Piromyces* sp. E2 (ATCC 76762) was functionally expressed in *S. cerevisiae* by Marko Kuyper *et al.* [34]. After prolonged cultivation on xylose, a mutant strain was obtained that grew aerobically and anaerobically on xylose. The anaerobic ethanol yield was 0.42 g ethanol /g. xylose and also by-product formation was comparable to that of glucose-grown anaerobic cultures.

In 2009, Brat *et al.* [35] cloned and successfully expressed a highly active new kind of xylose isomerase from the anaerobic bacterium *Clostridium phytofermentans* in *S. cerevisiae*. The recombinant yeast cells with heterologous expression got the ability to metabolize D-xylose and to use it as the sole carbon and energy source. The new enzyme has low sequence similarities to the XI *Thermus thermophilus* and *Piromyces sp. E2*, which were the only two xylose isomerases previously functionally expressed in *S. cerevisiae*. Importantly, the new enzyme is far less inhibited by xylitol, which accrues as a side-product during xylose fermentation. The findings provided an excellent starting point for further improvement of xylose fermentation in industrial yeast strains.

3. OPTIMIZATION OF DOWNSTREAM METABOLIC PATHWAYS

3.1. Xylulokinase

Although recombinant strains containing genes coding for XR and XDH from the xylose-utilizing yeast *P. stipitis* have been reported, such strains ferment xylose to ethanol poorly. One reason for this may be the low capacity of xylulokinase, the third enzyme in the xylose pathway [36,37].

Xylulokinase is an enzyme that catalyzes the chemical reaction: ATP + D-xylulose $\rightleftharpoons$ ADP + D-xylulose 5-phosphate. In 1989, Ho *et al.* [38] cloned the xylulokinase (xks1) gene from *S. cerevisiae* and firstly overexpressed in *S. cerevisiae*. Toivari *et al*. [39] also overexpressed the endogenous gene for xylulokinase (xks1) in *S. cerevisiae* along with the *P. stipitis* genes for XR and XDH. The metabolism of this recombinant yeast was further investigated in pure xylose bioreactor cultivation at various oxygen levels. The results clearly indicated that overexpression of xks1 significantly enhanced the specific rate of xylose utilization. In addition, the XK-overexpressing strain can more efficiently convert xylose to ethanol under all aeration conditions studied. These two studies represented an important step in efforts to improve xylose metabolism in *S. cerevisiae*, as their results strongly indicated that native XK activity was insufficient for xylose or xylulose fermentation, and overexpression was required to obtain high ethanol yields.

3.2. Transketolase and Ransaldolase

Transketolase and transaldolase catalyze transfer of 2-C and 3-C molecular fragments respectively, in each case from a ketose donor to an aldose acceptor. The two enzymes have been implicated as being rate-limiting for xylose and xylulose fermentation.

The TKL1 and TAL1 genes encoding transketolase and transaldolase were overexpressed individually and together in the *S. cerevisiae* strain containing XYL and XYL2. The strain overexpressing TAL1 showed considerably enhanced growth on xylose compared with a strain containing only XYL1 and XYL2. Overexpression of only TKL1 did not influence growth. The results indicated that the transaldolase level in *S. cerevisiae* is insufficient for the efficient utilization of pentose phosphate pathway metabolites [40]. Bao *et al*. [41] also found that the *S. cerevisiae* strain overexpressing the TAL1 and TKL1 showed considerably good growth on the xylose plate.

4. IMPROVEMENT OF TOLERANCE TO INHIBITORS

The growth of *S. cerevisiae* and ethanol production were limited by multiple inhibitors, including furan derivatives, 5-hydroxymethylfurfural (HMF), weak acids, and phenolic compounds produced during biomass-to-ethanol processing. The PPP is an important pathway incarbohydrate metabolism, and a lot of previous studies have shown a correlation between several PPP genes and specific stresses such as oxidative [42], sorbic acid [43], and osmotic [44].

To improve production of fuel ethanol from renewable raw materials, laccase from the white rot fungus *Trametes versicolor* was expressed under control of the *PGK1* promoter in *S. cerevisiae* to increase its resistance to phenolic inhibitors in lignocellulose hydrolysates [45]. To identify target genes involved in furfural tolerance, Gorsich [46] screened a *S. cerevisiae* gene disruption library for mutants with growth deficiencies in the presence of furfural. As a result, more than 62 genes were found to be associated with sensitivity to furfural. They also further showed that overexpression of ZWF1 in *S. cerevisiae* allowed growth at furfural concentrations that are normally toxic, which demonstrated a strong relationship between PPP genes and furfural tolerance.

Adapting strains is also an alternative to improve the performance of microorganisms. Liu [47] improved bio-

transformation by newly developed strains adapted to tolerate the challenges of furfural and HMF in batch cultures compared with the parental strains. The results suggest a possible *in situ* detoxification of the inhibitors for bioethanol fermentation using improved yeast strains. Although they have not been tested against inhibitor complexes such as those in a biomass hydrolysate, the development and study of such strains provided necessary materials for further studies of the mechanisms of the stress tolerance at molecular and genomic levels.

5. CONCLUSIONS

The bioconversion of cellulose and hemicellulose to biofuels and chemicals is being actively researched with the aim of developing technically and economically viable processes. D-Xylose is the major product of the hydrolysis of hemicellulose and considerable research efforts has been focused on the development of xylose-fermenting recombinant *S. cerevisiae.* Significant improvements in ethanol productivity from xylose have been achieved through metabolic engineering. However, there are still unidentified limiting steps in the xylose metabolism of metabolically engineered *S. cerevisiae,* such as lower ethanol yield, more byproducts, the suitability of these recombinant strains and so on. There are still many tasks that left in the xylose-metabolic engineering. So far the recombinant *S. cerevisiae* were constructed base on the laboratory strains, which are less complex in genetic background, growth characters, and physiological characters comparing with the industrial yeast strains. To get strains easy to be industrialized, more emphasis should be focused on the reconstruction of the wild type yeasts. Further improve the expression and stability of the heterogenous genes in yeasts can be expected for higher ethanol yield.

REFERENCES

[1] A. J. Ragauskas, C. K. Williams, B. H. Davison, *et al.* (2006) The path forward for biofuels and biomaterials. [J]. Science, **311**, 484-489.

[2] A. Wiselogel, S. Tyson, and D. Johnsson, (1996) Biomass feedstock resources and composition. [M]. C. E.Wyman (Editor), Handbook on bioethanol: Production and utilization. Washington, Taylor and Francis, 105-118.

[3] L. Olsson and B. Hahn-Hägerdal, (1993) Fermentative performance of bacteria and yeast in lignocellulose hydrolysates. [J]. Process Biochemistry, **28(4)**, 249-257.

[4] L. Olsson and J. Nielsen, (2000) The role of metabolic engineering in the improvement of *Saccharomyces cerevisiae*: Utilization of industrial media. [J]. Enzyme Microbial Technology, **26(9-10)**, 785-792.

[5] B. Hahn-Hägerdal, C. F. Wahlbom, M. Gárdonyi, *et al*., (2001) Metabolic engineering of *Saccharomyces cerevisiae* for xylose utilization. Advances in Biochemistry Engineering and Biotechnology, **73**, 53-84.

[6] T. W. Jeffries, I. V. Grigoriev, J. Grimwood, *et al*., (2007) Genome sequence of the lignocellulose-bioconverting and xylose-fermenting yeast *Pichia stipitis.* [J]. Nature Biotechnology, **25**, 319-326.

[7] P. J. Slininger, R. J. Bothast, J. E. Vancauwenberge, *et al*., (1982) Conversion of D-xylose to ethanol by the yeast *Pachysolen tannophilus* [J]. Biotechnology and Bioengineering, 24(2), 371-384.

[8] T. W. Jeffries, (2006) Engineering yeasts for xylose metabolism. [J]. Current Opinion in Biotechnology, **17**, 320- 326.

[9] K. L. Träff, R. R. O. Cordero, W. H. van Zyl, *et al*., (2001) Deletion of the GRE3 aldose-reductase gene and its influence on xylose metabolism in recombinant strains of *Saccharomyces cerevisiae* expressing the xylA and Xks1 genes. [J], Applied and Environmental Microbiology, **67(12)**, 5668-5674.

[10] A. Eliasson, C. Christensson, C. F. Wahlbom, *et al*., (2000) Anaerobic xylose fermentation by Recombinant *Saccharomyces cerevisiae* Carrying XYL1, XYL2 and XKS1 in Mineral Medium Chemostat Cultures. [J]. Applied and Environmental Microbiology, **66(8)**, 3381-33-86.

[11] M. Kuyper, M. M. P. Hartog, M. J. oirkens, *et al*., (2005) Metabolic engineering of a xylose-isomerase-expressing *Saccharomyces cerevisiae* strain for rapid anaerobic xylose fermentation. [J]. FEMS Yeast Research, **5(4-5)**, 399-409.

[12] T. Hamacher, J. Becker, M. Gárdonyi, *et al*., (2002) Characterization of xylose-transporting properties of yeast hexose transporters and their influence on xylose utilization. [J]. Microbiology, **148**, 2783-2788.

[13] E. Boles and C. P. Hollenberg, (1997) The molecular genetics of hexose transport in yeasts. [J]. FEMS Microbiology Reviews, **21(1)**, 85-111.

[14] R. Wieczorke, S. Krampe, T. Weierstall, *et al*., (1999) Concurrent knock-out of at least 20 transporter genes is required to block uptake of hexoses in Saccharomyces cerevisiae. [J]. FEBS Letter, **464**, 123-128.

[15] A. Kotyk, (1968) Properties of the sugar carrier in baker's yeast. [J]. Folia Microbiologica, **13(3)**, 212-220.

[16] P. Kötter and M. Ciriacy, (1993) Xylose fermentation by *Saccharomyces cerevisiae* [J]. Applied Microbiology and Biotechnology, **38(6)**, 776-783.

[17] L. M. José, P. Goncalves, and I. Spencer-Martins, (2006) Two glucose / xylose transporter genes from the yeast *Candida intermedia*: First molecular characterization of a yeast xylose–H^+ symporter. [J]. Biochemistry Journal, **395(3)**, 543-549.

[18] T. Weierstall, C. P. Hollenberg, and E. Boles, (1999) Cloning and characterization of three genes (*SUT1-3*) encoding glucose transporters of the yeast *Pichia stipitis.* [J]. Molecular Microbiology, **31(3)**, 871-883.

[19] T. Hamacher, J. Becker, M. Gárdonyi, *et al*., (2002) Characterization of the xylose-transporting properties of yeast hexose transporters and their influence on xylose utilization [J]. Microbiology, **148**, 2783-2788.

[20] S. Katahira, M. Ito, H. Takema, *et al*., (2008) Improvement of ethanol productivity during xylose and glucose co-fermentation by xylose-assimilating *S. cerevisiae* via expression of glucose transporter Sut1 [J]. Enzyme and Microbial Technology, **43(2)**, 115-119.

[21] M. Gárdonyi, M. Jeppsson, G. Lidén, *et al*., (2003) Control of xylose consumption by xylose transport in recombinant *Saccharomyces cerevisiae*. [J]. Biotechnology and Bioengineering, **82(7)**, 818–824.

[22] M. Gárdonyi, M. Österberg, C. Rodrigues, *et al*., (2003) High capacity xylose transport in *Candida intermedia* PYCC 4715. [J]. FEMS Yeast Research, **3**, 45–52.

[23] A. Kuhn, C. van Zyl, A. van Tonder, *et al*., (1995) Purification and partial characterization of an aldo-keto reductase from *Saccharomyces cerevisiae*. [J]. Applied and Environmental Microbiology, **61(4)**, 1580– 1585.

[24] P. Kötter, R. Amore, C. P. Hollenberg, *et al*., (1990) Isolation and characterization of the *Pichia stipitis* xylitol dehydrogenase gene, XYL2, and construction of a xylose-utilizing *Saccharomyces cerevisiae* transformant. [J]. Current Genetics, **18(6)**, 493-500.

[25] M. Walfridsson, J. Hallborn, M. Penttila, *et al*., (1995) Xylose-metabolizing *Saccharomyces cerevisiae* strains overexpressing the TKL1 and TAL1 genes encoding the pentose phosphate pathway enzymes transketolase and transaldolase. [J]. Applied and Environmental Microbiology, **61(12)**, 4184-4190.

[26] S. Ostergaard, L. Olsson, and J. Nielsen, (2000) Metabolic Engineering of *Saccharomyces cerevisiae.* [J]. Microbiology and Molecular Biology Reviews, **64(1)**, 34- 50.

[27] M. Anderlund, P. Rådström, and B. H. Hägerdal, (2001) Expression of bifunctional enzymes with Xylose Reductase and Xylitol Dehydrogenase activity in *Saccharomyces cerevisiae* alters product formation during Xylose fermentation. [J]. Metabolic Engineering, **3(3)**, 226-235.

[28] S. Watanabe, T. Kodaki, and K. Makino, (2005) Complete reversal of coenzyme specificity of xylitol dehydrogenase and increase of thermostability by the introduction of structural zinc. [J]. The Journal of Biological Chemistry, **280(11)**, 10340-10349.

[29] S. Watanabe, A. A. Salehb, S. P. Pack, *et al*., (2007) Ethanol production from xylose by recombinant Saccharomyces cerevisiae expressing protein engineered $NADP^+$-dependent xylitol dehydrogenase. [J]. Journal of Biotechnology, **130**,316–319.

[30] Q. K. Zeng, H. L. Du, Z. C. Zhai, *et al*., (2008) Mutational research on the role of Lysine 21 in the *Pichia stipitis* Xylose Reductase. [J]. Chinese Journal of Biotechnology, **24(6)**, 1108-1111.

[31] T. W. Jeffries and Y. S. Jin, (2000) Ethanol and thermotolerance in the bioconversion of xylose by yeasts [J]. Advances in Applied Microbiology, **47**, 221-268.

[32] R. Amore, M. Wilhelm, and C. P. Hollenberg, (1989) The fermentation of xylose—An analysis of the expression of Bacillus and Actinoplanes xylose isomerase gens in yeast. [J]. Applied Microbiology and Biotechnology, **30(4)**, 351-357.

[33] M. Walfridsson, X. Bao, M. Anderlund, *et al*., **(**1996) Ethanolic fermentation of xylose with *Saccharomyces cerevisiae* harboring the *Thermus thermophilus xylA gene*, which expresses an active xylose (glucose) isomerase. [J]. Applied and Environmental Microbiology, **62(12)**, 4648-4651.

[34] M. Kuyper, A. A. Winkler, J. P. van Dijken, *et al*., (2001) Minimal metabolic engineering of *Saccharomyces cerevisiae* for efficient anaerobic xylose fermentation: a proof of principle. [J]. FEMS Yeast Research, **4(6)**, 655-664.

[35] D. Brat, E. Boles, and B. Wiedemann, (2009) Functional expression of a bacterial xylose isomerase in Saccharomyces cerevisiae. [J]. Applied and Environmental Microbiology, **75(8)**, 2304-2311.

[36] Y. S. Jin and T. W. Jeffries, (2003) Changing flux of xylose metabolites by altering expression of xylose reductase and xylitol dehydrogenase in recombinant *Saccharomyces cerevisiae.* [J]. Applied Biochemistry and Biotechnology, **106(1-3)**, 277-285.

[37] X. D. Xue and N. W. Y. Ho, (1990) Xylulokinase activity in various yeasts including *Saccharomyces cerevisiae* containing the cloned xylulokinase gene. [J]. Applied Biochemistry and Biotechnology, **24-25(1)**, 193-199.

[38] N. W. Y. Ho and S. F. Chang, (1989) Cloning of yeast xylulokinase gene by complementation in *Escherichia coli* and yeast mutations. [J]. Enzyme Microbial Technology, **11**, 417-421.

[39] M. H. Toivari, A. Aristidou, L. Ruohonen, *et al*., (2001) Conversion of Xyl ose to ethanol by recombinant *Saccharomyces cerevisiae*: importance of Xylulokinase (XKS1) and oxygen availability. [J]. Metabolic Engineering, **3(3)**, 236-249.

[40] M. Walfridsson, J. Hallborn, M. Penttilä, *et al*., (1995) Xylose-metabolizing *Saccharomyces cerevisiae* strains overexpressing the TKL1 and TAL1 genes encoding the pentose phosphate pathway enzymes transketolase and transaldolase. [J]. Applied and Environmental Microbiology, **61(12)**, 4184–4190.

[41] X. Bao, D. Gao, Y. Qu, *et al*., (1997) Effect on product formation in recombinant *Saccharomyces cerevisiae* strains expressing different levels of xylose metabolic genes. [J]. Chinese Journal of Biotechnology, **13(4)**, 225- 231.

[42] H. Juhnke, B. Krems, P. Kotter, *et al*., (1996) Mutants that show increased sensitivity to hydrogen peroxide reveal an important role for the pentose phosphate pathway in protection of yeast against oxidative stress. [J]. Molecular & General Genetics, **252(4)**, 456–464.

[43] M. Mollapour, D. Fong, K. Balakrishnan, *et al*., (2004) Screening the yeast deletant mutant collection for hypersensitivity and hyperresistance to sorbate, a weak organic acid food preservative. [J]. Yeast, **21(11)**, 927–946.

[44] B. Krems, C. Charizanis, and K. D. Entian, (1995) Mutants of *Saccharomyces cerevisiae* sensitive to oxidative and osmotic stress. [J]. Current Genetics, **27(5)**, 427–434.

[45] S. Larsson, P. Cassland, and L. J. Jonsson, (2001) Development of a *Saccharomyces cerevisiae* strain with enhanced resistance to phenolic fermentation inhibitors in lignocellulose hydrolysates by heterologous expression of laccase. [J]. Aplied and Environmental Microbiology, **67(3)**, 1163-1170.

[46] S. W. Gorsich, B. S. Dien, N. N. Nichols, *et al*., (2006) Tolerance to furfural-induced stress is associated with pentose phosphate pathway genes *ZWF1, GND1, RPE1, and TKL1* in *Saccharomyces cerevisiae.* [J]. Applied Microbiology and Biotechnology, **71(3)**, 339-349.

[47] Z. L. Liu, P. J. Slininger, and S. W. Gorsich, (2005) Enhanced biotransformation of furfural and hydroxymethylfurfural by newly developed ethanologenic yeast strains. [J]. Applied Biochemistry and Biotechnology, **121(1-3)**, 451-460.

Vol.1, No.3, 216-221 (2009)
doi:10.4236/ns.2009.13029

Natural Science

Studies on the growth aspects of organic L-alanine maleate: a promising nonlinear optical crystal

D. Balasubramanian[1,3*], R. Jayavel[2], P. Murugakoothan[3]

[1]Department of Physics, Municipal School, Tiruvannamalai, India; dr.d.balu@gmail.com
[2]Crystal Growth Centre, Anna University, Chennai, India
[3]PG & Research Department of Physics, Pachaiyappa's College, Chennai, India

Received 17 September 2009; revised 10 October 2009; accepted 12 October 2009.

ABSTRACT

A organic nonlinear optical material, L-alanine maleate (LALM) was synthesized. Bulk Single crystals of LALM have been grown by slow cooling method with a solution pH of 5. The solubility of L-alanine maleate has been determined for various temperatures. Large size single crystal of 2.0 x 1.2 x 0.8 cm^3 has been grown with reasonable growth rate along the three crystallographic directions by optimizing the growth parameters. The structure of LALM crystal was studied by single-crystal X-ray diffraction analysis. The presence of functional groups was confirmed by Fourier transform infrared spectroscopy. The LALM crystal was analysed for its thermal and mechanical behaviours. The grown crystals have also been subjected to linear and non-linear optical property studies. From these studies, it is inferred that the LALM crystals exhibit better thermal and mechanical stabilities with improved optical properties. Thus satisfies the essential requirements for optical device fabrication.

Keywords: Organic; LALM; Crystal Growth; Bulk Single Crystals; Non-Linear Optical Crystal

1. INTRODUCTION

Recently, there is considerable interest in the synthesis of new nonlinear optical (NLO) material, both organic and inorganic, with large second-order optical nonlinearities, as these materials have a significant impact on laser technology, optical communication and optical storage technology etc. Over the years many organic and inorganic materials have been developed [1-4] to cover the potential applications in ultra-violet, near-and far-infrared wavelength regions. Amino acid nonlinear optical materials are often formed by weak van der Waals and hydrogen bonds and hence possess high degree of delocalization. The basic structure of organic NLO materials is based on the π bond system. Due to the overlapping of π orbital, the delocalization of electronic charge distribution leads to a high mobility of electrons. Functionalization of both ends of the π bond system with appropriate electron donor and acceptor groups can enhance the asymmetric electronic distribution in either or both ground and excited states, this leads to an increased optical nonlinearity. All these favourable properties paved the way for the development of amino acid crystals like L-arginine phosphate (LAP) [5], L-histidine dihydrogen phosphate (LHP) [6], L-arginine tetrafluoroborate (L-AFB) [7], L-alanine tetrafluoroborate (L-AlFB) [8], L-alanine [9], L-arginine acetate [10], and L-alanine acetate [11]. LAP crystal was reported to have promising NLO properties comparable to that of the well-known inorganic crystal of KDP. L-alanine crystal shows Type II phase matching, for doubling the Nd:YAG fundamental, by propagating the pump beam nearly normal to the {12 0} and {011} faces.

The growth of single crystals of L-alanine which is the simplest acentric member of the amino acid family has already been little investigated. In order to widen the properties of L-alanine and to develop new crystals with better NLO properties, L-alanine complexes with carboxylic acids have been tried. Maleic acid, a dicarboxylic acid with relatively large pi-conjugation has attracted much attention. Though the L-alanine maleate crystal was already grown by slow evaporation method [12], in the present study, bulk single crystals of L-alanine maleate (LALM) single crystals have been grown by the slow cooling method with optimized growth conditions first time. The grown crystals were subjected to various characterization studies. The im-

proved optical transmittance, NLO efficiency and the mechanical stability of the grown crystals were realized.

2. EXPERIMENTAL PROCEDURE

2.1. Crystal Growth

High purity (99%) L-alanine and analar grade maleic acid were taken in equimolar ratio and dissolved in de-ionized water. The solution was slightly heated and kept in undisturbed conditions. Three days later, transparent seed crystals were obtained. The synthesized salt was used to prepare the growth solution according to the following reaction.

$$CH_3-(CH)-NH_2-COOH+COOH-CH=CH-COOH$$

L-alanine + Maleic acid

$$\rightarrow CH_3-(CH)-NH_3^+-COOH\ ^-OOC-CH=CH-COOH$$

L-alanine maleate (LALM)

The amount of L-alanine maleate dissolved in 10 ml of water at 30 ºC was estimated from the saturated solution. The solubility was estimated for different temperatures and the solubility of L-alanine maleate at 40 ºC is estimated to be 33 g/100 ml. Crystals were grown from aqueous solution prepared from the recrystallized salt of LALM saturated at 40 ºC. In order to reproduce the supersaturation conditions, the solution was tested by checking the dissolution of a probe crystal over a period of one week. Then the solution was cooled down at a rate of 0.1 °C/day over a period of 25 days. Optical quality single crystal elongated in c-axis was obtained.

2.2. Characterization

The structure of the crystals was examined by single-crystal X-ray diffraction analysis and the lattice parameter values were determined. Powder X-ray diffraction analysis was also carried out using a Rich Seifert diffractometer with CuK$_\alpha$ (λ = 1.5418 Å) radiation to verify the correctness of lattice parameter values. FTIR spectrum was recorded by the KBr pellet technique using a Perkin–Elmer 783 spectrophotometer in order to confirm the presence of functional groups in the crystal lattice. Optical transmittance spectrum was recorded at room temperature using Shimadzu 1601 (UV-VIS) spectrophotometer. Optical second-harmonic generation was measured for the grown crystalline sample using Kurtz and Perry technique. Thermo gravimetric (TG) and Differential thermal analysis (DTA) for L-alanine maleate dihydrate crystals were carried out by ZETZSCH–Geratebau GmbH Thermal Analyzer. Etching studies were carried out on the {011} face of L-alanine maleate crystal using different etchants like water, methanol and ethanol, in order to investigate the growth mechanism and surface features. Microhardness studies were carried out on the {011} face of the L-alanine maleate crystals.

3. RESULTS AND DISCUSSIONS

As-grown crystal of L-alanine maleate (LALM) is shown in **Figure 1**. The crystals possess well defined morphology with reasonable growth rate along all the three crystallographic directions. The molecular structure with the numbering scheme is shown in the **Figure 2**. The cationic alanine molecule exists with a positively charged amino group and an uncharged carboxylic acid group. The maleic acid molecule exists in the monoionized state (i.e. as a semimaleate). The semimaleate ion is essentially planar and the intramolecular hydrogen bond between atoms O3 and O5 is found to be asymmetric, as in the crystal structure of maleic acid [13]. The single crystal X- ray diffraction studies confirm the orthorhombic structure with space group $P2_12_12_1$. The lattice parameter values of LALM were calculated as given in the **Table 1**.

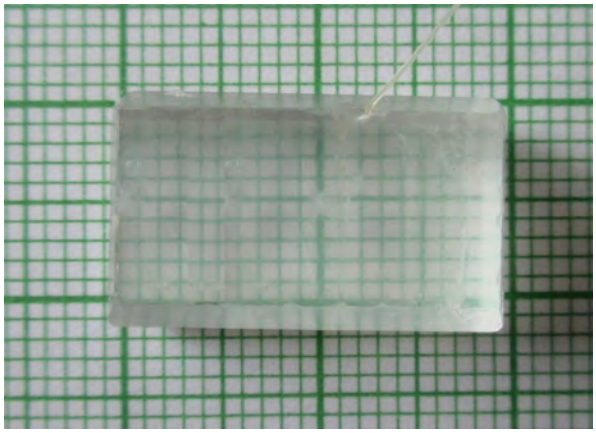

Figure 1. Bulk single crystal of LALM grown in optimizedgrowth condition.

Table 1. The single crystal X-ray data for LALM single crystal.

Molecular formula	$C_3H_8O_2N^+ \cdot C_4H_3O_4^-$
Molecular weight	205.17
System	Orthorhompic
Space group	$P2_12_12_1$
Lattice parameter	a = 5.5873 Å, b = 7.3864 Å, c = 23.688 Å
Volume (V)	977.6 Å^3
Number of atom in unit cell (Z)	4
Density	1.394 Mgm^{-3}

The FTIR absorption spectrum of LALM is shown in **Figure 3**. A broad, strong absorption in the 3300–2300 cm^{-1} range, including the absorptions at 3205 cm^{-1} corresponds to the stretching bonds of the NH_3^+ ion of the amino acid. This region is due to superimposing of O–H and NH_3^+ stretching bonds. Absorption in this region was also characterized by multiple fine structures on the lower wave number side of the bond and the weak absorptions due to COO^- ions. The prominent absorption band is relatively strong due to symmetric NH_3^+ bending bond at 1569 cm^{-1}. A strong band arising from C–COO^- stretching is observed at 1219 cm^{-1}. Further strong carbonyl absorption at 1722 cm^{-1} confirms the COOH and COO^- groups of the compound. The C=O stretch of carboxylic acid was observed to produce its peak in the same region of asymmetrical NH_3^+ bending vibration.

The CH_3 bending modes were assigned to the peak at 1374 cm^{-1}. O–H bending of the COOH group was observed at 1333 cm^{-1}. The peaks between 918 and 1106 cm^{-1} were assigned to asymmetrical coupled vibration of maleic acid and alanine.

This analysis also indicates that the protonation of carboxyl group in alanine takes place by maleic acid. The absorptions of LALM have been compared with those of the L-alanine [14] in **Table 2**. The shifts in the positions of the characteristic peaks confirm the formation of the compound.

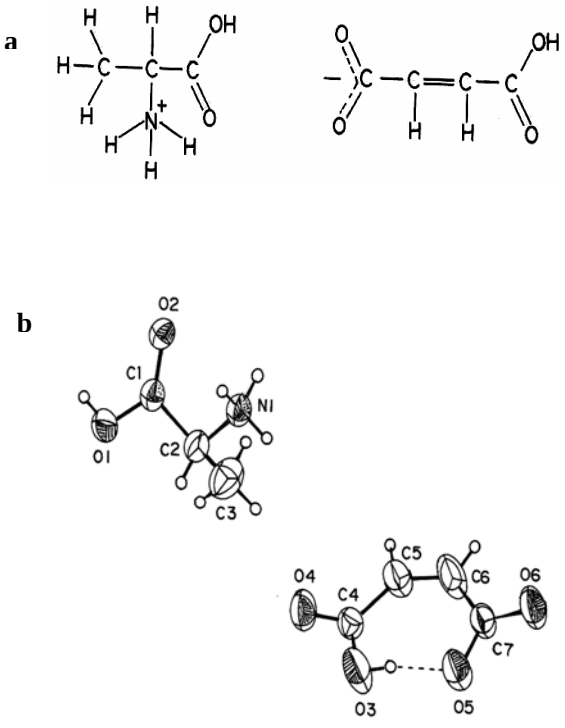

Figure 2. The molecular structure of LALM with atom-numbering scheme and 50%probability displacement ellipsoids.

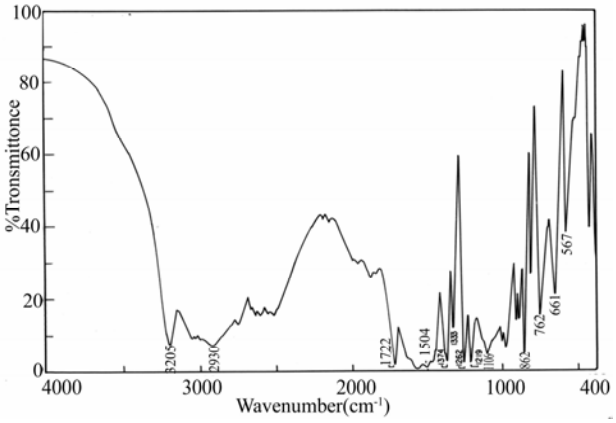

Figure 3. FT-IR spectrum of LALM crystal.

Table 2. FT-IR spectral band assignments of LALM.

L-alanine	LALM	Assignments
	3205	NH_3^+ asymmetric stretching
	2930	C-H stretching
	1722	COO^- stretching
1506	1504	NH_3^+ symmetric bending
1361	1374	C-H deformation in CH_3
	1333	O-H plane deformation in COOH
	1262	=C-H deformation (over tone)
	1219	C-COO^- stretching
1114	1106	C-O stretching, NH_3 rocking
850	862	O–H out-of-plane deformation
772	762	CH_2 rocking
649	661	O-C = O in plane deformation
	567	COO^- wagging

The transmission spectrum of LALM crystal was recorded in the range 200–1200 nm is shown in **Figure 4**. A sample of thickness 2mm was used to record the transmission spectrum. The crystal possesses 75 % transmittance and the lower cutoff is found to be as low as 320 nm, allowing for frequency conversion down to UV-region which account for the suitability of this material for optoelectronics applications and the second and third harmonic generation of Nd:YAG fundamental.

The powder second harmonic generation (SHG) test was carried out for LALM using Kurtz and Perry technique. Powdered sample of LALM was tightly packed in the micro capillary tubes of uniform diameter (1.5 mm) and irradiated by an incident laser radiation 1064 nm of pulse width 8 ns and pulse energy of 10–800 mJ from a Q-switched quanta ray of Nd:YAG laser. KDP was used for calibrating the SHG intensity. The second harmonic nonlinearity of LALM was confirmed by the emission of green radiation (532 nm) by the crystal. The powder SHG efficiency of LALM was found to be 1.2 times that of the standard KDP. This confirms that the LALM has higher SHG efficiency than the relative efficiencies of L-alanine (0.2) and L-alanine acetate (0.3) with respect to KDP [15].

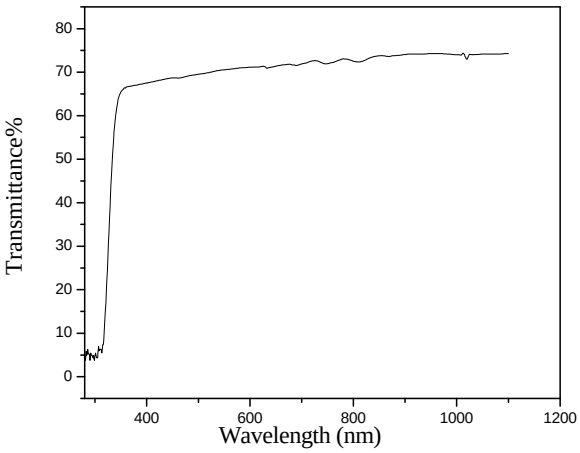

Figure 4. Optical transmittance spectrum of LALM crystal.

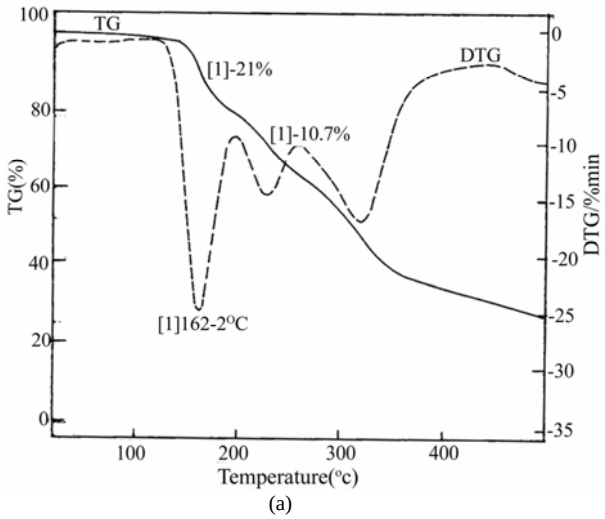

(a)

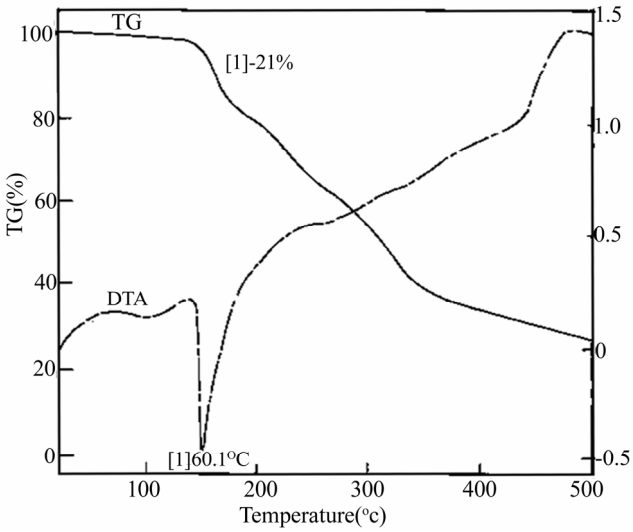

(b)

Figure 5. (a) TG / DTG curves of LALM; (b) DTA/ TG curves of LALM.

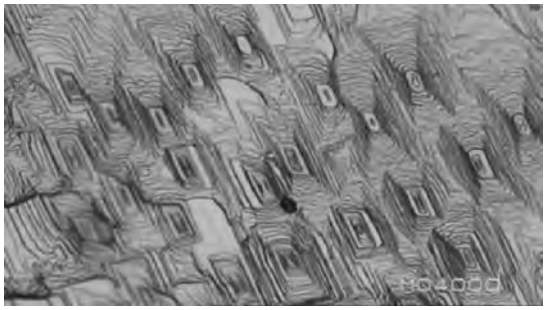

(a)

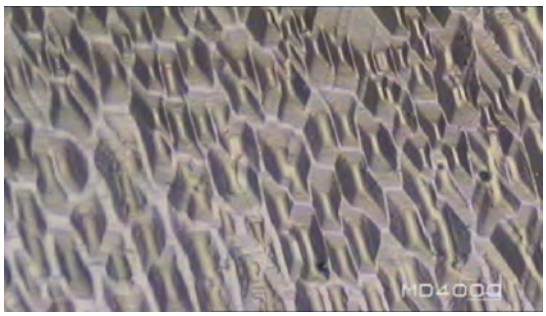

(b)

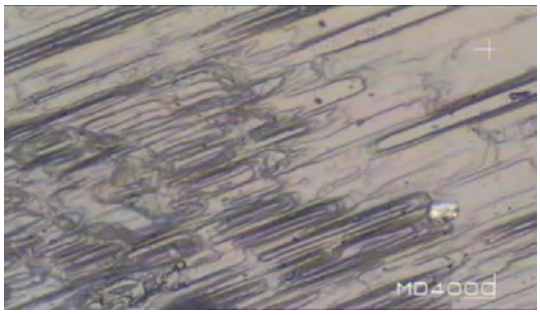

(c)

Figure 6. Etch patterns obtained on (011) of LALM-crystal for different etchants. (a) Water; (b) Methanol ; (c) Ethanol.

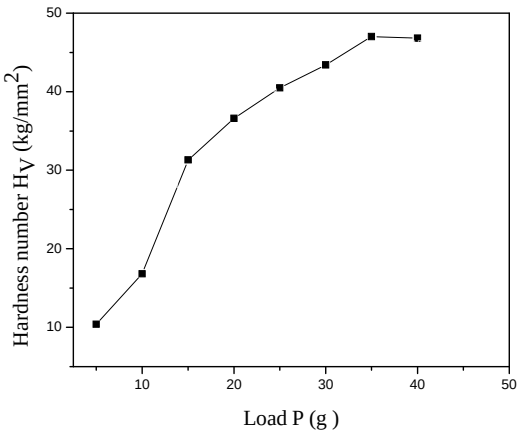

Figure 7. Load (P) Vs Hardness number (Hv) of LALM crystal.

Simultaneous thermo-gravimetric analysis (TG) and differential thermal analysis (DTA) were carried out for the as-grown LALM crystals to study the thermal stability. The characteristic curves are shown in **Figure 5a** and **5b**. Finely powdered crystal was used for the TG/DTA analysis in the temperature range of 26 to 500 °C with a heating rate of 5 °C/min. The alumina (Al_2O_3) crucible was used as a reference for the sample. A weight loss of 21% occur at 162 °C in TGA corresponds to the decomposition range of LALM. An endothermic peak observed at 160 °C in DTA is attributed to the utilization of thermal energy to overcome the valence bonding between the alaninium cation and the maleate anion, which happens during the initial stage of decomposition. As the temperature is increased further, maleic acid decomposes and becomes anhydride and results in the further release of CO_2 and CO molecules at 205 and 258 °C, which is evident from the DTG. The reactions of simplest amino acids induced by heating include the condensation reactions of carboxyl and amino groups leading to the formation of peptide bonds. In the dehydration at the initial stage, H_2O molecule is not liberated immediately; instead, it is absorbed by alumina, which acts as a catalyst, and then is released along with another water molecule obtained from the decomposition of alanine at 320°C. Because of this, an endothermic effect is noted in DTA. CO and CH_4 molecules are liberated at around 450°C.

The NLO efficiency of the grown crystals mainly depends on their optical quality, because the segregated impurities and dislocations occurring during the growth results in the distortion of the optical beam to be processed. In the present investigation, grown crystal of LALM was subjected to chemical etching to study the microstructural imperfection or crystal defects in the grown crystal. A thin plates of 3 mm thickness parallel to {0 1 1} face were cut from the as grown crystal of LALM with the help of a wet thread. Polishing of the surfaces was carried out using soft felt-cloth wetted with ethanol and tertiary butanol mixture (3 : 1). Polished plates of 2 mm in thickness, free from visible inclusions or cracks were selected for etch pit study. Etchants employed to reveal dislocations are taken in homologous series of alcohols i.e. water, methanol and ethanol. Etching of the surfaces was carried out by dipping the plates in etchants for few seconds to few minutes at room temperature and then wiping them with dry filter paper. Etch patterns were observed and photographed under an optical (Carl-Zesis Jenavert) microscope in the reflected light. Elongated circular etch pits were observed when LALM single crystal was etched with water for five seconds as shown in **Figure 6a**. There was no change in etch pit dimension and density with varying etching time (10–20 s). Trapezoid etch pits were observed as shown in **Figure 6b** when LALM single crystal was etched with methanol for five seconds. Rectangular etch pits were observed when the crystal was etched with ethanol for fifteen seconds as shown in **Figure 6c.** From the results of etching behavior of different etchants on LALM crystals, it is inferred that all the organic solvents used in this experiment have successfully revealed the presence of dislocation in the crystal. The observed etch pits, due to layer growth, confirmed the two dimensional (2D) nucleation mechanism with less dislocations. Fast dissolving etchant like water produces better contrasting dislocation etch pits of all surfaces and hence it is intensive to surfaces orientation.

Hardness value on the (011) of LALM crystal was estimated for different loads. The relation between hardness number (Hv) vs load (P) for LALM is shown in **Figure 7**. At lower loads, hardness is relatively lower and it increases for higher loads and remains constant up to 40g. Above 40g, a significant cracking occurred due to the release of internal stress generated locally by indentation. It has been observed that the hardness values of LALM are comparable with pure L-alanine.

4. CONCLUSIONS

A new organic optical material for second order NLO applications, L-alanine maleate (LALM) was synthesized. Single crystals were grown and characterized by X-ray diffraction (single crystal XRD) to confirm the formation of the crystalline phase. FT-IR spectroscopic analysis confirms the presence of all the functional groups in the crystal lattice. Etching studies were carried out for LALM crystal using various etchants. Mechanical behavior of grown crystal was studied on (011) using micro hardness measurement and the hardness values are found to be comparable with pure L-alanine. TG-DTA studies reveal that the material starts decomposing at 162.2 ^{o}C. The UV-Vis spectrum establishes the good transmittance window and the lower cutoff are found to be as low as 320 nm, allowing for frequency conversion down to UV-region. From the Kurtz-Perry powder technique, the second harmonic generation efficiency of the grown LALM crystal was found to be 1.2 times that of KDP crystal.

REFERENCES

[1] N. B. Singh, T. Henningsen, R. H. Hopkins, R. Mazelsky, R. D. Hamacher, E. P. Supertzi, F. K. Hopkins, D. Zelmon, and E. O. P. Singh, (1993) Nonlinear optical characteristics of binary organic system. J. Cryst. Growth, **128**, 976-980.

[2] D. S. Chemla and J. Zyss, (1987) Nonlinear optical properties of organic molecules and crystals. **1** & **2**, Academic Press, New York.

[3] J. Badan, R. Hierle, A. Perigaud, J. Zyss, and D. J. Williams, (1993) Nonlinear optical properties of organic

molecules and polymeric materials. American Chemical Society, Washington, DC, American Chemical Sym- posium Series, **233**.

[4] R. Rajasekaran, P. M. Ushasree, R. Jayavel, and P. Ramasamy, (2001) Growth and characterization of zinc thiourea chloride (ZTC): A semiorganic nonlinear optical crystal. J. Cryst. Growth, **229**, 563-567.

[5] D. Xu, M. Jiang, and Z. Tan, (1983) A new phase matchable nonlinear optical crystal L-arginine phosphate monohydrate, Acta Chem.Sinica, **41**, 570-573.

[6] E. Espinosa, B. Wyncke, F. Bréhat, X. Gerbaux, S. Veintemillas, and E. Molins, (1997) Infrared vibrational spectra of L-histidinium dihydrogen orthophosphate orthophosphoric acid (LHP). Infrared Physics & Technology, **38**, 449-458.

[7] D. R. Babu, D. Jayaraman, R. M. Kumar, G. Ravi, and R. Jayavel, (2003) Growth aspects of semi-organic nonlinear optical L-arginine tetrafluoroborate single crystals, Journal of Crystal Growth, **250**, 157-161.

[8] D. R. Babu, D. Jayaraman, R. M. Kumar, and R. Jayavel, (2002) Growth and characterization of non-linear optical L-alanine tetrafluoroborate (L-AlFB) single crystals, J. Crystal Growth, **245**, 121-125.

[9] C. Razzetti, M. Ardoino, L. Zanotti, M. Zha, and C. Paorici, (2002) Solution growth and characterisation of l-alanine single crystals. Cryst. Res. Technol, **37**, 456-465.

[10] R. Muralidharan, R. Mohankumar, R. Jayavel, and P. Ramasamy, (2003) Growth and characterization of L-arginine acetate single crystals: A new NLO material. J. Cryst. Growth, **259**, 321-325.

[11] R. M. Kumar, D. R. Babu, D. Jayaraman, R. Jayavel, and K. Kitamura, (2005) Studies on the growth aspects of semi-organic l-alanine acetate: A promising NLO crystal, J. Crystal Growth, **275**, 1935-1939.

[12] S. A. Natarajan, S. M. Britto, and E. Ramachandran (2006) Growth, thermal, spectroscopic, and optical studies of l-alaninium maleate, a new organic nonlinear optical material. Crystal Growth & Design, **6(1)**, 137-140.

[13] M. N. G. James and G. J. B. Williams, (1974) A refinement of the crystal structure of Maleic Acid. Acta Cryst. **B30**, 1249-1257.

[14] K. Nakamoto, (1970) Infrared spectra of inorganic and coordination compounds. Wiley-Interscience, New York, **233**.

[15] D. R. Babu, (2003) Ph.D Thesis, University of Madres, India.

Vol.1, No.3, 222-228 (2009)
doi:10.4236/ns.2009.13030

Natural Science

Control strategy optimization using dynamic programming method for synergic electric system on hybrid electric vehicle

Yuan-Bin Yu, Qing-Nian Wang, Hai-Tao Min, Peng-Yu Wang, Chun-Guang Hao

The State Key Laboratory of Automobile Dynamic Simulation, JiLin University, Changchun, China

Received 23 August 2009; revised 27 September 2009; accepted 22 October 2009.

ABSTRACT

Dynamic Programming (DP) algorithm is used to find the optimal trajectories under Beijing cycle for the power management of synergic electric system (SES) which is composed of battery and super capacitor. Feasible rules are derived from analyzing the optimal trajectories, and it has the highest contribution to Hybrid Electric Vehicle (HEV). The methods of how to get the best performance is also educed. Using the new Rule-based power management strategy adopted from the optimal results, it is easy to demonstrate the effectiveness of the new strategy in further improvement of the fuel economy by the synergic hybrid system.

Keywords: Dynamic Programming; Control Strategy; Optimization; Synergic Electric System; HEV

1. INTRODUCTION

Hybrid Electric Vehicle (HEV) could improve fuel economy and exhaust emission using the electric system to adjust the load of engine and could make it work in high efficiency. But this depends on the performance of the electric system on board. Because of the low power density of battery, it's hard to be competent for this purpose. When it was combined with super capacitor to form a new electric system which was called the Synergic Electric System (SES), could exert both merits, which is energy and power density [1,2].

Rule-based or fuzzy logic control strategy was used to supervise the power flow between the two parts at present [3,4]. For every state of the SES, each control will come to a new state，at the same time, we can get a loss of energy. With regard to a given cycle of motor power requirement, how to get the best control rate has been put to us which can achieve the optimal performance of the system. Dynamic Programming is a numerical methodology developed for solving sequential or multi-stage decision problems just like the SES. The algorithm searches for optimal decisions at discrete points in a time sequence. It has been shown to be a powerful tool for optimal control in various application areas [4,5,6,7]. The dissertation proposed the dynamic programming algorithm from optimum control theory which solve the problem of overall control rate for SES in the whole cycle and try to answer the question like what can SES do on energy-saving.

2. BRIEF INTRODUCTION OF SES CONFIGURATION AND RULE-BASED CONTROL ALGORITHM

A hybrid city bus was chosen as a researching flat, and the SES was made up of 280 Nickel-Hydrogen batteries units (1.2V\15Ah each) and 120 super capacitors (2.5V \2000F each). A Buck/ Boost DC/DC power converter whose Peak / rated power were 60/30kw was used in this system to coordinate the voltage of battery and capacitor, and to control the current of capacitor actively. **Figure 1** was the layout of SES in this research.

Control objective of SES was as follow: ensure the vehicle's dynamic as the premise and give full play to the super capacitor's "push and pull" role; decrease large current's impact; extent battery's service life; regenerate braking energy as much as possible to improve fuel

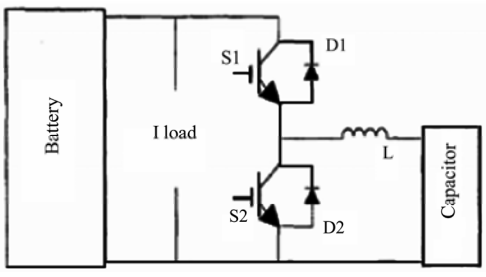

Figure 1. Topology of Buck/Boost DC/DC Converter.

economy. The principle of the rule-based control strategy is: During the operation, battery provides the average power requirement; capacitor will give a complement. The control rule was as follow:

1) if $P_m<0$, and super capacity was not over charged, then $P_{bat}=0$;

2) or if $P_m<P_{bat\_max}$, and super capacity was not over discharged, then $P_{bat}=P_{filter}$、$P_{scap}=P_m-P_{filter}$;

3) otherwise $P_{bat}=P_m$;

4) when super capacity run out of energy, charge the capacitor from battery, $P_{bat}=P_{chg}+P_{bat}$.

The variables' meanings above are: P_m——the power required from motor, P_{bat} ——batteries' power needed from motor, P_{scap} ——capacitor's power requirement, P_{filter}——filtering power, which is calculated by **Formula (1)**.

$$P_{filter}=P_m \bullet H_{LP}'=P_m \bullet \left(1-e^{-\frac{t}{\tau'}}\right)$$
$$=P_{load} \bullet e^{-\frac{t}{\tau}} \bullet \left(1-e^{-\frac{t}{\tau'}}\right) \quad (1)$$

In the formula: P_{load}——road resistance; H_{LP}——filter function; τ、τ'——engine and battery's low-pass filter time constant; t——acceleration time; P_m——motor power required; P_{chg}——charge power from battery when capacitor's state of charge (CSOC) is low. It is the function of battery's state of charge (SOC) and is equal to P_{bat_max}*（$SOC-SOC_{min}$）/ ($SOC_{max}-SOC_{min}$).

The capacitor's electrical-quantity shortage is determined by the demand. When the actual voltage of capacitor is lower than the ideal voltage, it is calculated out according to vehicle speed as **Formula (2)**. The dissertation provides that the ideal voltage limit is in a reverse proportion with vehicle speed. The object of setting this value is to develop a goal of electrical-quantity for capacitor, which could ensure that it could preserve enough energy for acceleration when vehicle speed is in the formula: V_{scap}——capacitor's actual voltage of low and regenerate enough braking energy capacity. When vehicle speed is high. The speed requirement of the vehicle, the current of single battery, current of SES's battery and capacitor according to rule-based control strategy are shown in **Figure 2**.

$$\frac{V_{scap}}{V_{scap}^{\max}}=\sqrt{1-k\left(\frac{v_{car}}{v_{car}^{\max}}\right)^2} \quad (2)$$

In the formula: capacitor; $V_{scap}^{\max}$ ——capacitor's maximum voltage; v_{car}——actual vehicle speed; $v_{car}^{\max}$ ——maximum vehicle speed; k——capacitor's energy utilization rate in cycle, in value equivalent to 0.75;

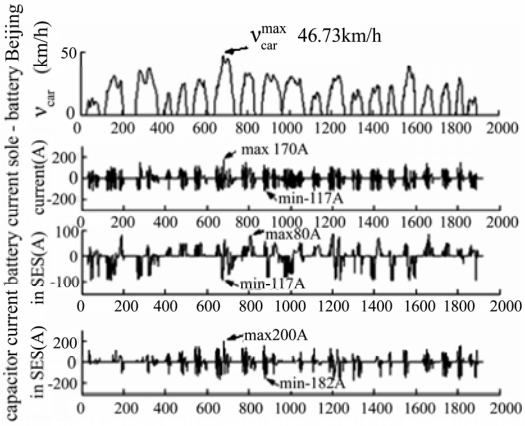

Figure 2. Simulation results under Beijing cycle.

3. BRIEF INTRODUCTION OF DYNAMIC PROGRAMMING CONTROL ALGORITHM

Dynamic programming is a kind of math method solving the optimal problem in process of multi-stage decision. It is proposed and established in the Fifties of 20th Century by American mathematicians (Bellman) who claim the famous Optimum Theory and transmit the process of multi-decision into a serious of single-stage issue. Multi-stage problem is a kind of activities which could be divided into several interrelated stages. Each stage needs a decision. The decision not only decides the benefit of this stage but also the initial state of next stage. A sequence of decisions would be created after every stage's decision has been made. The multi-stage decision problem is to get a control strategy that can optimize the sum of every stage's benefit [3]. Dynamic programming algorithm can fully utilize the limited resources which is an important content of investment-determination. As for multi-stage determination problem, dynamic programming method could be used to make sure the sum of benefit from every stage optimal [4].

4. DESCRIPTION OF PROBLEM OF OPTIMIZATION CONTROL ALGORITHM

The power requirement of motor at every moment is fulfilled by battery and ultra capacitor. However, because of the difference between the resistance and the efficiency of charge and discharge, every decision made by system at every moment will create impact on the whole control effect. For the power requirement of motor is consist of the power of battery and ultra capacitor at any proportion. So relationship of the power of battery and ultra capacitor is:

$$P_{bat}+P_{scap}=P_m \quad (3)$$

Every moment, the battery and ultra capacitor in the SES have the corresponding SOC and CSOC which represent the state X of battery and ultra capacitor. When the power flow through battery and ultra capacitor, it can create an incentive to change the state of the two power source, at the same time can create power loss J. According to the experiment result of component's character, the resistances of battery and ultra capacitor are functions of SOC and CSOC and different system loss would be created under different control rate U. Thus, conclusions can be drawn that system's power loss J, at the same time J is the function of state object X and control rate U. Recursive equation of X and power loss equation can be expressed by **Formula (4)**.

$$x(k+1)=f(x(k),u(k))$$

$$J_{loss}^{system}=L(x(k),u(k))$$

$$=P_{loss}^{bat}(x(k),u(k))+P_{loss}^{Scap}(x(k),(1-u(k)))+P_{loss}^{DC/DC}(1-u(k)) \quad (4)$$

Under given driving cycle, the power requirement from motor can be drawn, then the system's loss on this moment was only decided by the two parts' state X and the chosen control rate U. From this moment on, different power requirement Pm and control rate U will create different state X and confront with the problem of choosing a new control rate till the end of the cycle. Because the initial condition of vehicle simulation has been decided, the problem of optimum control rate on SES can be attributed to: Free optimal control issues on certain initial condition x(0)=x, as shown in **Figure 3.**

It is considered that the changes of battery's state will have a certain influence on the power loss effect. So, when calculating the value of J, battery and capacitor's electrical-quantity state G should be fully considered. Calculation of G showed in **Formula (5)**.

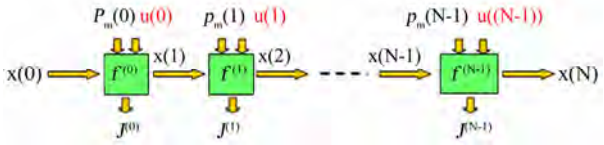

Figure 3. Recursive of system's state and control object.as shown in **Formula (6)**.

$$G=G_{bat}+G_{Scap}=E_{max}^{bat}(SOC(K+1)-SOC(K))+E_{max}^{Scap}(CSOC(K+1)-CSOC(K)) \quad (5)$$

5. OBJECT OF THE OPTIMIZATION

If every control rate in the cycle is given properly, the sum of power loss at every moment will decrease to the minimum. Under the same cycle power requirement, it can be seen as the best cycle power efficiency, the biggest regenerate of braking energy and the best performance of power. Consequently, optimal goal could be set

$$\min J=\min\left(\sum_{k=0}^{k=N-1}\left(L(x(k),u(k))-G\right)\right) \quad (6)$$

6. CONSTRAINTS

In cycle, the charge and discharge power and the energy of batteries and capacitors must subject to the limitation of **Formulas (7)** and **(8)**.

$$P_{bat\,min}\le P_{bat}(t)\le P_{bat\,max}$$

$$E_{bat\,min}\le E_{bat}(t)\le E_{bat\,max} \qquad \forall t\in[0,T] \quad (7)$$

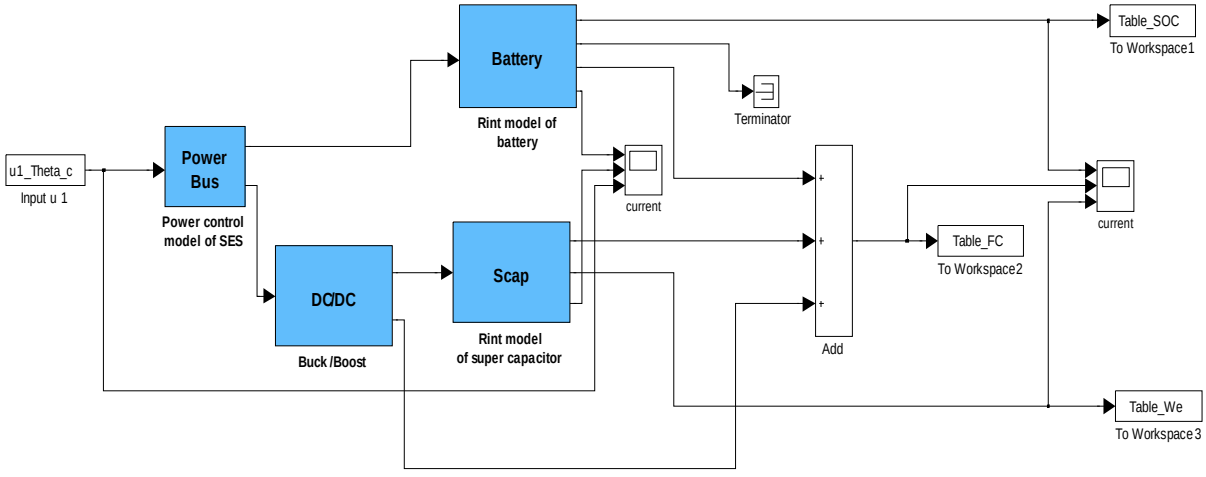

Figure 4. Solving model of synergic system.

Table 1. Optimal solution of synergic system's energy loss at the 126th sec of Beijing cycle J1* e+005.

Soc csoc	0.4	0.45	0.5	0.55	0.6	0.65	0.7	0.75	0.8
0.5	9.9952	9.936	9.873	9.8693	9.8659	9.8745	9.883	9.942	10
0.55	9.982	9.9229	9.8602	9.8567	9.8535	9.8619	9.870	9.929	9.98
0.6	9.971	9.912	9.8495	9.846	9.8414	9.8485	9.855	9.915	9.97
0.65	9.9574	9.8966	9.829	9.8232	9.8177	9.8248	9.832	9.891	9.94
0.7	9.9464	9.86	9.7929	9.7871	9.7758	9.7829	9.790	9.849	9.90
0.75	9.9233	9.86	9.7929	9.7871	9.7817	9.7888	9.796	9.855	9.91
0.8	9.9175	9.8541	9.787	9.7812	9.7758	9.7829	9.790	9.849	9.90
0.85	9.8935	9.8152	9.7489	9.7432	9.7378	9.7449	9.752	9.810	9.86
0.9	9.8777	9.8152	9.7489	9.7432	9.7378	9.7449	9.752	9.810	9.86
0.95	9.8615	9.7988	9.7325	9.7269	9.7216	9.7286	9.735	9.794	9.85
1	9.8545	9.7922	9.7262	9.7206	9.7153	9.722	9.729	9.787	9.84

Table 2. Optimal control rate at the 126th sec of Beijing cycle U1.

Soc csoc	0.4	0.45	0.5	0.55	0.6	0.65	0.7	0.75	0.8
0.5	6	6	6	6	6	6	6	6	6
0.55	5	5	5	5	5	5	5	5	5
0.6	4	4	4	4	4	4	4	4	4
0.65	3	3	3	3	3	3	3	3	3
0.7	2	2	2	2	2	2	2	2	2
0.75	1	1	1	1	1	1	1	1	1
0.8	6	6	6	6	6	6	6	6	6
0.85	6	6	6	6	6	6	6	6	6
0.9	6	6	6	6	6	6	6	6	6
0.95	5	5	5	5	5	5	5	5	5
1	5	5	5	5	5	5	5	5	5

Table 3. Optimal solution of synergic system's energy loss at the 127th sec of Beijing cycle J1* e+005.

Soc csoc	0.4	0.45	0.5	0.55	0.6	0.65	0.7	0.75	0.8
0.5	9.9914	9.9318	9.8686	9.865	9.8617	9.8702	9.8787	9.9383	9.9964
0.55	9.9866	9.9275	9.8645	9.8608	9.8574	9.866	9.8746	9.9342	9.9919
0.6	9.9731	9.914	9.8514	9.8479	9.8447	9.8531	9.8616	9.9208	9.9784
0.65	9.9618	9.9028	9.8403	9.8368	9.8322	9.8393	9.8465	9.906	9.964
0.7	9.9478	9.887	9.8194	9.8135	9.808	9.8152	9.8224	9.8817	9.9395
0.75	9.9361	9.9361	9.8046	9.7987	9.7933	9.8004	9.8076	9.867	9.9248
0.8	9.9124	9.8491	9.782	9.7762	9.7708	9.7779	9.7851	9.8441	9.9015
0.85	9.8888	9.825	9.7576	9.7518	9.7463	9.7535	9.7608	9.82	9.8777
0.9	9.8731	9.8106	9.7444	9.7387	9.7333	9.7404	9.7476	9.8601	9.8629
0.95	9.8572	9.7946	9.7283	9.7226	9.7173	9.7244	9.7315	9.79	9.8469
1	9.8505	9.7882	9.7222	9.7166	9.7113	9.7183	9.7254	9.7838	9.8405

Table 4. Optimal control rate at the 127th sec of Beijing cycle U1.

Soc csoc	0.4	0.45	0.5	0.55	0.6	0.65	0.7	0.75	0.8
0.5	8	8	8	8	8	8	8	8	8
0.55	7	7	9	9	9	9	9	7	7
0.6	7	7	7	7	7	7	7	7	7
0.65	7	7	7	7	7	7	7	7	7
0.7	8	8	8	8	8	8	8	8	8
0.75	8	8	8	8	8	8	8	8	8
0.8	7	7	7	7	7	7	7	7	7
0.85	7	7	7	7	7	7	7	7	7
0.9	6	6	6	6	6	6	6	6	6
0.95	5	5	5	5	5	5	5	5	5
1	5	5	5	5	5	5	5	5	5

$$P_{scap\,min} \le P_{scap}(t) \le P_{scap\,max}$$

$$E_{scap\,min} \le E_{scap}(t) \le E_{scap\,max} \qquad \forall t \in [0,T] \tag{8}$$

In the **Formula (7)** and **(8)**, P and E are the power require from battery and capacitor, the max and min are the maximum and minimum value respectively.

7. ALGORITHM SOLVING

1) Model for System Solving

Figure 4 shows the solving model of SES under dynamic programming. From the initial moment according to the model established, the algorithm calculates out every moment's system loss and stored them in memory. The code of this program is:

table_x1_n(a,b,c)=Table_CSOC(2); table of CSOC
table_x2_n(a,b,c)=Table_SOC(2); table of SOC
table_u1_n(a,b,c)=u1_Theta_c; control rate table
FC_inst(a,b,c)=Table_FC(2); power loss table

2) Algorithm Solving

Making use of the result in the last section, start from the terminal, calculate the value-added power loss of the current and the last moment in sequence and find out the minimum point according to the reverse deducing method using the min function of MATLAB language. Record every moment and state's minimum value of J and the corresponding optimal control rate u and store them in matrix J1 and U1 respectively. The calculating program is:

```
a=interp2(x2_SOC_grid,x1_We_grid,FC_interp,table
_x2_n(:),table_x1_n(:),'nearest'); %sum of the past b =
reshape
(FC_inst(:)+a,N_x1_We,N_x2_SOC,N_u1_Theta);
%sum of the past and current
%FC_inst(:) every moment's power loss
%find out the optimal solve from the first step to the
current step using min function
[J1(:,:),U1(:,:)] = min(b,[],3); %find the optimal solve
and the corresponding u1
%for J1: x represent SOC and y represent CSOC,
volume is the system's power loss
%reverse calculation
%U1 store the optimum control rate u1.
```

Based on the object of optimization, the minimum power loss of any moment and the moment behind can

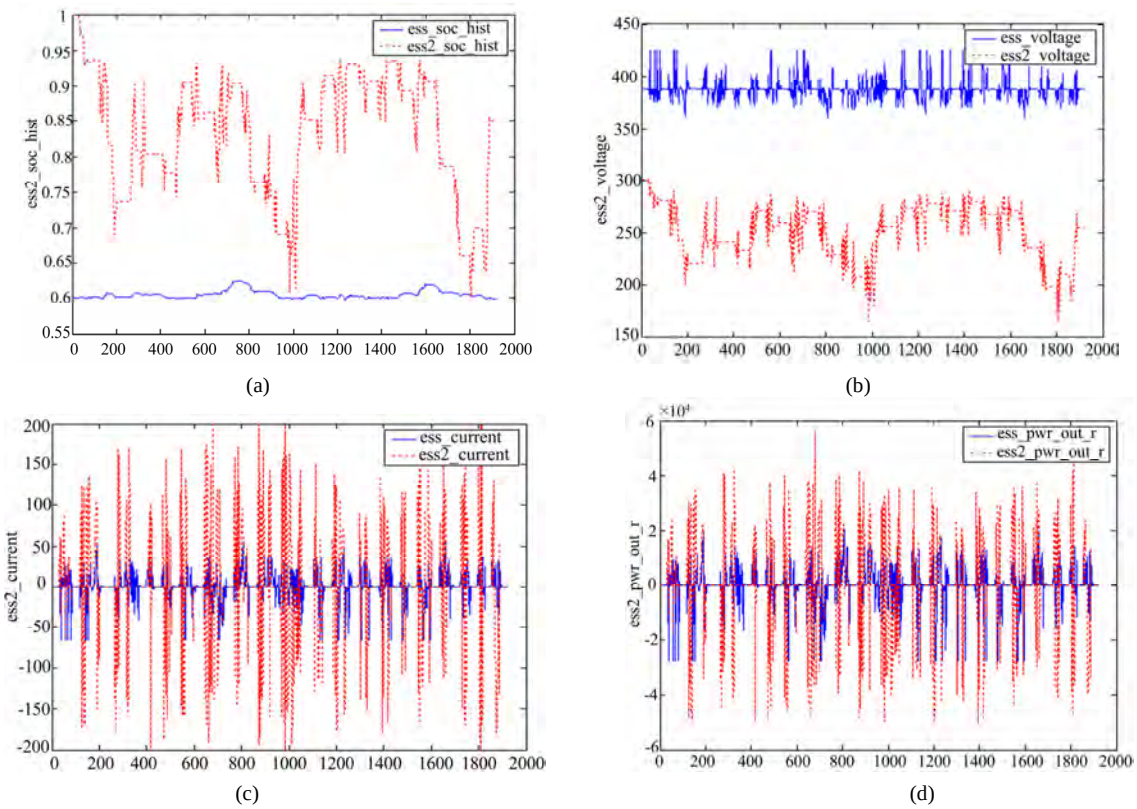

Figure 5. Optimum solution of synergic system's dynamic programming under Beijing cycle（battery—ess、capacitor—ess2. (a) electrical-quantity state of battery and capacitor; (b) voltage process of battery and capacitor; (c) current distribution of battery and capacitor; (d) power distribution of battery and capacitor.

be calculated out under the reverse method and stored in J1. At the same time, the optimum control rate is stored in U1.Under Beijing cycle, the electrical power requirement of the 126th sec and the 127th sec is -16859w and 37467w. **Table 1** to **4** list out the optimum solve J1 and optimum control rate U1, and from which, the trend and principle of controlling can be induced.

As is shown from the data, if the SOC and CSOC of battery and super capacitor at some moment are known, then the optimum solution J1 and optimum control rate U1 can be checked up from tables above. After known about the point's power demand Pm and the optimum control rate U1, the SOC and CSOC of battery and super capacitor on the next moment can be calculated out through every parts model, and then continue to look-up tables to find out the optimum solution and optimum control rate. Followed by analogy, on the situation when the forward calculation mode. Connect every moment's optimal control rate, the optimum control rate of SES under Beijing cycle can be drawn approximately. During calculation, if the less interval of every component's state and control rate were used, the closer the result to the synergic system's optimal control rate.

In this way, under Beijing cycle, divide the battery's SOC from 0.4 to 0.8 into 9 parts. The interval of each calculation point is 0.05. Divide the capacitor's CSOC from 0.5 to 1 into 11parts to ensure that the same interval of calculation point is chose. After optimized calculation, the optimal control rate can be counted out shown in **Figure 5**. **Figure 5a** illustrates the SOC of battery and capacitor resulted from the optimized control under Beijing cycle. **Figure 5b** shows the voltage process of battery and capacitor resulted from optimum control. Figure (c&d) illustrate the current and power distribution resulted from the optimum control rate at every moment respectively.

3) Improved Rule-based Control Strategy

The result is based on cycle, so the Dynamic Programming algorithm can be not directed applied to engineering control. However, some enlightening can be drawn used as the guidance of actual control algorithm programming. For example, based on the result of previous section, the following four laws can be educed:

a).During power assisting, if the motor required a low current, the battery would provide the power.

b).During power assisting, the capacitor should provide more power when the motor is under high power demand.

The two tips above are all induced by the low efficient of DC/DC under low load.

c).If the capacitor is in high CSOC, and then it should share a greater proportion of discharge. However, as the CSOC drops, the discharge proportion of capacitor would diminish responsively, while battery's proportion would increase gradually till the battery pack power the motor alone.

d).When low-power braking, capacitor can recovery all the vehicle braking energy; While, with the increase of braking power, collaborative work mode of battery and capacitor would be taken by the optimized control algorithm to make the two both working on a high efficiency and contribute to the balance of battery. Also the proportion of discharge from capacitor would increase as the braking power increase. This is different from the rule of rule-based control strategy that energy firstly go to the capacitor and it gives inspiration for the improvement of control strategy.

Based on the analysis above, this section proposed a modification on rule-based control strategy of SES when motor power assisting and braking energy regeneration. Details as follows:

(1) When power assisting, if $P_m>0$, and $P_m<P_{set}$, then $P_{bat}=P_m$;

(2) Otherwise, if $P_m>P_{set1}$, then $P_{scap}=K_1*P_m$, but $P_{bat}=(1- K_1) *P_m$; in the formula: K_1 is the function of capacitor's CSOC showed in table 5. P_{set1}=12.33kw.

(3) When braking: if $P_m<0$, and $P_m>P_{set2}$, capacitor is not over recharged, then $P_{bat}=0$; otherwise when $P_m<P_{set2}$, $P_{scap}=K_2*P_m$, and $P_{bat}=(1- K_2) *P_m$, K_2 increases as P_m decreases.P_{set2}=8.7kw.

Figure 6 shows working process manipulate of SES's control rate, battery and capacitor resulted from the simulation of rule-based control strategy, which is modified by applied optimal algorithm. **Table 6** lists comparison of SES's HEV simulation result under different control algorithm. Conclusions can be drawn from the various SES's simulation results listed in the table, that HEV vehicle have optimum fuel economy under control of dynamic programming algorithm. Using the principle of optimized DP algorithm, designer could know the maximum energy-saving efficient contributed by SES and also could compile optimal control algorithm of SES, which can be used in actual engineering. Under this cir-

Table 5. Relationship between Ki and CSOC.

CSOC	0.5	0.6	0.7	0.8	0.9	1.0
K_1	0	0.2	0.4	0.6	0.8	1.0

Table 6. Simulation result comparison of synergic system.

Control strategy	Rule-based	Dynamic programming	Improved rule-based
Fuel economy（L/100km）	25.7	23.2	24.5
Fuel economy improvement	1	↑2.1%	↑1.6%
Power efficiency	87%	93%	91%
Brake energy recovery efficient	8.34%	9.74%	9.35%

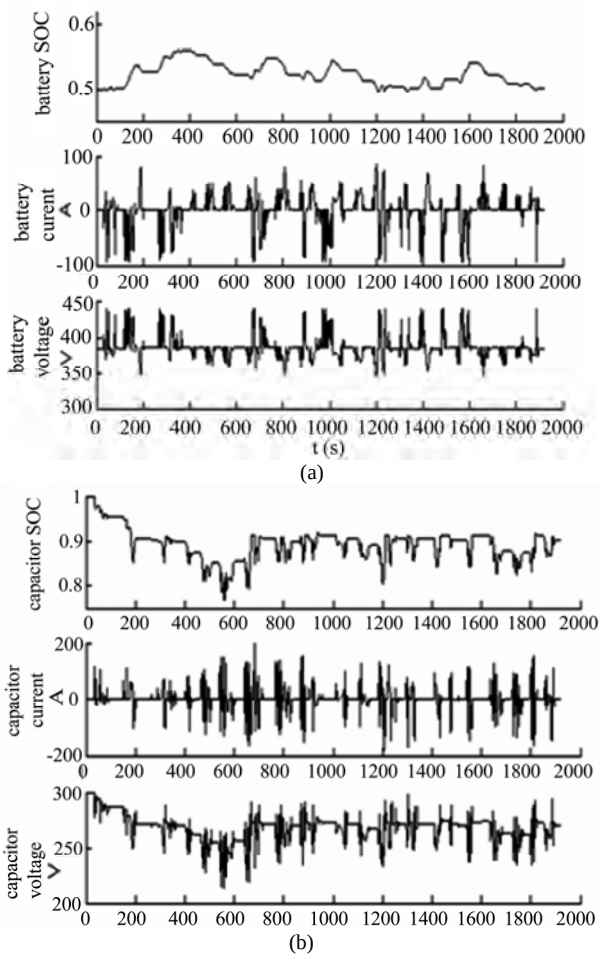

Figure 6. Simulation result based on the optimized rule-based control strategy under Beijing cycle; (a) SOC, current and voltage of battery; (b) CSOC, current and voltage of capacitor.

cumstance,capacitor can keep appropriate power state at anytime and make vehicle fuel consumption a further reduction. All the advantages above can prove the significance improvement by dynamic programming optimization algorithm

8. CONCLUSIONS

1) Dynamic programming algorithm had been applied to SES to find out the optimum control rate using off-line simulation.

2) Rule-based control algorithm was established based on the optimum control rate. The simulation results demonstrated that the method is practical and effective.

3) Based on the control rules of overall optimized algorithm, the rule-based control strategy of the SES had been improved and the control effect had also been evaluated. The dissertation explicated the best performance and most efficient control method of SES which could make the best contribution to vehicle energy-saving.

4) The overall optimized principle was suitable for the programming and optimizing of control algorithm for HEV vehicle with multi-energy power source.

REFERENCES

[1] T. Markel, M. Zolot, K. B. Wipke, and A. A. Pesaran, (2003) Energy storage system requirement for hybrid fuel cell vehicles. Advanced Automotive Battery Conference, Nice, France, June. 10-13.

[2] A. C. Baisden and A. Emadi, (2004) ADVISOR-based model of a battery and an ultra capacitor energy source for hybrid vehicles. IEEE Transactions on Vehicular Technology, **53(1)**.

[3] Y. B. Yu and Q. N. Wang, (2005) The redevelopment of synergy electric power HEV simulation software based on advisor. Jilin Daxue Xuebao (Gongxueban) /Journal of Jilin University (Engineering and Technology Edition), **35(4)**, 353-357.

[4] Y. B. Yu and W. H. Wang, (2007) The research on fuzzy logic control strategy of synergic electric system of hybrid electric vehicle. SAE Internatioal, 07APAC-185.

[5] D. P. Bertsekas, (1995) Dynamic programming and optimal control, Athena Scientific.

[6] J. M. Kang, I. Kolmanovsky, and J. W. Grizzle, (1999) Approximate dynamic programming solutions for lean burn engine aftertreatment. proceedings of the IEEE conference on decision and control, **2**, Piscataway, NJ, 1703-1708.

[7] C. Lin, J. Kang, J. W. Grizzle, and H. Peng, (2001) Energy management strategy for a parallel hybrid electric truck. Proceedings of the 2001 American Control Conference, Arlington, VA, 2878-2883.

[8] M. P. O'Keefe and T. Markel, (2006) Dynamic programming applied to investigate energy management strategies for a plug-in HEV. The 22nd International Battery, Hybrid and Fuel Cell Electric Vehicle Symposium and Exhibition (EVS-22), Yokohama, Japan, October 23–28.

[9] L. V. P´erez and G. R. Bossio, (2006) Optimization of power management in an hybrid electric vehicle using dynamic programming. Mathematics and Computers in Simulation, **73**, 244–254.

Vol.1, No.3, 229-233 (2009)
doi:10.4236/ns.2009.1303

Natural Science

Focal shift of radially polarized bessel-modulated gaussian beam by phase shifting

Xiu-Min Gao[1,2], Ming-Yu Gao[1], Song Hu[1], Han-Ming Guo[2], Jian Wang[1], Song-Lin Zhuang[2]

[1]Electronics & Information College, Hangzhou Dianzi University, Hangzhou, China; xiumin_gao@yahoo.com.cn
[2]Optics & Electronics College, University of shanghai for Science and Technology, Shanghai, China

Received 28 September 2009; revised 23 October 2009; accepted 26 October 2009.

ABSTRACT

Focal shift of radially polarized Bessel-modulated Gaussian (QBG) beam by phase shifting is investigated theoretically by vector diffraction theory. The phase shifting distribution is the function of the radial coordinate. Calculation results show that intensity distribution in focal region can be altered considerably by the topological charge of QBG beam and the phase parameter that indicates the vary degree of the phase shifting along radial coordinate. Topological charge induces the focal shift in transverse direction, while phase parameter leads to the focal shift along optical axis of the focusing system. More interesting, the focal shift may be incontinuous in certain case.

Keywords: Focal Shift; Bessel-Modulated Gaussian Beam; Vector Diffraction Theory

1. INTRODUCTION

Since Caron and Potvliege introduced a novel class of beam expressed in cylindrical coordinate system recently, namely, the Bessel-modulated Gaussian beams with quadratic radial dependence (QBG beam) [1], QBG beam has attracted much attention [2-7]. It was shown that such class of beams has familiar collinear geometry of the Gaussian beam and also an interesting non-Gaussian features for certain values of its parameters [1-3]. Belafhal and Dalil-Essakali studied the propagation properties of QBG beams through a unapertured optical paraxial ABCD system [4]. X. Wang, and B. Lü researched on the beam propagation factor (M^2-factor), far-field distribution, and the kurtosis parameter of such type of beams [3,5,6]. And the Bessel-modulated Gaussian light beams passing through a paraxial ABCD optical system with an annular aperture has also been studied [7]. On the other hand, in the investigation of the focusing properties of optical beams, tracing the movement of the point of absolute maximum intensity along optical axis has attracted many researchers for several decades [8-12]. It was found that the point of absolute maximum intensity does not coincide with the geometrical focus but shifts along optical axis. This phenomenon is referred to as focal shift. More interesting, the focal shift may be incontinuous in certain optical focusing systems.

Almost all QBG beams in above previous papers are in scalar a form, which means the polarization property of optical field is not considered. In fact, the polarization is very important characteristics to alter propagating and focusing properties of beams. For example, laser beam with cylindrical symmetrical polarization have attracted many researchers recently because the electric field in focal region of such cylindrical vector beam has some unique properties [13-16]. The present paper is aimed at studying focal shift of radially polarized QBG beam by vector diffraction theory. The principle of the focusing radially polarized QBG beam with phase shifting is given in Section 2. Section 3 shows the simulation results and discussions. The conclusions are summarized in Section 4.

2. PRINCIPLE OF THE FOCUSING RADIALLY POLARIZED QBG BEAM WITH PHASE SHIFTING

In the focusing system we investigated, focusing beam is radially polarized QBG beam whose value of transverse optical field is same as that of the scalar QBG [1-3], and its polarization distribution turns on radially symmetric [13,14]. Therefore, in the cylindrical coordinate system $(r,\varphi,0)$ the field distribution $\vec{E}(r,\varphi,0)$ of the radially polarized QBG beam at the plane is written as,

$$\vec{E}_0(r,\phi,0) = E_0(r,\phi,0)\cdot\vec{n}_r \qquad (1)$$

where $\vec{n}_r$ is the radial unit vector of polarized direction. Term $\vec{E}(r,\varphi,0)$ is optical field value distribution and can be written in the from [1-5],

$$E_0(r,\phi,0) = B \cdot J_{|m|/2}\left(\frac{\mu r^2}{\omega_0^2}\right)\exp\left(-\frac{r^2}{\omega_0^2}\right)\exp(im\phi) \quad (2)$$

where $J_{|m|/2}$ denotes the Bessel function of order |m|/2, m is the topological charge of QBG beam, ω_0 is the waist width of the Gaussian beam, and μ is a beam parameter which is complex-valued in general. B is a constant. According to vector diffraction, the electric field in focal region of radially polarized QBG beam is [17],

$$\vec{E}(\rho,\varphi,z) = E_\rho \vec{e}_\rho + E_\varphi \vec{e}_\varphi + E_z \vec{e}_z \quad (3)$$

where $\vec{e}_\rho$, $\vec{e}_\varphi$, and $\vec{e}_z$ are the unit vectors in the radial, azimuthal, and propagating directions, respectively. To indicate the position in image space, cylindrical coordinates (ρ,φ,z) with origin $\rho = z = 0$ located at the paraxial focus are employed. E_ρ, E_z, and E_Φ are amplitudes of the three orthogonal components and can be expressed as.

$$E_\rho(\rho,\varphi,z) = \frac{-iA}{\pi}\int_0^\alpha\int_0^{2\pi}\sqrt{\cos\theta}\cdot E_0 \cdot\sin\theta\cos\theta\cos(\phi-\varphi)$$
$$\cdot\exp\left\{ik\left[z\cos\theta+\rho\sin\theta\cos(\phi-\varphi)\right]\right\}d\phi d\theta \quad (4)$$

$$E_\varphi(\rho,\varphi,z) = \frac{-iA}{\pi}\int_0^\alpha\int_0^{2\pi}\sqrt{\cos\theta}\cdot E_0$$
$$\cdot\sin\theta\cos\theta\sin(\phi-\varphi)$$
$$\cdot\exp\left\{ik\left[z\cos\theta+\rho\sin\theta\cos(\phi-\varphi)\right]\right\}d\phi d\theta \quad (5)$$

$$E_Z(\rho,\varphi,z) = \frac{iA}{\pi}\int_0^\alpha\int_0^{2\pi}\sqrt{\cos\theta}\cdot E_0\cdot\sin^2\theta$$
$$\cdot\exp\left\{ik\left[z\cos\theta+\rho\sin\theta\cos(\phi-\varphi)\right]\right\}d\phi d\theta \quad (6)$$

where θ and φ denote the tangential angle with respect to the z axis and the azimuthal angle with respect to the x axis, respectively. k is wave number. α=arcsin(NA) is convergence angle corresponding to the radius of incident optical aperture. In order to make focusing properties clear and simplify calculation process, after simple derivation, **Eq.2** can be rewritten as,

$$E_0(\theta,\phi,0) = B\cdot J_{|m|/2}\left[\frac{\sin^2(\theta)}{w^2\cdot NA^2}\right]$$
$$\cdot\exp\left[-\frac{\sin^2(\theta)}{w^2\cdot NA^2}\right]\cdot\exp(im\phi) \quad (7)$$

where $w = \omega_0/r_0$ is called relative waist width. The phase shifting of the radially polarized QBG beam is the function of radial coordinate and is in the from as,

$$\psi = \pi\cdot\cos\left(C\cdot\frac{\tan\theta}{\tan\alpha}\cdot\pi\right) \quad (8)$$

where C is phase parameter that indicates the vary degree of the phase shifting along radial coordinate. Substitute the **Eq.7** and **Eq.8** into **Eqs.4-6**, we can obtain,

$$E_\rho(\rho,\varphi,z) = \frac{-iAB}{\pi}\int_0^\alpha\int_0^{2\pi}\sqrt{\cos\theta}\cdot\sin\theta\cos\theta$$
$$\cdot\cos(\phi-\varphi)\cdot J_{|m|/2}\left[\frac{\sin^2(\theta)}{w^2\cdot NA^2}\right]\cdot\exp\left[-\frac{\sin^2(\theta)}{w^2\cdot NA^2}\right]$$
$$\cdot\exp(i\psi)\cdot\exp(im\phi)\cdot\exp\left[i\cdot\pi\cdot\cos\left(C\cdot\frac{\tan\theta}{\tan\alpha}\cdot\pi\right)\right]$$
$$\cdot\exp\left\{ik\left[z\cos\theta+\rho\sin\theta\cos(\phi-\varphi)\right]\right\}d\phi d\theta \quad (9)$$

$$E_\varphi(\rho,\varphi,z) = \frac{-iAB}{\pi}\int_0^\alpha\int_0^{2\pi}\sqrt{\cos\theta}\cdot\sin\theta\cos\theta$$
$$\cdot\sin(\phi-\varphi)\cdot J_{|m|/2}\left[\frac{\sin^2(\theta)}{w^2\cdot NA^2}\right]\cdot\exp\left[-\frac{\sin^2(\theta)}{w^2\cdot NA^2}\right]$$
$$\cdot\exp(i\psi)\cdot\exp(im\phi)\cdot\exp\left[i\cdot\pi\cdot\cos\left(C\cdot\frac{\tan\theta}{\tan\alpha}\cdot\pi\right)\right]$$
$$\cdot\exp\left\{ik\left[z\cos\theta+\rho\sin\theta\cos(\phi-\varphi)\right]\right\}d\phi d\theta \quad (10)$$

$$E_Z(\rho,\varphi,z) = \frac{iAB}{\pi}\int_0^\alpha\int_0^{2\pi}\sqrt{\cos\theta}\cdot\sin^2\theta\cdot\exp(i\psi)$$
$$\cdot J_{|m|/2}\left[\frac{\sin^2(\theta)}{w^2\cdot NA^2}\right]\cdot\exp\left[-\frac{\sin^2(\theta)}{w^2\cdot NA^2}\right]\cdot\exp(im\phi)$$
$$\cdot\exp\left[i\cdot\pi\cdot\cos\left(C\cdot\frac{\tan\theta}{\tan\alpha}\cdot\pi\right)\right]$$
$$\cdot\exp\left\{ik\left[z\cos\theta+\rho\sin\theta\cos(\phi-\varphi)\right]\right\}d\phi d\theta \quad (11)$$

The optical intensity in focal region is proportional to the modulus square of **Eq.3**. Basing on the above equations, focusing properties of radially polarized QBG beam with phase shifting can be investigated theoretically.

3. RESULTS AND DISCUSSIONS

Without of loss of validity and generality, it was supposed that NA=0.95, μ=5 and w=1. Firstly, the intensity distributions in focal region of the radially polarized QBG beam with phase shifting are calculated under condition of m=0 and different C, and are illustrated in **Figure 1**. It should be noted that the distance unit in all figures in this paper is k^{-1}, where k is the wave number of incident beam. In addition, the coordinates are the radial distance and axial distance, and symmetric characteristics should be paid attention to when see figures. It can be seen that there occurs one dark hollow focus in focal region for C=0.0. Dark hollow focus refers to those focuses whose optical intensity is weaker than that around it and is stable optical trap for those particles

whose refractive index is smaller than that of surrounding media, and this condition is very common, especially in life science optical trapping systems, so construction of dark focal spot is very important and attracts many researchers [18,19]. Therefore, radially polarized QBG beam can be used to construct dark hollow focus. On increasing *C*, this dark hollow focus shifts along optical axis away from the optical aperture of the focusing system, as shown in **Figure 1b**. And the point of absolute maximum intensity also shifts along optical axis. The number of the absolute maximum intensity changes from two to one, namely, the on-axis intensity peak near to the optical aperture weakens on increasing *C*, as illustrated in **Figure 1c**. Increase *C* continuously, the shape of dark hollow focus goes on shifting along optical axis. How ever, the position of absolute maximum intensity becomes incontinuous, namely, jumps to one position near the optical aperture, and then also shifts far away from optical aperture.

In order to understand the focal shift deeply, the dependence of focal shift on *C* is calculated and shown in

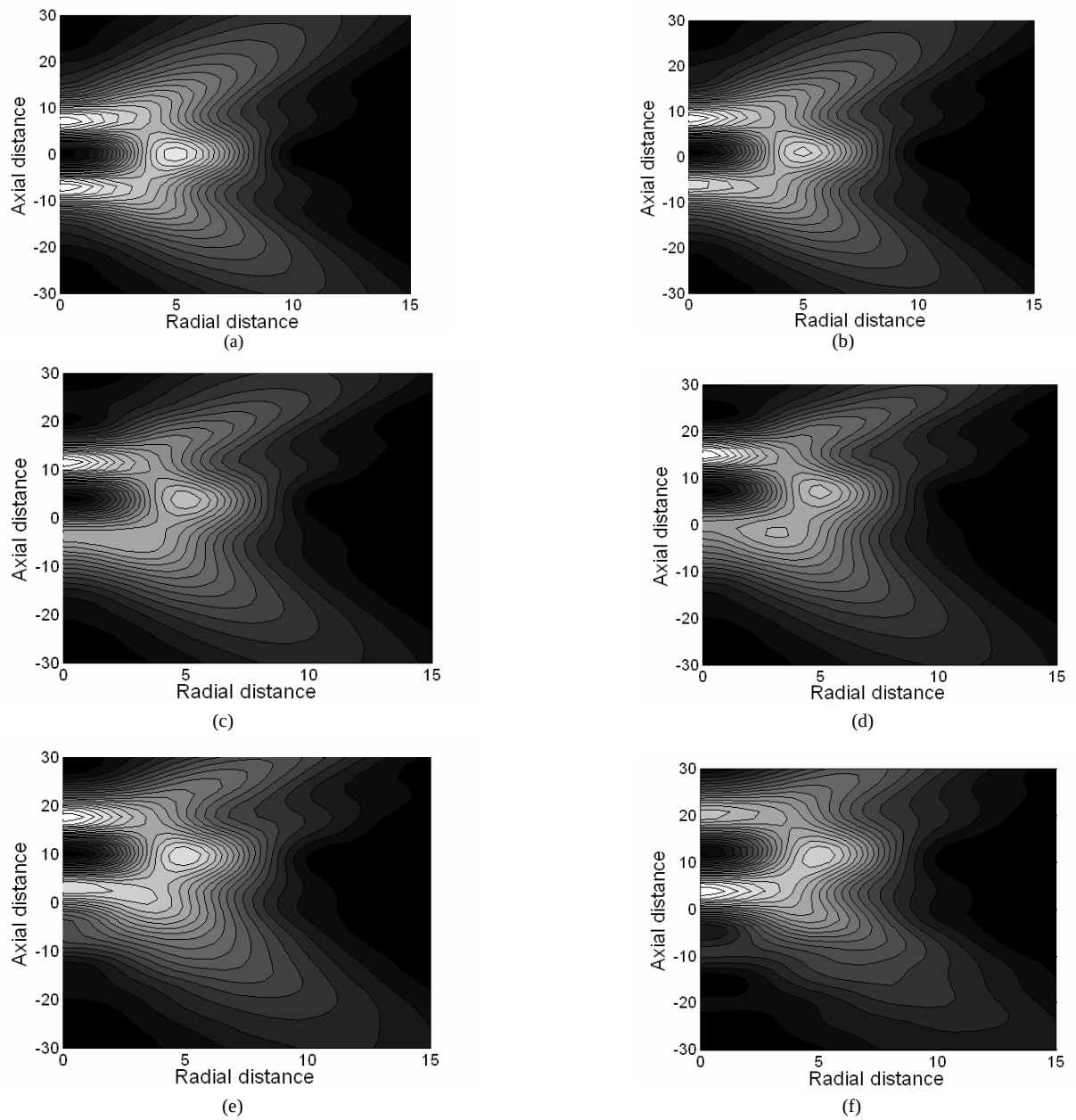

Figure 1. Intensity distributions in focal region for m=0 and (a) C=0.0, (b) C=0.3, (c) C=0.6, (d) C=0.9, (e) C=1.2, and (f) C=1.5, respectively

Figure 2. It can be seen from this figure that when C=0.0 there are two absolute maximum intensity peaks on axis, and on increasing C, one absolute maximum intensity peaks weakens so that there is only one absolute maximum intensity peak, and in the focal evolution process, the distance of focal shift increases on increasing C.

When C changes from 1.2 to 1.3, the position of absolute maximum intensity peak jumps from on position to another position, then also shifts increases on increasing C. Focal shift is incontinuous.

Figure 3 illustrates the optical intensity distributions in focal region under condition of m=2 and different C.

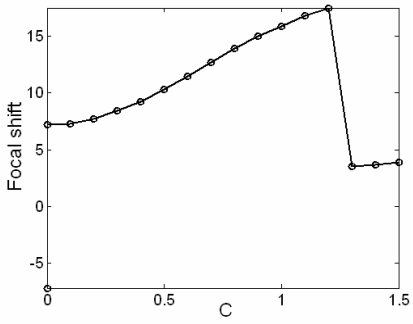

Figure 2. Dependence of focal shift on C for m=0.

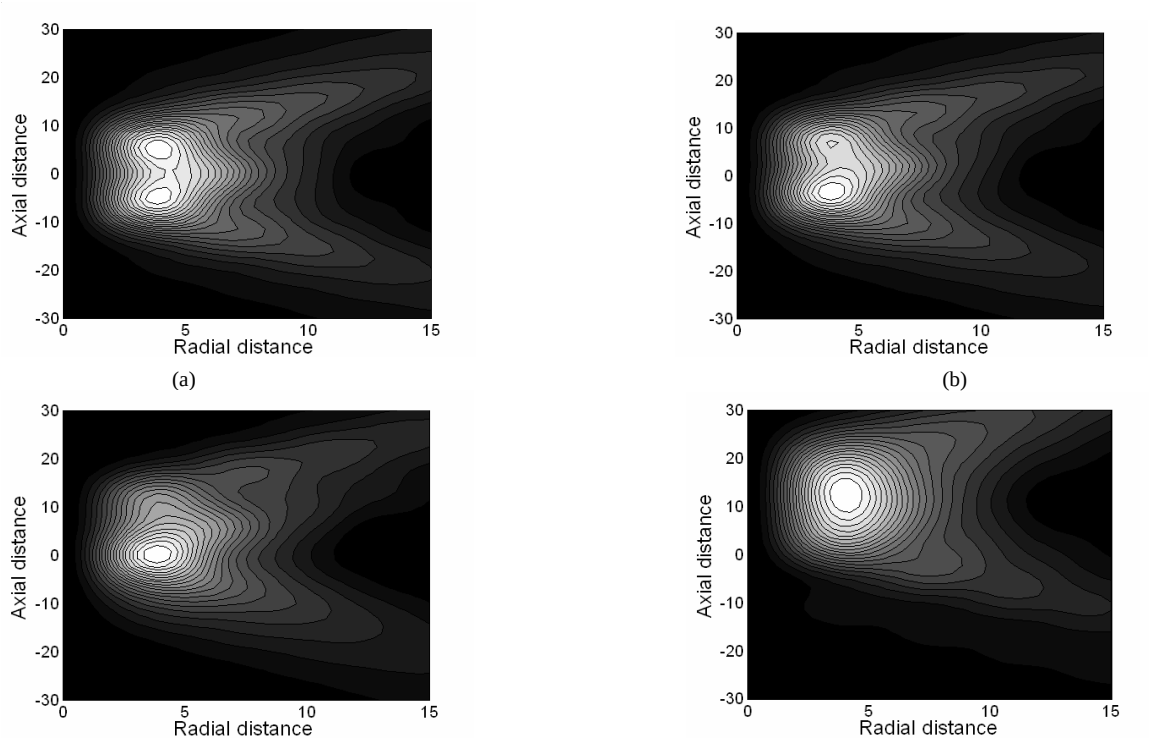

Figure 3. Intensity distributions in focal region for m=2 and (a) C=0.0; (b) C=0.3; (c) C=0.6, and; (d) C=1.5, respectively.

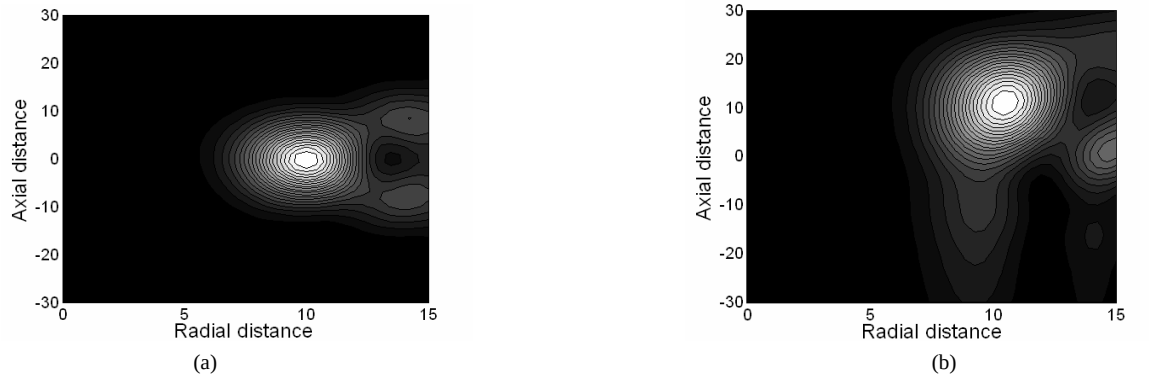

Figure 4. Intensity distributions in focal region for m=7 and (a) C=0.0; (b) C=1.5, respectively.

For C =0.0, there is two overlapping intensity rings in focal region, as shown in **Figure 3a**. On increasing C. one of these two intensity ring weakens, so that one focal ring comes into being and shifts in axial direction. From all above focal pattern evolution, we can see that Topological charge induces the focal shift in transverse direction, while phase parameter leads to the focal shift along optical axis of the focusing system. In order to show this point, optical intensity distributions in focal region under condition of m=7 are also calculated and illustrated in **Figure 4**. Ring intensity distribution can be used to construct a ring optical trap that is stable for those particles in focal region whose refraction index is bigger than that of their surrounding medium.

4. CONCLUSIONS

Focal shift of radially polarized QBG beam by phase shifting is investigated theoretically by vector diffraction theory in this paper. The phase shifting distribution is the function of the radial coordinate. Simulations results show that intensity distribution in focal region can be altered considerably by the topological charge of QBG beam and the phase parameter that indicates the vary degree of the phase shifting along radial coordinate. Dark hollow focus can be obtained in focal region of radially polarized QBG beam, which is very desirable in optical tweezers technique. Particularly, topological charge induces the focal pattern evolution in transverse direction, while phase parameter leads to the focal shift along optical axis more significantly.

5. ACKNOWLEDGMENT

This work was supported by National Basic Research Program of China (2005CB724304), National Natural Science Foundation of China (60708002, 60777045, 60871088, 60778022), China Postdoctoral Science Foundation (20080430086), and Shanghai Postdoctoral Science Foundation of China (08R214141).

REFERENCES

[1] C. F. R. Caron and R. M. Potvliege, (1999) Bessel-modulated Gausian beams with quadratic radial dependence. Opt. Commun, **164**, 83-93.

[2] Z. Hricha and A. Belafhal, (2005) Focal shift in the axisymmetric Bessel-modulated Gaussian beam. Opt. Commun, **255**, 235-240.

[3] X. Wang and B. Lü, (2002) The beam propagation factor and far-field distribution of Bessel-modulated Gaussian beams. Opt. Quant. Electron, **34**, 1071-1077.

[4] A. Belafhal and L. Dalil-Essakali, (2000) Collins formula and propagation of Bessel-modulated Gaussian light beams through an ABCD optical system. Opt. Commun, **177**, 181-188.

[5] X. Wang and B. Lü, (2003) The beamwidth of Bessel-modulated Gaussian beams. J. Mod. Opt, **50**, 2107-2115.

[6] B. Lü and X. Wang, (2002) Kurtosis parameter of Bessel-modulated Gaussian beams propagating through ABCD optical systems. Opt. Commun, **204**, 91-97.

[7] Z. Mei, D. Zhao, X. Wei, F. Jing, and Q. Zhu, (2005) Propagation of Bessel-modulated Gaussian beams through a paraxial ABCD optical system with an annular aperture. Optik, **116**, 521-526.

[8] Y. Li and E. Wolf, (1981) Focal shifts in diffracted converging spherical waves. Opt. Commun, **39**, 211-215.

[9] M. M. Corral, M. T. Caballero, L. M. Escriva, and P. Andres, (2001) Focal-shift formula in apodized non-telecentric focusing systems. Opt. Lett, **26**, 1501- 1503.

[10] C. J. R. Sheppard and P. Tötök, (2003) Focal shift and axial coordinate for high-aperture systems of finite Fresnel number. J. Opt. Soc. Am. A, **20**, 2156-2162.

[11] X. Gao, F. Zhou, W. Xu, and F. Gan, (2005) Gradient force pattern, focal shift, and focal switch in an apodized optical system. Optik, **116**, 99-106.

[12] X. Gao and J. Li, (2007) Focal shift of apodized truncated hperbolic-Cosine-Gaussian beam. Opt. Commun, **273**, 21-27.

[13] K. S. Youngworth and T. G. Brown, (2000) Focusing of high numerical aperture cylindrical-vector beams. Optics Express, **7**, 77-87.

[14] Q. Zhan, (2009) Cylindrical vector beams: from mathematical concepts to applications. Advances in Optics and Photonics, **1**, 1–57.

[15] X. Gao, S. Hu, H. Gu, and J. Wang, (2009) Focal shift of three-portion concentric piecewise cylindrical vector beam. Optik, **120**, 519-523.

[16] F. Lu, W. Zheng, and Z. Huang, (2009) Coherent anti-stokes Raman scattering micriscopy using tighly focused radially polarized light. Opt. Lett, **34**, 1870-1871.

[17] S. Sato and Y. Kozawa, (2009) Hollow vortex beams. J. Opt. Soc. Am. A, **26**, 142-146.

[18] J. Arlt and M. J. Padgett, (2000) Generation of a beam with a dark focus surrounded by regions of higher intensity: The optical bottle beam. Opt. Lett, **25**, 191-193.

[19] D. Ganic, X. Gan, M. Gu, M. Hain, S. Somalingam, S. Stankovic, and T. Tschudi, (2002) Generation of doughnut laser beams by use of a liquid-crystal cell with a conversion efficiency near 100%. Opt. Lett, **27**, 1351-1353.

Call for Papers

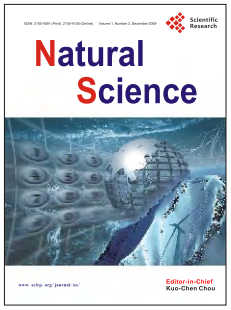

Natural Science

A Journal Published by Scientific Research Publishing, USA
www.scirp.org/journal/ns

Natural Science is an international journal dedicated to the latest advancement of natural sciences. The goal of this journal is to provide a platform for scientists and academicians all over the world to promote, share, and discuss various new issues and developments in different areas of natural sciences. All manuscripts must be prepared in English, and are subject to a rigorous and fair peer-review process. Accepted papers will immediately appear online followed by printed hard copy. The journal publishes original papers including but not limited to the following fields:

- **Astronomy & Space Sciences**
  - Astronomy
  - Astrophysics
  - Atmospheric Science
  - Space Physics
- **Earth Science**
  - Geography
  - Geology
  - Geophysics/Geochemistry
  - Oceanography
- **Chemistry**
  - Analytical Chemistry
  - Biochemistry
  - Computational Chemistry
  - Inorganic Chemistry
  - Organic Chemistry
  - Physical Chemistry
- **Life Science**
  - Cell Biology
  - Computational Biology
  - Genetics
  - Immunology
  - Medicine/Diseases
  - Microbiology
  - Molecular Biology
  - Neuroscience
  - Pharmacology/Toxicology
  - Physiology
  - Psychology
  - Virology
- **Physics**
  - Applied Physics
  - Atomic, Molecular, and Optical Physics
  - Biophysics
  - High Energy/Particle Physics
  - Material Science
  - Plasma Physics
- **Others**
  - Education
  - History of Science
  - Science and Innovations

We are also interested in: 1) Short Reports—2-5 page papers where an author can either present an idea with theoretical background but has not yet completed the research needed for a complete paper or preliminary data; 2) Book Reviews—Comments and critiques.

Notes for Intending Authors

Submitted papers should not be previously published nor be currently under consideration for publication elsewhere. Paper submission will be handled electronically through the website. For more details, please access the website.

Website and E-Mail

http://www.scirp.org/journal/ns ns@scirp.org

Natural Science, 2009, 1, 157-233
Published Online December 2009 in SciRes (http://www.scirp.org/journal/ns).

TABLE OF CONTENTS

Volume 1, Number 3, December 2009

ISSN: 2150-4091

9772150409001 03